Measurements of the proton and deuteron spin structure functions g_1 and g_2

K. Abe,[15] T. Akagi,[11,15] P. L. Anthony,[11] R. Antonov,[10] R. G. Arnold,[1] T. Averett,[16,*] H. R. Band,[18] J. M. Bauer,[6,†] H. Borel,[4] P. E. Bosted,[1] V. Breton,[3] J. Button-Shafer,[6] J. P. Chen,[16,7] T. E. Chupp,[7] J. Clendenin,[11] C. Comptour,[3] K. P. Coulter,[7] G. Court,[11,‡] D. Crabb,[16] M. Daoudi,[11] D. Day,[16] F. S. Dietrich,[5] J. Dunne,[1,14] H. Dutz,[11,§] R. Erbacher,[11,12] J. Fellbaum,[1] A. Feltham,[2] H. Fonvieille,[3] E. Frlez,[16] D. Garvey,[8] R. Gearhart,[11] J. Gomez,[14] P. Grenier,[4] K. A. Griffioen,[10,17] S. Hoibraten,[16,‖] E. W. Hughes,[11,*] C. Hyde-Wright,[9] J. R. Johnson,[18] D. Kawall,[12] A. Klein,[9] S. E. Kuhn,[9] M. Kuriki,[15] R. Lindgren,[16] T. J. Liu,[16] R. M. Lombard-Nelsen,[4] J. Marroncle,[4] T. Maruyama,[11] X. K. Maruyama,[8] J. McCarthy,[16] W. Meyer,[11,**] Z.-E. Meziani,[12,13] R. Minehart,[16] J. Mitchell,[14] J. Morgenstern,[4] G. G. Petratos,[11,††] R. Pitthan,[11] D. Pocanic,[16] C. Prescott,[11] R. Prepost,[18] P. Raines,[10] B. Raue,[9,‡‡] D. Reyna,[1] A. Rijllart,[11,§§] Y. Roblin,[3] L. S. Rochester,[11] S. E. Rock,[1] O. A. Rondon,[16] I. Sick,[2] L. C. Smith,[16] T. B. Smith,[7] M. Spengos,[1,10] F. Staley,[4] P. Steiner,[2] S. St. Lorant,[11] L. M. Stuart,[11] F. Suekane,[15] Z. M. Szalata,[1] H. Tang,[11] Y. Terrien,[4] T. Usher,[11] D. Walz,[11] F. Wesselmann,[9] J. L. White,[1,11] K. Witte,[11] C. C. Young,[11] B. Youngman,[11] H. Yuta,[15] G. Zapalac,[18] B. Zihlmann,[2] and D. Zimmermann[16]

(E143 Collaboration)

[1]*The American University, Washington, D.C. 20016*

[2]*Institut für Physik der Universität Basel, CH–4056 Basel, Switzerland*

[3]*LPC IN2P3/CNRS, University Blaise Pascal, F–63170 Aubiere Cedex, France*

[4]*DAPNIA-Service de Physique Nucleaire Centre d'Etudes de Saclay, F–91191 Gif-sur-Yvette, France*

[5]*Lawrence Livermore National Laboratory, Livermore, California 94550*

[6]*University of Massachusetts, Amherst, Massachusetts 01003*

[7]*University of Michigan, Ann Arbor, Michigan 48109*

[8]*Naval Postgraduate School, Monterey, California 93943*

[9]*Old Dominion University, Norfolk, Virginia 23529*

[10]*University of Pennsylvania, Philadelphia, Pennsylvania 19104*

[11]*Stanford Linear Accelerator Center, Stanford, California 94309*

[12]*Stanford University, Stanford, California 94305*

[13]*Temple University, Philadelphia, Pennsylvania 19122*

[14]*Thomas Jefferson National Accelerator Facility, Newport News, Virginia 23606*

[15]*Tohoku University, Sendai 980, Japan*

[16]*University of Virginia, Charlottesville, Virginia 22901*

[17]*The College of William and Mary, Williamsburg, Virginia 23187*

[18]*University of Wisconsin, Madison, Wisconsin 53706*

(Received 13 February 1998; published 27 October 1998)

Measurements are reported of the proton and deuteron spin structure functions g_1^p and g_1^d at beam energies of 29.1, 16.2, and 9.7 GeV, and g_2^p and g_2^d at a beam energy of 29.1 GeV. The integrals $\Gamma_p = \int_0^1 g_1^p(x,Q^2)dx$ and $\Gamma_d = \int_0^1 g_1^d(x,Q^2)dx$ were evaluated at fixed $Q^2 = 3\,(\mathrm{GeV}/c)^2$ using the full data set to yield $\Gamma_p = 0.132 \pm 0.003(\mathrm{stat}) \pm 0.009(\mathrm{syst})$ and $\Gamma_d = 0.047 \pm 0.003 \pm 0.006$. The Q^2 dependence of the ratio g_1/F_1 was studied and found to be small for $Q^2 > 1\,(\mathrm{GeV}/c)^2$. Within experimental precision the g_2 data are well described by the twist-2 contribution, g_2^{WW}. Twist-3 matrix elements were extracted and compared to theoretical predictions. The asymmetry A_2 was measured and found to be significantly smaller than the positivity limit $\sqrt{R}$ for both proton and deuteron targets. A_2^p is found to be positive and inconsistent with zero. Measurements of g_1 in the resonance region show strong variations with x and Q^2, consistent with resonant amplitudes extracted from unpolarized data. These data allow us to study the Q^2 dependence of the integrals Γ_p and Γ_n below the scaling region. [S0556-2821(98)06919-7]

PACS number(s): 13.60.Hb, 11.55.Hx, 13.88.+e, 25.30.Fj

---

*Present address: California Institute of Technology, Pasadena, CA 91125.

†Present address: University of Mississippi, University, MS 38677.

‡Permanent address: Oliver Lodge Lab, University of Liverpool, Liverpool, U.K.

§Permanent address: University of Bonn, D-53113 Bonn, Germany.

‖Permanent address: FFIYM, P.O. Box 25, N-2007 Kjeller, Norway.

**Permanent address: University of Bonn, D-53113 Bonn, Germany.

††Permanent address: Kent State University, Kent, Ohio 44242.

‡‡Permanent address: Florida International University, Miami, FL 33199.

§§Permanent address: CERN, 1211 Geneva 23, Switzerland.

I. INTRODUCTION

Inelastic lepton scattering from nucleons has been used over the past thirty years to obtain an ever increasing knowledge of the distribution of the partons that make up the nucleon, namely gluons and up, down, strange, and perhaps charmed quarks. It is one of the great successes of QCD that the same parton densities can be used to describe the unpolarized inelastic structure functions $F_1(x,Q^2)$ and $F_2(x,Q^2)$ as well as many other physical processes, such as the production of jets in pp collisions. The parton densities depend on the fractional momentum of the parton $x=Q^2/2M\nu$, where $-Q^2$ is the four-momentum transfer squared, M is the nucleon mass, and ν is the lepton energy transfer. The measured Q^2 dependence at fixed x of $F_1(x,Q^2)$ and $F_2(x,Q^2)$ has been shown to be in very good agreement with the QCD-based evolution equations [1].

The F_1 and F_2 structure functions are sensitive to the helicity-averaged parton densities. Recent improvements in polarized lepton beams and targets have made it possible to make increasingly accurate measurements of two additional structure functions, $g_1(x,Q^2)$ and $g_2(x,Q^2)$, which depend on the difference in parton densities with helicity either aligned or anti-aligned with the spin of the nucleon. Measurements of g_1^p have been made using electron beams at SLAC [2–5] and muon beams at CERN [6,7], while g_1^n has been measured both using polarized deuteron targets at SLAC [5,8] and CERN [9], and a ^{3}He target at SLAC [10,11] and DESY [12]. Measurements have also been made of g_2 for both the proton and deuteron [10,13–15], although with limited statistical precision compared to the g_1 measurements. This paper reports final results for g_1^p, g_1^d, g_2^p, and g_2^d from experiment E143 at SLAC, and includes more details of the analysis procedure, as well as some auxiliary results not covered in the original short publications [4,5,8,13,16].

The earliest experiments [2,3,6] sparked considerable interest in the spin structure functions when it was reported that, contrary to the quark model expectation, the quarks contribute very little to the proton's spin (the so-called ''spin crisis''). Subsequent precision measurements are consistent with the original experimental results (with improved QCD corrections applied), but the theoretical interpretation has become more complex. It is now believed that in addition to the quarks, the orbital angular momentum and gluons may contribute significantly to the proton's spin. There is still the unanswered question as to how much the gluons alone really contribute. The g_1 and g_2 structure functions are interesting not only in opening a new degree of freedom with which to explore the detailed structure of the nucleon, but also for making a precise test of QCD via the Bjorken sum rule which is a strict QCD prediction [17].

In this paper we describe the theory and phenomenology of spin structure physics, and detail the SLAC experiment E143, which measured both $A_\parallel$ and $A_\perp$ for proton and deuteron targets over a wide range of kinematics. The theory and experimental apparatus are described in Secs. II and III. The analysis procedure is detailed in Sec. IV. Results, their interpretation, and a discussion of systematic errors are shown in Sec. V, and finally we present a summary and conclusions in Sec. VI.

II. INTERPRETATION AND THEORY

A. Formalism

The structure functions $g_1(x,Q^2)$ and $g_2(x,Q^2)$ are typically extracted from asymmetry measurements. Longitudinally polarized leptons are scattered from a target that is polarized either longitudinally or transversely. The longitudinal ($A_\parallel$) and transverse ($A_\perp$) asymmetries are formed from combining data taken with opposite beam helicity:

$$A_\parallel=\frac{\sigma^{\downarrow\uparrow}-\sigma^{\uparrow\uparrow}}{\sigma^{\downarrow\uparrow}+\sigma^{\uparrow\uparrow}}, \quad A_\perp=\frac{\sigma^{\downarrow\rightarrow}-\sigma^{\uparrow\rightarrow}}{\sigma^{\downarrow\rightarrow}+\sigma^{\uparrow\rightarrow}}. \tag{1}$$

The polarized structure functions can be determined from these asymmetries:

$$g_1(x,Q^2)=\frac{F_1(x,Q^2)}{d'}\,[A_\parallel+\tan(\theta/2)A_\perp],$$

$$g_2(x,Q^2)=\frac{yF_1(x,Q^2)}{2d'}\left[\frac{E+E'\,\cos(\theta)}{E'\,\sin(\theta)}A_\perp-A_\parallel\right], \tag{2}$$

where E is the incident electron energy, E' is the scattered electron energy, θ is the scattering angle, $y=(E-E')/E$, $d'=[(1-\epsilon)(2-y)]/[y(1+\epsilon R(x,Q^2))]$, $\epsilon^{-1}=1+2[1+\gamma^{-2}]\tan^2(\theta/2)$, $\gamma=2Mx/\sqrt{Q^2}$, M is the nucleon mass and $R(x,Q^2)=\sigma_L/\sigma_T$ is the ratio of longitudinal and transverse virtual photon-absorption cross sections. $R(x,Q^2)$ is related to the spin-averaged (or unpolarized) structure functions $F_1(x,Q^2)$ and $F_2(x,Q^2)$ by $R(x,Q^2)+1=(1+\gamma^2)F_2(x,Q^2)/[2xF_1(x,Q^2)]$.

The virtual photon-absorption asymmetries A_1 and A_2 are related to the measured asymmetries by

$$A_\parallel=D(A_1+\eta A_2),$$

$$A_\perp=d(A_2-\zeta A_1), \tag{3}$$

where the photon depolarization factor $D=(1-E'\epsilon/E)/(1+\epsilon R)$, $\eta=\epsilon\sqrt{Q^2}/(E-E'\epsilon)$, $d=D\sqrt{2\epsilon/(1+\epsilon)}$, and $\zeta=\eta(1+\epsilon)/2\epsilon$. A_1 and A_2 can be expressed as

$$A_1=\frac{\sigma_{1/2}^T-\sigma_{3/2}^T}{\sigma_{1/2}^T+\sigma_{3/2}^T}=\frac{\sigma_{TT}}{\sigma_T}=\frac{A_\parallel}{D(1+\eta\zeta)}-\frac{\eta A_\perp}{d(1+\eta\zeta)}$$
$$=\frac{g_1(x,Q^2)-\gamma^2 g_2(x,Q^2)}{F_1(x,Q^2)}$$

$$A_2=\frac{2\sigma_{LT}}{\sigma_{1/2}^T+\sigma_{3/2}^T}=\frac{\sigma_{LT}}{\sigma_T}=\frac{\zeta A_\parallel}{D(1+\eta\zeta)}+\frac{A_\perp}{d(1+\eta\zeta)}$$
$$=\frac{\gamma[g_1(x,Q^2)+g_2(x,Q^2)]}{F_1(x,Q^2)}, \tag{4}$$

where $\sigma_{1/2}^T$ and $\sigma_{3/2}^T$ are the virtual photoabsorption transverse cross sections for total helicity between photon and nucleon of 1/2 and 3/2 respectively, σ_{LT} is the interference term between the transverse and longitudinal photon-nucleon amplitudes, $\sigma_T=(\sigma_{1/2}^T+\sigma_{3/2}^T)/2$, and $\sigma_{TT}=(\sigma_{1/2}^T-\sigma_{3/2}^T)/2$. We see from Eq. (4) that for low x or high Q^2 (where $\gamma \ll 1$), $A_1 \approx g_1/F_1$. Positivity constrains $|A_1| \leqslant 1$ and $|A_2| \leqslant \sqrt{R(x,Q^2)}$. For the case where only the longitudinal asymmetry is measured, and a model is used for g_2, A_1 and g_1 can be expressed as

$$A_1=\frac{A_\parallel}{d'}\left[1+\frac{xMy}{E+E'\cos(\theta)}\right]-\frac{g_2}{F_1}\left[\frac{4xME'\cos^2(\theta/2)}{\nu(E+E'\cos(\theta))}\right],$$

$$g_1=\frac{A_\parallel F_1}{d'}\left[\frac{E+E'}{E+E'\cos(\theta)}\right]+g_2\left[\frac{2Mx}{E+E'\cos(\theta)}\right]. \tag{5}$$

In the resonance region, g_1 and g_2 are well defined but are more properly interpreted in terms of the helicity structure of the resonance transition amplitudes. The γ^*NN^* vertex for electro-excitation of the resonance N^* is generally given in terms of three amplitudes, $A_{1/2}(Q^2)$, $A_{3/2}(Q^2)$ and $S_{1/2}(Q^2)$ [18,19]. Here, A denotes transverse photon polarization and S indicates longitudinal photons. The index 1/2 or 3/2 refers again to the total γ^*N helicity. The virtual photon-nucleon cross sections for an isolated resonance can then be written in terms of helicity amplitudes as

$$\sigma_{1/2}^T=\frac{4\pi^2\alpha}{KM}\left(F_1+g_1-\frac{2Mx}{\nu}g_2\right)=2\pi\frac{M}{W}b|A_{1/2}|^2,$$

$$\sigma_{3/2}^T=\frac{4\pi^2\alpha}{KM}\left(F_1-g_1+\frac{2Mx}{\nu}g_2\right)=2\pi\frac{M}{W}b|A_{3/2}|^2,$$

$$\sigma_{1/2}^L=\sigma_L=\frac{4\pi^2\alpha}{K}\left[\frac{F_2}{\nu}\left(1+\frac{\nu^2}{Q^2}\right)-\frac{F_1}{M}\right]$$

$$=2\pi\frac{M}{W}b\frac{Q^2}{q^{*2}}|S_{1/2}|^2,$$

$$\sigma_{1/2}^{LT}=\sigma_{LT}=\frac{4\pi^2\alpha}{K}\frac{\sqrt{Q^2}}{M\nu}(g_1+g_2)$$

$$=\pi\frac{M}{W}\sqrt{2}b\frac{Q}{q^*}S_{1/2}^*A_{1/2}, \tag{6}$$

in which K is the incoming photon flux which is chosen using the Hand convention such that the invariant mass squared of the final state is $W^2=M^2+2MK$, b is the resonance line shape (unit area), and $q^{*2}=Q^2+(W^2-M^2-Q^2)/4W^2$ is the squared magnitude of the 3-momentum transfer measured in the resonance rest frame. The electron scattering cross sections are then written

$$\frac{d\sigma}{dE'd\Omega}=\Gamma_V[\sigma_T+\epsilon\sigma_L],$$

$$\frac{d\sigma^{\downarrow\uparrow}}{dE'd\Omega}-\frac{d\sigma^{\uparrow\uparrow}}{dE'd\Omega}=2\Gamma_V D(1+\epsilon R)[\sigma_{TT}+\eta\sigma_{LT}],$$

$$\frac{d\sigma^{\downarrow\rightarrow}}{dE'd\Omega}-\frac{d\sigma^{\uparrow\rightarrow}}{dE'd\Omega}=2\Gamma_V d(1+\epsilon R)[\sigma_{LT}-\zeta\sigma_{TT}], \tag{7}$$

where

$$\Gamma_V=\frac{\alpha}{4\pi^2}\frac{K}{Q^2}\frac{E'}{E}\frac{2}{1-\epsilon}. \tag{8}$$

B. The deep-inelastic spin structure function $g_1(x,Q^2)$

As will be shown below, the first moment of the spin structure function $g_1(x,Q^2)$ is related to the net quark helicity $\Delta\Sigma$ which contributes to the proton spin. Angular momentum conservation requires that

$$\frac{1}{2}=\frac{\Delta\Sigma}{2}+\Delta G+L_z, \tag{9}$$

where ΔG is the net gluon helicity, and L_z is the orbital angular momentum.

1. The quark-parton model

In the naive quark-parton model (QPM) the nucleon is composed of quarks which have no orbital angular momentum, and there are no polarized gluons present. In this simple picture, the unpolarized structure function $F_1(x,Q^2)$ and the polarized structure function $g_1(x,Q^2)$ can be simply expressed as the charge-weighted sum and difference between momentum distributions for quark helicities aligned parallel ($q^\uparrow$) and antiparallel ($q^\downarrow$) to the longitudinally polarized nucleon:

$$F_1(x)=\tfrac{1}{2}\sum_i e_i^2[q_i^\uparrow(x)+q_i^\downarrow(x)],$$

$$g_1(x)=\tfrac{1}{2}\sum_i e_i^2[q_i^\uparrow(x)-q_i^\downarrow(x)]\equiv\sum_i e_i^2\Delta q_i(x). \tag{10}$$

The charge of quark flavor u, d, and s is denoted by e_i, and $q_i^{\uparrow(\downarrow)}(x)$ are the quark plus antiquark momentum distributions. The quantity $\int_0^1\Delta q_i(x)dx=\Delta q_i$ refers to the helicity of quark flavor i in the proton, and $\Delta\Sigma=\Delta u+\Delta d+\Delta s$ is the net helicity of quarks. Since $\Delta G=0$ and $L_z=0$, it follows from Eq. (9), that $\Delta\Sigma$ is expected to be unity in this model. In a relativistic quark-parton model [20–22] (with no polarized gluons), the orbital angular momentum contribution is no longer zero and the quark helicity contributions to the proton helicity are suppressed by a factor of about 0.75.

2. Perturbative QCD and the role of the gluons

The quark-parton model is useful for understanding some properties of the nucleon such as charge and isospin. However, it fails to adequately describe all properties, and it falls short in explaining the dynamics of particle interactions. For this we need a more comprehensive theory such as quantum chromodynamics (QCD) which can account for gluons and their interactions with the quarks.

The operator product expansion (OPE) [23–25] is a useful technique within QCD because it separates the physics into a perturbative part that is easily treatable and a nonperturbative part that is parameterized in terms of unknown matrix elements of Lorentz-covariant operators. At leading twist the first moment of $g_1(x,Q^2)$ can be expressed in terms of singlet (a_0) and nonsinglet (a_3 and a_8) proton matrix elements of the axial current:

$$\Gamma_1^p(Q^2)=\int_0^1 g_1^p(x,Q^2)dx=\left(\frac{1}{12}a_3+\frac{1}{36}a_8\right)C_{ns}+\frac{1}{9}a_0C_s,$$

$$\Gamma_1^d(Q^2)=\int_0^1 g_1^d(x,Q^2)dx=\left(1-\frac{3}{2}\omega_D\right)\times\left[\frac{1}{36}a_8C_{ns}+\frac{1}{9}a_0C_s\right], \tag{11}$$

where ω_D is the D-state probability in the deuteron, and the factors C_{ns} and C_s are the Q^2-dependent non-singlet and singlet QCD corrections, which are discussed in more detail below.

Assuming that there are no polarized gluons contributing to the proton spin, the singlet and nonsinglet proton matrix elements given in Eq. (11) can be related to the quark helicities:

$$a_0=\Delta u+\Delta d+\Delta s=\Delta\Sigma,$$

$$a_3=\Delta u-\Delta d=F+D,$$

$$a_8=\Delta u+\Delta d-2\Delta s=3F-D. \tag{12}$$

Here, F and D are weak hyperon decay constants which can be extracted from data assuming $SU(3)$ symmetry [26,27]

$$F+D=g_A=1.2601\pm0.0025,$$

$$3F-D=0.588\pm0.033. \tag{13}$$

The error quoted above on $3F-D$ is the experimental error assuming SU(3) symmetry. It may be an underestimate because possible $SU(3)$ symmetry breaking effects could be significant. There have been a number of attempts to estimate these effects [20,28–32]. According to Ratcliffe [29], symmetry breaking effects in the past have always been found to be at most 10%. Assuming a generous 20% systematic error from symmetry breaking combined with the above error in quadrature yields an error of 0.12 on $3F-D$. This error is somewhat smaller than the range of possible values (0.40–0.84) presented under various assumptions [28,29,31,32], some of which have come under criticism [29].

After combining Eq. (11) and Eq. (12) [27] it is straightforward to extract the singlet matrix element from the measured first moments of the proton:

$$a_0=\frac{9}{C_s}\left[\Gamma_1^p(Q^2)-\frac{1}{18}(3F+D)C_{ns}\right], \tag{14}$$

and the deuteron:

$$a_0=\frac{9}{C_s}\left[\frac{\Gamma_1^d(Q^2)}{1-\frac{3}{2}\omega_D}-\frac{1}{36}(3F-D)C_{ns}\right]. \tag{15}$$

The nonsinglet QCD correction C_{ns} [33] calculated in the modified minimal subtraction ($\overline{\text{MS}}$) scheme to order three for three quark flavors is given by

$$C_{ns}=1-\frac{\alpha_s(Q^2)}{\pi}-3.58\left(\frac{\alpha_s(Q^2)}{\pi}\right)^2-20.22\left(\frac{\alpha_s(Q^2)}{\pi}\right)^3, \tag{16}$$

where $\alpha_s(Q^2)$ is the strong coupling constant. Fourth order QCD corrections have been estimated [34] to be small at the kinematics of this experiment. The singlet QCD correction exists in two forms [33], one which yields a Q^2-dependent $a_0(Q^2)$ in Eqs. (14)–(15) and one which yields a_0^{inv} which is the asymptotic high Q^2 limit of $a_0(Q^2)$. These singlet QCD corrections have been calculated in the $\overline{\text{MS}}$ scheme [33]:

$$C_s(Q^2)=1-\frac{\alpha_s(Q^2)}{\pi}-1.10\left(\frac{\alpha_s(Q^2)}{\pi}\right)^2,$$

$$C_s^{inv}=1-0.3333\left(\frac{\alpha_s(Q^2)}{\pi}\right)-0.5495\left(\frac{\alpha_s(Q^2)}{\pi}\right)^2. \tag{17}$$

The contribution of ΔG to a_0 (and thus to the first moment of g_1) is a factorization scheme-dependent quantity. In a gauge-invariant scheme such as the $\overline{\text{MS}}$ scheme gluons do not contribute to the first moment of g_1 which means that $a_0=\Delta\Sigma$. For chiral-invariant schemes such as the Adler-Bardeen scheme [35] the gluons do contribute to Γ_1. The physical quantity $g_1(x)$ is independent of the factorization scheme, however. In the Adler-Bardeen scheme [35], the quantity $a_0\neq\Delta\Sigma$, and is instead written as

$$a_0=\Delta\Sigma-\frac{3}{2\pi}\alpha_s(Q^2)\Delta G(Q^2). \tag{18}$$

This contribution of ΔG is called the gluon axial anomaly [36] or the Adler-Bell-Jackiw anomaly (as applied to QCD from QED). The product $\alpha_s(Q^2)\Delta G(Q^2)$ is independent of Q^2 in leading order which implies that $\Delta G(Q^2)$ grows in Q^2 like $1/\alpha_s(Q^2)$, and L_z compensates to satisfy Eq. (9). Physically, this means that as each quark radiates a gluon with some preferential helicity the orbital angular momentum of

TABLE I. Quark helicity predictions from the nonrelativistic quark-parton model (NR QPM) where $\Delta G=0$ and from the relativistic quark-parton model (R QPM) [21,22] with $\Delta G=0$ and $\Delta G(Q^2=1(\mathrm{GeV}/c)^2)=1.6\pm0.9$ [37].

	NR QPM	R QPM	R QPM+gluons
$\alpha_s\Delta G/2\pi$	0	0	0.13 ± 0.08
$\Delta u-\alpha_s\Delta G/2\pi$	1.33	1.0	0.87 ± 0.08
$\Delta d-\alpha_s\Delta G/2\pi$	-0.33	-0.25	-0.38 ± 0.08
$\Delta s-\alpha_s\Delta G/2\pi$	0	0	-0.13 ± 0.08
$a_0=\Delta\Sigma-3\alpha_s\Delta G/2\pi$	1.0	0.75	0.36 ± 0.24

the quark-gluon system must increase to conserve the total angular momentum. Thus, as more gluons are emitted, both ΔG and L_z will grow, but with opposite signs.

Other quantities of interest are the helicity contributions from the individual quarks. These quantities can be extracted from the measured a_0, but may be subject to possible gluon contributions as in Eq. (18). Allowing for the possibility of gluon contributions, these quark helicities are calculated using

$$\Delta u=\frac{1}{3}(a_0+3F+D)+\frac{1}{2\pi}\alpha_s(Q^2)\Delta G(Q^2),$$

$$\Delta d=\frac{1}{3}(a_0-2D)+\frac{1}{2\pi}\alpha_s(Q^2)\Delta G(Q^2), \tag{19}$$

$$\Delta s=\frac{1}{3}(a_0-3F+D)+\frac{1}{2\pi}\alpha_s(Q^2)\Delta G(Q^2).$$

If we include a contribution of $\Delta G(1\ (\mathrm{GeV}/c)^2)=1.6\pm0.9$ [37], and use $\alpha_s(M_Z)=0.118\pm0.003$ [26], we calculate $\alpha_s\Delta G/2\pi=0.13\pm0.08$ and find good agreement with existing data. This model along with quark-parton model expectations are summarized in Table I and can be compared with data from this experiment in Table XXIX. Note that the value used above for ΔG agrees well with a theoretical prediction based on QCD sum rules [38] which yields $\Delta G(1\ (\mathrm{GeV}/c)^2)=2.1\pm1.0$ and on an earlier parametrization [39] which yields $\Delta G(1\ (\mathrm{GeV}/c)^2)=1.7$.

There are a number of other theoretical models which attempt to explain how the quark helicity is distributed within the nucleon. Non-perturbative effects enhancing the role of intrinsic sea quarks have been proposed by several authors. Halperin and Zhitnitsky [40] argue that a large portion of the nucleon spin comes from charm quarks by adding a term $2\Delta c$ to the a_o term in Eq. (11). Brodsky and Ma [41] contend that asymmetries in the light quark sea could generate the observed $\Delta\Sigma$. The Skyrme model [42] predicts that $\Delta\Sigma=\Delta u+\Delta d+\Delta s=0$ and $\Delta G=0$ and $L_z=1/2$, and should be accurate to $\mathrm{O}(1/N_c)$ where $N_c=3$, the number of colors. Within its uncertainty this is consistent with the small observed value of $\Delta\Sigma$. Other models include the chiral bag model [43], the chiral quark model [32], calculations based on QCD spectral sum rules [44], or Pauli-exclusion principles [45], and also lattice QCD predictions [46–49].

3. The Bjorken sum rule

This sum rule was originated by Bjorken [17] using current algebra and isospin symmetry. It has since been rederived in QCD and is a strict prediction made by this theory. It relates the integral over all x at fixed Q^2 of the difference between $g_1^p(x,Q^2)$ and $g_1^n(x,Q^2)$ to the well-measured neutron beta decay coupling constant $g_A=1.2601\pm0.0025$ [26],

$$\Gamma_1^p(Q^2)-\Gamma_1^n(Q^2)=\int[g_1^p(x,Q^2)-g_1^n(x,Q^2)]dx$$

$$=\frac{1}{6}g_A C_{ns}. \tag{20}$$

An experimental test of this sum rule provides a test of fundamental QCD assumptions. In addition, it is possible to use the measurement to extract a relatively accurate determination of $\alpha_s(Q^2)$ at low Q^2 [on the order of 2 to 10 $(\mathrm{GeV}/c)^2$] [50]. A significant difference from other $\alpha_s(Q^2)$ determinations could indicate the presence of interesting new physics.

4. The Ellis-Jaffe sum rule

The other sum rules of interest for g_1, although less rigorous than the Bjorken sum rule, are the Ellis-Jaffe sum rules [51] which were derived using SU(3) symmetry and assuming the strange sea in the nucleons is unpolarized. These sum rules, including the necessary QCD corrections, follow naturally from Eqs. (11) and (12) with $\Delta s=\Delta G=0$ such that $a_0=a_8=3F-D$:

$$\Gamma_1^p(Q^2)=\int_0^1 g_1^p(x,Q^2)dx$$

$$=\frac{1}{18}[C_{ns}(3F+D)+2C_s(3F-D)],$$

$$\Gamma_1^n(Q^2)=\int_0^1 g_1^n(x,Q^2)dx$$

$$=\frac{1}{9}[-DC_{ns}+C_s(3F-D)]. \tag{21}$$

5. Q^2 dependence: Evolution and higher twist

The quark-parton model does not inherently include gluons, and it is the interaction between the quarks and gluons which generates the observed Q^2 dependence of both the polarized and unpolarized nucleon structure functions. The QCD theory which describes the quark-gluon dynamics gives predictions about how the parton distribution functions (and thus structure functions) evolve in Q^2 in the perturbative limit of small α_s. The Q^2 evolution of the polarized parton densities is governed by the Dokshitzer-Gribov-Lipatov-Altarelli-Parisi (DGLAP) [1] equations which embody the emission of gluons by quarks. This gluon emission is responsible for the leading logarithmic Q^2 dependence. In addition, there are higher-twist contributions to the Q^2 dependence which are suppressed by powers of $1/\sqrt{Q^2}$. Higher

twist corrections to g_1 have been estimated to be small [52–55] while higher twist corrections for g_2 have been estimated to be significant [49,52,56–58]. Fits to $\Delta u(x,Q^2)$, $\Delta d(x,Q^2)$, $\Delta s(x,Q^2)$, and $\Delta G(x,Q^2)$ have been made [35,59] using next-to-leading-order (NLO) DGLAP equations [60]. The results indicate that NLO fits are more sensitive to the strength of the polarized gluon distribution function $\Delta G(x,Q^2)$ than leading order fits.

C. The deep-inelastic spin structure function $g_2(x,Q^2)$

1. Physical interpretation

The literature which discusses the interpretation of g_2 within the naive parton model has been confusing and filled with inconsistencies. Feynman related the quantity $g_T(x) = g_1(x)+g_2(x)=A_2F_1/\gamma$ to the distribution of quark polarizations aligned parallel ($k^{\uparrow}$) and antiparallel ($k^{\downarrow}$) to that of a transversely polarized proton [24,61] by the expression

$$g_T(x)=\sum_i e_i^2 \frac{m_q}{2xM}[k_i^{\uparrow}(x)-k_i^{\downarrow}(x)], \tag{22}$$

where m_q is the quark mass. A more general expression for Eq. (22) was presented by Leader and Anselmino [62] for arbitrary nucleon polarization direction. Jaffe and Ji [24] pointed out that claims [63,64] that g_T is small were generated by setting $m_q=0$ in Eq. (22). Another approach has been to take the quark momenta to be along the longitudinal direction such that $m_q=xM$ [24,62], which yields $g_2(x)=0$. Because of Fermi motion, however, the quarks are off-shell and $m_q\neq xM$ in general. More importantly, it has since been recognized [65] that Eq. (22) is not correct for g_T, and g_T should be replaced in the formula by the twist-2 structure function h_T which is the quark transverse polarization distribution. The quantity h_T is sometimes denoted as h_1 in the literature [65,66]. It turns out that neither g_T nor g_2 can be adequately expressed within the naive quark parton model to yield a useful physical interpretation. In addition, the naive parton model does not include transverse momentum or quark-gluon interactions which are known to be important for g_2, and does not account for Q^2 dependence. Early theoretical advances [25,67–69] in the understanding of g_2 help to solve these problems and serve as a basis for subsequent theoretical work. Among the more recent work are a light-cone parton model [70,71] and an OPE analysis [24,72], which indicates that there are three components (up to twist-3) contributing to g_2. These components include the leading twist-2 part $g_2^{WW}(x,Q^2)$ [73], coming from the same set of operators that contribute to g_1, another twist-2 part coming from the quark transverse-polarization distribution $h_T(x,Q^2)$, and a twist-3 part coming from quark-gluon interactions $\xi(x,Q^2)$:

$$g_2(x,Q^2)=g_2^{WW}(x,Q^2) - \int_x^1 \frac{\partial}{\partial y}\left(\frac{m_q}{M}h_T(y,Q^2)+\xi(y,Q^2)\right)\frac{dy}{y}. \tag{23}$$

The term containing $h_T(y,Q^2)$ is usually neglected because it is suppressed by the quark mass m_q, and the g_2^{WW} expression of Wandzura-Wilczek [73] is given by

$$g_2^{WW}(x,Q^2)=-g_1(x,Q^2)+\int_x^1 \frac{g_1(y,Q^2)}{y}dy. \tag{24}$$

2. OPE sum rules and the twist-3 matrix element

Keeping terms up to twist-3, the OPE analysis of g_1 and g_2 yields an infinite number of sum rules:

$$\Gamma_1^{(n)}=\int_0^1 x^n g_1(x,Q^2)dx=\frac{a_n}{2},\quad n=0,2,4,\ldots,$$

$$\Gamma_2^{(n)}=\int_0^1 x^n g_2(x,Q^2)dx=\frac{1}{2}\frac{n}{n+1}(d_n-a_n),\quad n=2,4,\ldots, \tag{25}$$

where a_n are the twist-2 and d_n are the twist-3 matrix elements of the renormalized operators. The OPE only gives information on the odd moments of the spin structure functions. Note that contributions involving m_q/M [see Eq. (23)] have been left out of Eq. (25) as have target mass effects discussed below. The twist-3 matrix elements follow from Eq. (25):

$$d_n=2\int_0^1 x^n\left[g_1(x,Q^2)+\frac{n+1}{n}g_2(x,Q^2)\right]dx,\quad n=2,4,\ldots,$$

$$=2\int_0^1 x^n\left(\frac{n+1}{n}\right)\overline{g_2}(x,Q^2)dx,\quad n=2,4,\ldots, \tag{26}$$

where $\overline{g_2}=g_2-g_2^{WW}$. We see from Eq. (26) that if all $d_n=0$ then g_2 is completely determined by g_1 because there are an infinite number of sum rules. This is how the quantity g_2^{WW} was originally derived.

There are a number of theoretical predictions for d_2 for both proton and neutron targets [49,52,56–58]. Some are based on bag models [56,57], others on QCD sum rules [52,58], and there is also a lattice QCD calculation [49]. Many of these models have predicted large values for d_2 which means there could be significant twist-3 contributions to g_2. This makes the study of g_2 particularly interesting.

3. The Burkhardt-Cottingham sum rule

The Burkhardt-Cottingham sum rule [74] for g_2 at large Q^2, namely

$$\int_0^1 g_2(x)dx=0, \tag{27}$$

was derived from virtual Compton scattering dispersion relations. This sum rule does not follow from the OPE since the $n=0$ sum rule is not defined for g_2 in Eq. (25). The validity of the Burkhardt-Cottingham sum rule relies on g_2 obeying Regge theory at low x, which may not be a good assumption. A non-Regge divergence of g_2 at low x would

invalidate this sum rule [23,24], although such a divergence could be very difficult to detect experimentally.

4. Target mass effects

The OPE sum rules as given in Eq. (25) were derived in the limit $M^2x^2/Q^2 \to 0$. These target mass effects can become significant when M^2/Q^2 is of order unity which is certainly the case for a subset of the data presented in this paper. These target mass effects for polarized electroproduction have been determined [75,76]. The corrected Bjorken sum rule derived from these formulas is given by [76]

$$\frac{1}{9}\int_0^1 dx \frac{\xi^2}{x^2}[5+4\sqrt{1+4M^2x^2/Q^2}][g_1^p(x,Q^2) - g_1^n(x,Q^2)] - \frac{4}{3}\int_0^1 dx \frac{M^2\xi^2}{Q^2}[g_2^p(x,Q^2)-g_2^n(x,Q^2)] = \frac{1}{6}g_A C_{NS}, \quad (28)$$

where the Nachtmann variable $\xi = 2x/(1+\sqrt{1+4M^2x^2/Q^2})$. This sum rule is now dependent on g_2. The size of the target mass effects [77,78] to the uncorrected Bjorken sum rule formula are estimated to be of the same magnitude as higher-twist effects which are typically small. The target mass effects for the g_2^{WW} calculation [missing in Eq. (24)] have been investigated and are negligible for our kinematics [79].

D. Resonance region polarized structure functions

The values of A_1 in the resonance region are a combination of the asymmetries for individual resonances and for the nonresonant background. Resonance helicity amplitudes $A_{1/2}$ and $A_{3/2}$ are reasonably well measured at $Q^2=0$ for the prominent resonances [26]. Sparse data exist also for virtual photons [80]. The excitation of the $\Delta(1232)$ resonance (spin-$\frac{3}{2}$) includes both $\frac{1}{2}$ and $\frac{3}{2}$ spin projections. At low Q^2 the $\Delta(1232)$ excitation is expected to be primarily a magnetic dipole transition for which $A_{3/2}/A_{1/2}=\sqrt{3}$ and $A_1=(|A_{1/2}|^2 - |A_{3/2}|^2)/(|A_{1/2}|^2+|A_{3/2}|^2)=-\frac{1}{2}$. For real photons $A_{3/2}/A_{1/2}=1.064\sqrt{3}$ [26]. Perturbative QCD predicts that the ratio $A_{3/2}/A_{1/2}$ should go as $1/Q^2$ and A_1 should approach unity as $Q^2 \to \infty$. However, a recent analysis of pion electroproduction [81] data shows that the magnetic dipole transition still dominates at $Q^2=3.2\ (\mathrm{GeV}/c)^2$. On the other hand, the $S_{11}(1535)$ resonance has no spin-$\frac{3}{2}$ projection, so A_1 should be unity at all Q^2. Data [80] from Bonn, Daresbury and DESY have been used to extract $A_{1/2}$ and $A_{3/2}$ up to $Q^2=3\ (\mathrm{GeV}/c)^2$ for the S_{11}, D_{13}, and F_{15} resonances. Because of the large uncertainties of these extractions, our knowledge of the Q^2 dependence of the helicity amplitudes is still rudimentary. The asymmetries A_1 for both D_{13} and F_{15} make a transition from $A_1 \approx -1$ to $A_1 \approx 1$ somewhere in the range $0<Q^2<3\ (\mathrm{GeV}/c)^2$ [80].

Less is known about σ_{LT} and A_2. The positivity limit $A_2 < \sqrt{R(x,Q^2)}$ constrains A_2. The world average value [82] for R in the resonance region is 0.06 ± 0.02 for $1<Q^2<8\ (\mathrm{GeV}/c)^2$ and $W^2<3\ \mathrm{GeV}^2$. Since this is smaller by half than the deep-inelastic fit to $R(x,Q^2)$ [83] extrapolated into the resonance region, one might argue that $R(x,Q^2)$ for the resonances themselves is small. However, little is known for $Q^2<1.3\ (\mathrm{GeV}/c)^2$.

A complete mapping of $g_1(x,Q^2)$ at low Q^2 where the resonances dominate is useful for two reasons. First, these data provide important input for radiative corrections of the deep-inelastic data. Second, the evolution of the integral (defined to exclude elastic scattering) $\Gamma_1(Q^2)=\int_0^1 g_1(x,Q^2)dx$ for $Q^2 \to 0$ should be determined by the Gerasimov-Drell-Hearn (GDH) sum rule [84] for real photons:

$$\int_{\nu_{th}}^{\infty} 2\sigma_{TT} d\nu/\nu = -\frac{2\pi^2\alpha\kappa^2}{M^2} \quad (29)$$

in which ν is the photon energy, ν_{th} is the threshold energy for pion production, κ is the nucleon anomalous magnetic moment, and M is the nucleon mass. A simple change of variables from ν to x in Eq. (29) and a reformulation of σ_{TT} in terms of g_1 and g_2 yields

$$\lim_{Q^2 \to 0} \frac{\Gamma_1(Q^2)}{Q^2} = -\frac{\kappa^2}{8M^2}. \quad (30)$$

One important feature of Eq. (30) is the sign. Γ_1^p for the proton is positive for Q^2 above $3\ (\mathrm{GeV}/c)^2$ as measured in the deep-inelastic regime. However, the GDH sum rule predicts that Γ_1^p should become negative at small Q^2. This implies that somewhere in the region $0<Q^2<3\ (\mathrm{GeV}/c)^2$, Γ_1^p must cross zero. Exactly where this occurs depends crucially on the Q^2 evolution of the resonance helicity amplitudes which are presently not well known. Predictions about how $\Gamma_1(Q^2)$ goes from the deep-inelastic values to the GDH limit have taken one of two paths: (1) theoretically motivated interpolation and (2) computations that include all available knowledge of the resonance behavior. Both need to be checked with direct measurements of $\Gamma_1(Q^2)$ at low Q^2.

Recent theoretical work [85] indicates that at low Q^2, $\Gamma_1(Q^2)$ corrected to include the elastic contribution,

$$\Gamma_1^{el}(Q^2) = \frac{1}{2}F_1(Q^2)[F_1(Q^2)+F_2(Q^2)], \quad (31)$$

provides the twist-4 $(1/Q^2)$ corrections to the Ellis-Jaffe sum rule. F_1 and F_2 in Eq. (31) are the Dirac and Pauli elastic form factors (not the deep-inelastic structure functions).

III. THE EXPERIMENT

The goal of the E143 experiment was to determine the longitudinal and transverse cross-section asymmetries via deep-inelastic scattering of longitudinally polarized electrons from polarized protons and deuterons. Over a period of three calendar months data were taken at beam energies of 29.13 GeV (122 million events), 16.18 GeV (56 million events) and 9.71 GeV (58 million events). The longitudinal asymme-

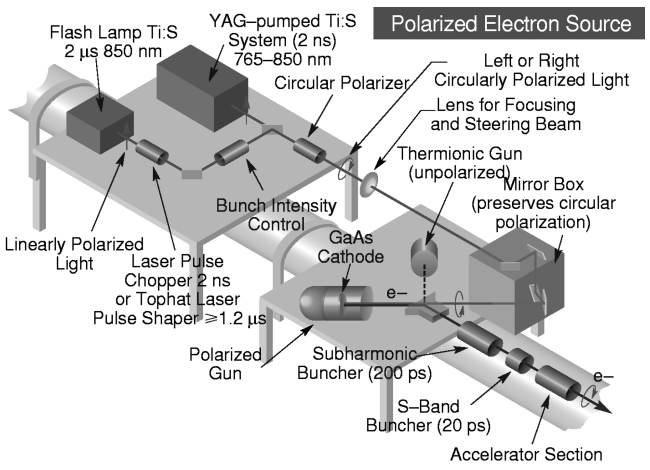

FIG. 1. The layout of the lasers and the polarized electron gun at the accelerator injector is shown schematically. Two types of lasers are used, one for the SLC, which produces two 2 nsec pulses separated by 61 nsec, and one for the fixed target experiments, which produces one pulse 2 μsec long.

try $A_{\parallel}$ was obtained with the target polarization parallel to the beam momentum, whereas the transverse asymmetry $A_{\perp}$ (at $E=29.1$ GeV only) was obtained with the target polarization transverse to the beam momentum (right or left of the beam).

The experimental apparatus employed consisted of five components: the polarized source, the accelerator and beam transport, the Møller polarimeter to measure the beam polarization in the end station A (ESA), the polarized proton and deuteron target, and the two spectrometer arms to detect the scattered electrons. These components are discussed in the sections which follow.

A. The SLAC polarized electron source

A polarized electron source for the SLAC linear accelerator was first developed in the early 1970s for experiments on the spin structure of the proton. Since 1978 the SLAC polarized electron source has been based on the principle of laser photoemission from a gallium arsenide (GaAs) photocathode. Strained GaAs photocathodes, which effectively doubled the polarization obtainable from an unstrained GaAs photocathode, were developed in 1991 [86,87] and first used in a SLAC experiment in 1993. The design and operational characteristics of the SLAC polarized electron source are fully described in Ref. [88].

Figure 1 is a schematic of the layout of the laser and gun structure at the SLAC injector. Electrons are photo-emitted from a GaAs photocathode by illuminating the surface with a laser. The electrons are polarized with a helicity defined by the sign of the circular polarization of the incident laser light. Spin reversals are achieved at the source by reversing the circular polarization of the laser light with a Pockels cell. The pattern for the sign of the polarization is chosen to be a known pseudo-random sequence, permitting validation of the sign of each pulse in the offline data stream.

The polarization of the electrons is a consequence of the band structure of GaAs and the angular momentum selection rules that apply to this system. The presence of strain changes the lattice constant of the GaAs, shifts the energy levels, and breaks a spin state degeneracy in the valence band, changing the theoretical maximum electron polarization from 50% to 100%. Excitation by circularly polarized light near the band gap edge ($\lambda \approx 850$ nm) will then result in only one set of spin states populating the conduction band provided the strain is sufficiently large. The strain in the active GaAs layer is achieved by growing a 100 nm thick epitaxial layer of GaAs on a substrate of $GaAs_{(1-x)}P_x$ ($x=0.28$). The lattice spacing for the GaAsP is about 1% smaller than for GaAs, and the resulting lattice mismatch puts the GaAs epitaxial layer under a compressive strain sufficiently high to remove the spin state degeneracy. Under these conditions one expects that photo-emitted electrons will have a polarization close to the theoretical limit of 100%. In practice, the electron polarization is less than the theoretical limit due to effects such as non-ideal photocathode strain and depolarization as the electrons diffuse to the photocathode surface. The electron polarization averaged 85% for the E143 experiment.

The laser system was designed and built at SLAC. It consisted of a flash-lamp pumped titanium sapphire rod, producing light pulses which were optically chopped to a 2.3 μsec long pulse. The laser beam was transmitted through a lens system which allowed for steering and focusing on the cathode. For the E143 experiment, the amount of laser power available was larger than needed, so the power was attenuated to about 10 watts peak, yielding approximately 4×10^9 electrons per pulse. At this low electron intensity, the accelerator control system was unable to sense the presence of beam. To allow the accelerator controls to operate, the beam was intentionally intensified to about 2×10^{10} in one of the 120 pulses generated per second. This ''witness pulse'' was then sent into a beam dump before reaching the target, and the experiment operated on the remaining 119 pulses per second.

Possible systematic errors associated with reversal of the electron spin are important to this type of experiment. Correlations between beam current, beam energy, beam positions, and beam angles on the target were available to the experimenters on a short time basis from beam monitors. For this laser-driven photoemission source, the reversal of the laser polarization is sufficiently free of unwanted effects such that all systematic errors from the source were negligible.

B. The electron beam

1. Production and transport

The electrons produced by the polarized source were accelerated to energies between 9 and 30 GeV in the linear accelerator. The electrons were then deflected through an angle of 24.5° in the A-line beam transport and were directed onto the polarized target in the ESA.

Because of its anomalous magnetic moment, the spin of the electron precesses by an angle larger than that of the bend angle of the beam, according to the formula:

$$\Delta\phi = \pi\left(\frac{24.5°}{180°}\right)\left(\frac{g-2}{2}\right)\left(\frac{E}{m}\right) = \left(\frac{E}{3.237}\right)\pi, \qquad (32)$$

where g is the gyromagnetic ratio, E is the energy (in GeV), m is the mass of the electron, and $\Delta\phi$ is the angle between the electron spin and the momentum at the target. When $\Delta\phi$ is an integral multiple of π, the electron spin is longitudinal at the target. The experiment was run at energies of 9.71, 16.18 and 29.13 GeV, corresponding to 3π, 5π and 9π respectively. By varying the energy around the nominal value and measuring the longitudinal polarization in the Møller polarimeter, we verified that the chosen energy produced the maximum polarization.

2. Beam monitoring

The incident flux of electrons was measured independently in two identical precision toroidal charge monitors in the ESA. These were frequently calibrated with a known charge and agreed to better than 1%. The response of the toroids is independent of the polarity of the beam.

The position of the beam at the target was monitored in two devices: a traveling-wave radio-frequency beam position monitor which was non-interfering and was placed just in front of the target, and a pair of secondary emission foil arrays with 1 mm spacing located 10.8 m downstream from the target. The former provided a direct measurement of beam centroid position, and was used in an automatic feedback system to keep the beam on target; the latter allowed a measurement of both the position and the transverse dimensions of the beam by comparing the charge collected on the individual foils.

3. Beam rastering

To minimize effects such as target depolarization from local beam heating and radiation damage, the beam was moved or ''rastered'' across the face of the target. The beam position was changed between pulses by means of a pair of air-core magnet coils located 67 m upstream of the target. The lack of iron in these magnets allowed the fields to be quickly changed under computer control. The beam at the target was rastered on a grid with a spacing of 1.2 mm inside a circle of radius 10.8 mm for a total of 253 points. Thus, each point in the target was illuminated only once every 2.1 seconds. The raster pattern skipped every other point and row, so that subsequent pulses did not overlap, and the entire raster pattern was completed in four passes. Because the dimensions of the beam (Gaussian σ of 2 mm horizontally and 1 mm vertically) were comparable to the raster spacing, the overall illumination of the target was quite uniform inside the circle of the raster.

4. The beam chicane

For the measurement of g_2, the target was rotated by 90° so that the target nucleons were polarized transversely to the beam direction in the scattering plane. In this configuration, the electrons in the beam passed through $\int Bdl = 1.52$ T-m as they traversed the target. This was enough to deflect them through an angle of 0.90° at 29.1 GeV and to rotate the polarization vector through an angle of 60°. As a result, the beam after the target would have no longer been parallel to the nominal beam-line, and in fact would have been about 30 cm low at the exit of the ESA. More significantly, the deep-inelastic scattering would have taken place at a different average angle and longitudinal polarization than in the parallel case.

To compensate for the effects of this magnetic field, we inserted four identical dipole magnets (the chicane) into the beam-line, three upstream and one downstream of the target. The first magnet deflected the beam down by 0.45°, and the second pair bent the beam back up by twice this amount. This caused the beam to arrive at the center of the target with both the momentum and polarization vectors horizontal. After exiting the target, the beam was tilted downward, and the fourth magnet returned the beam to the horizontal so that it left the ESA parallel to the nominal beam-line displaced vertically by only 3.5 cm at 29.1 GeV.

C. Beam polarimetry

A Møller polarimeter was used to measure the beam polarization during the E143 experiment. This is a practical and reliable approach based on $\vec{e}+\vec{e}\rightarrow e+e$ scattering, a spin-dependent QED process with a large cross-section and analyzing power. The expected cross-section asymmetry can be calculated with high precision [89] and is not significantly modified by radiative processes [90].

For a beam with longitudinal polarization P_B and target with longitudinal polarization P_T, the beam polarization is measured by comparing the relative cross-section asymmetry for beam and target spins aligned parallel ($\uparrow\uparrow$) and anti-parallel ($\uparrow\downarrow$):

$$\epsilon = \frac{d\sigma^{\uparrow\uparrow}/d\Omega - d\sigma^{\uparrow\downarrow}/d\Omega}{d\sigma^{\uparrow\uparrow}/d\Omega + d\sigma^{\uparrow\downarrow}/d\Omega} = A_{ZZ}(\theta)P_B P_T. \qquad (33)$$

The relative cross-sections are determined by detecting either of the scattered electrons or both in coincidence.

1. Layout

A schematic of the polarimeter is shown in Fig. 2. The major components are a polarized electron target, an acceptance-defining collimator, a dipole magnet spectrometer, and two independent detector systems. One system detected the Møller electrons in coincidence, whereas the other integrated the single electrons over the duration of the beam spill.

The polarized electron target consisted of six magnetized ferromagnetic foils of different thickness which could be moved into the beam. The foils were magnetized to near saturation by Helmholtz coils providing nearly 100 gauss at the target center. The permendur (49% Fe, 49% Co, 2% V) foils were 3 cm wide and varied in thickness from 20 μm to 150 μm. The target electron polarization (typically 0.082) was determined to a relative accuracy of 1.7% [91] from foil magnetization measurements.

The tungsten collimator which was 20 radiation lengths thick (see Fig. 2) had a central opening to allow the main

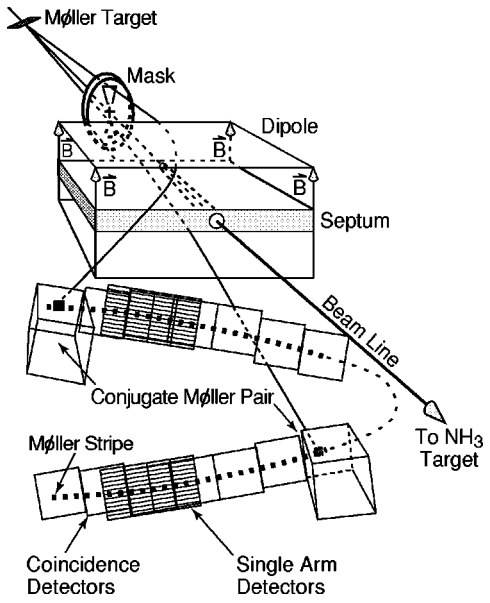

FIG. 2. The layout of the Møller polarimeter systems used in the E143 experiment (not to scale).

beam to pass and wedge shaped apertures of constant azimuthal acceptance (0.2 radian top, 0.22 radian bottom) above and below the beam-line to select Møller electrons scattered transverse to the bend plane of the downstream dipole magnet. The vertical acceptance was 3.6–9 mrad in the lab (corresponding to 70–116° in the center-of-mass). The 2.1 T-m dipole field separated the scattered electrons according to momenta. Since Møller scattering is elastic, the x and y position of the scattered electrons at the detector plane are correlated as shown in Fig. 2.

The detector hut was situated 27 m downstream from the Møller target. The single-arm detector package of three radiation lengths of lead and a single plane of position-sensitive silicon detectors was placed immediately in front of the coincidence detectors. The coincidence package consisted of two arrays of seven lead glass blocks (SF-6), each with a 10×10 cm^2 entrance area and 25 cm of depth ($\sim$15 radiation lengths).

2. The measurements

Measurements of the beam polarization were performed every one to two days. Each measurement period typically consisted of four runs using two target foils (thin and thick) and opposite target polarization directions. This made it possible to look for rate or helicity dependent effects in the data. For polarization measurements, the beam rastering was turned off and the beam focus was moved to the Møller target. Otherwise, the beam conditions were identical to that of the main experiment. Data were obtained from almost 200 runs over a range of luminosities (more than a factor of 8) through different combinations of foil thickness and beam current. The coincidence polarimeter obtained a typical statistical precision of 0.010 (absolute) per run whereas the single arm polarimeter achieved 0.019 per run. Both detector systems took data at 29.1 and 16.2 GeV. The single arm collected data with the 9.7 GeV beam.

3. The coincidence polarimeter

The segmented lead glass arrays provided good energy and timing information and made it possible to accommodate the high instantaneous rates of several 10 s of MHz characteristic of the low duty factor (10^{-4}) at SLAC. The combination of Čerenkov light in the glass blocks, fast photomultiplier tubes, and a clipping circuit resulted in signal pulse widths as narrow as five nanoseconds. The signals were fed into an Ortec 935 constant fraction discriminator with the threshold set at 30–40% of typical Møller signal amplitude. The discriminator output was then fed into a fast multiplexing circuit with a fanout to three or four time to digital converter (TDC) channels. The time of each event was recorded by a LeCroy 2277 multi-hit TDC which has a least significant bit time of one nanosecond. The multiplexor was required to decrease the dead-time and increase the maximum hit capability of the individual TDC channels. A laser pulser, triggered randomly $\leqslant$1/spill, was fed into each detector block simultaneously through fibers to provide both time calibration and detector dead-time information for the analysis.

The data were recorded on tape on a spill-by-spill basis as a series of event times and corresponding TDC channels. The analysis identified coincidence events by the arrival of single event times within a predefined time window of ±4 ns, determined by the resolution of the TDC's. Frequently, the analysis encountered ambiguous coincidence pair combinations where a single event of one detector could be combined with events in two or more other detectors. Such ambiguities arose as a result of cross-talk between adjacent detectors due to shower sharing or due to random coincidences, particularly at higher luminosities. In the case of ambiguities, the cluster of all possible coincidences was subjected to a decision making routine which selected the most probable combinations of events. In the case of cross-talk events the full weight of the single coincidence event was shared with the adjacent coincidence pairs. Background contributions consisted of random coincidences between Møller or Mott type electron events. Their contribution, typically $\leqslant$1% was estimated from the product of the singles rates in each conjugate detector.

The dead-time measurement was obtained using the laser pulser system which sent a known pulse to all 14 detectors simultaneously. The efficiency at which both detectors of a pair saw the pulser event yielded the live-time for that pair. It was also necessary to correct for the possibility of two Møller events occurring in a given pair within the same coincidence window. In such a case the system is only capable of seeing one of the pairs, an inefficiency which would be unaccounted for in the dead-time correction. To correct for this effect an estimate of the number of Møller coincidence events occurring during the pulser event was added to the known number of pulser events for each pair.

A typical Møller coincidence time difference spectrum is shown in Fig. 3(a). Two views of a typical distribution of coincidence events in the two detector arms are given in Figs. 3(b)–(c) for a run at 29 GeV. True Møller events were kinematically restricted to occur only in 11 (9 for the 16 GeV

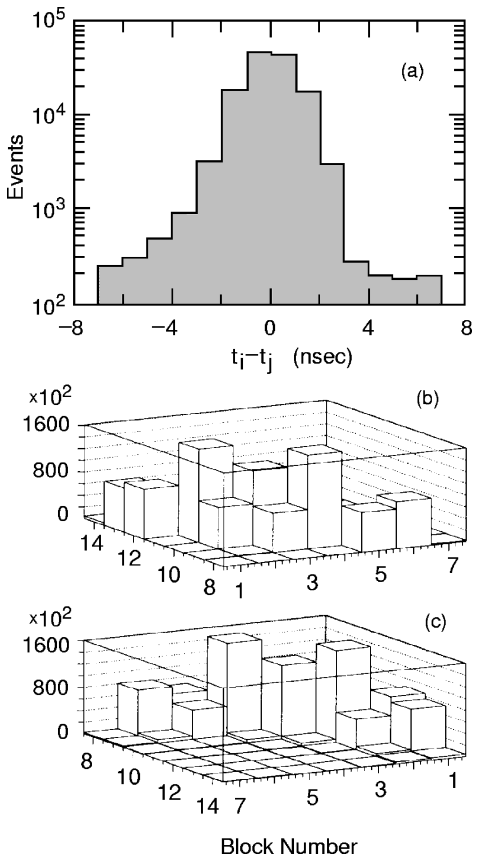

FIG. 3. (a) A typical Møller coincidence event time difference spectrum. (b)–(c) Two views of the distribution of coincidence events in the $7\times7=49$ possible combinations. (c) shows the hidden back-side of (b). True Møller events were constrained to occur in the crest.

data) of the possible (7×7) 49 pairs. Radiative effects did allow some true Møller coincidences to occur on the low momentum side of the ridge seen in Fig. 3(c), but these events were not considered in the total event yield due to poor signal-to-noise ratio and greater uncertainties in the analyzing powers.

The beam polarization for each coincidence pair was determined from the asymmetry in the yield corrected for background, dead-time, charge asymmetry, the effective analyzing power of each pair, the target polarization and the target angle. The polarization for a run was taken from the weighted average over all the pairs.

A Monte Carlo analysis [92] was used to determine the effective analyzing powers of each coincidence pair and to evaluate the sensitivity of the analyzing powers to possible systematic influences such as the atomic motion of the target electrons [93] and typical shifts in the beam position or focus. The analyzing powers were found to range from 0.776 to 0.690 for the different pairs. The effect of the target electron motion was to increase the average analyzing power by $<0.5\%$. Typical beam parameter shifts resulted in changes to the average analyzing power within $\pm0.6\%$. Since only one set of analyzing powers was used at each beam energy, the $\pm0.6\%$ variation was included as a source of systematic error. The large acceptance of the detectors reduced the sensitivity of the analyzing powers to these systematic influences.

The possibility of rate dependence was investigated in two studies. One study compared low and high luminosity runs taken during a run set where little variation in polarization was expected during the set. In this study the internal agreement between all measurements of a run set was very good, resulting in an average χ^2 per degrees of freedom (DF) of 1.1 for all the run sets. Another study tested the effectiveness of the analysis routine in dealing with ambiguities in the data which were most prevalent at high luminosity. Data taken from subsequent spills of a low luminosity run were artificially superimposed to create a fictitious spill of high luminosity. After imposing the detector dead-time on the single events the data were analyzed as a normal run, and the yields could be compared with the original luminosity analysis. In both studies it was possible to rule out a rate dependence at better than $\pm0.5\%$.

Despite the excellent agreement of the polarization results within a run set, a large fluctuation in the average polarization values obtained from each coincidence pair was observed. Although the sources of these fluctuations likely cancel in the average, their origins are not clear. As a result a maximum error contribution of 1.3% was included. This contribution reduced the χ^2 per DF of the pair-dependent polarization distribution to unity. This uncertainty was combined in quadrature with the uncertainties estimated for the analyzing powers and the limit on a possible rate dependence to obtain a total systematic uncertainty of 1.5% for the coincidence polarimeter measurement.

4. The single-arm polarimeter

The single arm detectors had four silicon pad detectors above and below the beam height. A lead converter absorbed soft photon backgrounds and amplified the Møller signal. Each detector consisted of two 4 (x) by 6 (y) cm silicon devices approximately 300 μm thick. Each device was segmented into 7 pads (channels) 8.70 mm wide and 40 mm long. Only 12 contiguous channels were instrumented in each detector. The detectors were tilted by $-10.5°$ (top) and $+11.0°$ (bottom) to align the channels along the Møller scattered electron stripe. Since each detector was formed from two silicon devices there was a 5.3 mm gap between channels seven and eight.

The silicon detector channels were connected to 96 charge sensitive preamplifiers which integrated over the entire 2300 ns beam pulse. The preamplifier outputs were brought into analogue to digital converters (ADCs) to measure the peak of the preamplifier signal and were recorded together with the sign of the beam polarization for each beam pulse.

The Møller analysis proceeded through two steps. The first-pass analysis calculated average pedestal subtracted pulse heights and errors for each channel from the pulse-by-pulse data. Separate averages were made for pulses tagged by right (R) and left (L) handed polarization bits. Correlations between channels were calculated and recorded. A very loose beam current requirement was made before including the pulse in the overall averages. A summary file containing

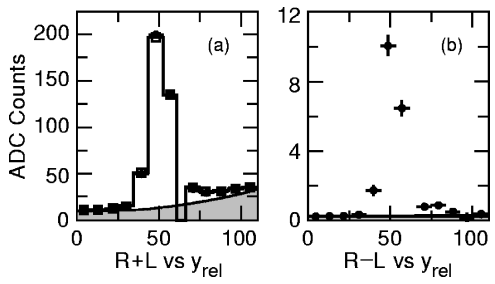

FIG. 4. Typical measured single-arm Møller line-shapes in detector 7 at 29.1 GeV. The (R+L) data (points), (R+L) fit (histogram), and (R+L) background (shaded region) are plotted in (a) versus the relative y position of the channel. The (R−L) data (points) and (R−L) background (shaded region) are plotted in (b).

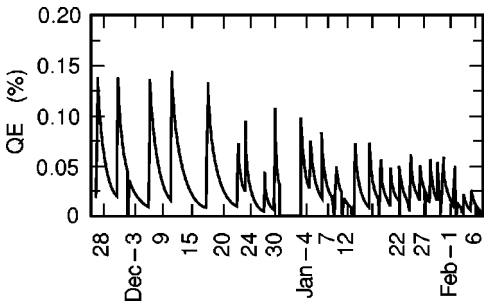

FIG. 5. Variation of the quantum efficiency (QE) of the polarized source over the course of the E143 experiment.

the ADC averages and errors as well as useful beam and polarimeter parameters was written for each run. A second-pass analysis read the summary file, applied channel by channel gain corrections, and formed sum (R+L) and difference (R−L) averages and errors for each channel. Typical (R+L) and (R−L) line-shapes are shown in Fig. 4 for data at 29.1 GeV.

The background (B) under the unpolarized (R+L) Møller scatters was estimated by fitting the (R+L) line-shape to an arbitrary quadratic background plus the line-shape expected from unpolarized Møller scattering. The technique for estimating the unpolarized line-shape used the observed (R−L) line-shape and angular smearing functions [91] to generate a predicted (R+L) line-shape for Møller scatters. The observed (R+L) distribution was then fit by this predicted line-shape and a quadratic background. Since the observed (R−L) line-shape is already broadened by multiple scattering in the target material, beam windows, air, and helium, only corrections to the line-shape which are different [93] for scatters from polarized and unpolarized target electrons are included in the smearing function.

An analyzing power for each detector was calculated from the target polarization and the expected Møller asymmetry determined by Monte Carlo simulations of the scattering process [92] and detector response. The effect of the target electron momentum distribution [93] was to modify the expected asymmetries by 1.4%. The measured asymmetry for each detector was calculated from the ADC averages by

$$A_{meas.}=\frac{\Sigma_i(R-L)_i-\Sigma_i(\mathrm{B})_{R-L}}{\Sigma_i(R+L)_i-\Sigma_i(\mathrm{B})_{R+L}}, \tag{34}$$

where the sum is over the central five channels including the Møller peak. The (R−L) background was estimated by averaging the channels far from the Møller peak. The (R+L) background subtraction increased the measured asymmetry by 17–24%. The full covariance matrix calculated from the pulse-by-pulse data was used to determine the statistical error of A_{meas}. The beam polarization was calculated from the measured asymmetry divided by the analyzing power.

To check for possible systematic biases in the single arm analysis, both the number of channels included in the sum over the Møller peak and the shape of the background fit to the unpolarized (R+L) line shapes were varied. From the observed spread in calculated polarizations, the sensitivity of the single arm analysis to the choice of fit parameters was estimated to be 1.3%. The polarization determined individually by each detector agreed with the overall mean within statistical errors. The total systematic error of the single arm analysis includes contributions from the detector analyzing power, known to $\approx 0.5\%$, possible nonlinearities in the preamplifier and ADC response which could change the computed polarization by $\leqslant 1.0\%$, and the sensitivity to analysis parameters, 1.3% as discussed above. The total systematic error of the single arm analysis is estimated to be 1.7%.

5. Results

The polarization values measured by the single and coincidence arm polarimeters were in good agreement, although the results from the coincidence system were on average 0.6% lower than the single arm. This difference is well within the independent systematic errors of the two polarimeters. Both systems measured the same polarization dependence on the quantum efficiency of the polarized source, resulting in a linear decrease of source polarization with increasing quantum efficiency. The polarized source quantum efficiency time history is shown in Fig. 5. The variations in polarized source quantum efficiency were related to the frequent cesiation treatments which were applied to the source in order to maintain the source quantum efficiency at an acceptable level.

To obtain the beam polarization for the main analysis, the average polarization value for each run set was computed separately for each polarimeter. The results from both polarimeters are shown in Fig. 6 plotted as a function of source quantum efficiency. The plotted errors are a combination of the computed statistical errors and an additional 0.8% systematic error to account for non-statistical fluctuations in the data.

A linear fit to the single arm and coincidence data as a function of polarized source quantum efficiency (QE) yields:

$$P_B=(0.866-0.34\times \mathrm{QE})\pm 0.003\pm 0.022, \tag{35}$$

where the first error term is statistical while the second and dominant term is systematic. The systematic error includes a contribution of $\pm 0.8\%$, as discussed above, a $\pm 1.6\%$ contribution from the average of the single arm and coincidence

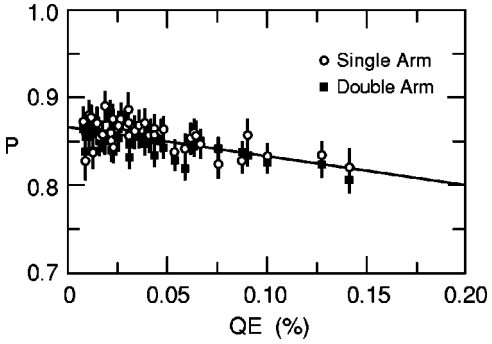

FIG. 6. Beam polarization versus QE for the the single (circles) and double-arm (squares) polarimeter systems.

Møller systematic errors, and a $\pm 1.7\%$ contribution from the uncertainty assigned to the target foil polarization. The resultant systematic error is $\pm 2.5\%$.

D. The polarized target

The polarized target required a high-power ^{4}He evaporation refrigerator operating near 1 K, and a 5 T superconducting split pair magnet.[1] The target material, frozen ^{15}N ammonia, was polarized using dynamic nuclear polarization (DNP). A schematic diagram of the target is shown in Fig. 7 [94]. The magnet is shown with its field direction along the beam momentum direction. The refrigerator is positioned vertically and along the axis of the magnet. It is connected to a large Roots blower pumping system. The target insert lies along the central axis of the refrigerator. This insert was slid up and down to position any one of four targets in the beam. The targets were (from the top position) $^{15}ND_3$, $^{15}NH_3$, an empty cell, and either carbon or aluminum. A fifth position having no target was also available. The target insert also carried coaxial cables for the NMR measurement, a waveguide to transmit microwaves to the target(s) for DNP, and various temperature sensors. A diagram of the target insert is shown in Fig. 8.

1. DNP and ammonia

The DNP process for polarizing protons, deuterons, or any nucleus possessing a magnetic moment, requires temperatures of ~ 1 K or less and large magnetic holding fields. For thermal equilibrium at 1 K and 5 T, the proton polarization is only about 0.5%. However, the polarization of the ''free'' electrons, associated with the paramagnetic radicals introduced into the target material, is greater than 99%. The electron polarization can be transferred to the proton through a hyperfine transition by irradiating the target with microwaves at appropriate frequencies. The two polarization directions for the proton are reached by irradiation at frequencies slightly above or below the electron Larmor frequency, ≈ 140 GHz at 5 T. Details of the DNP process can be found in the literature, e.g., Abragam and Goldman [95] or Borghini [96]. In our case the magnetic field was held at 4.87 T to match the frequency range (136–137 GHz) of the microwave tube[2] being used.

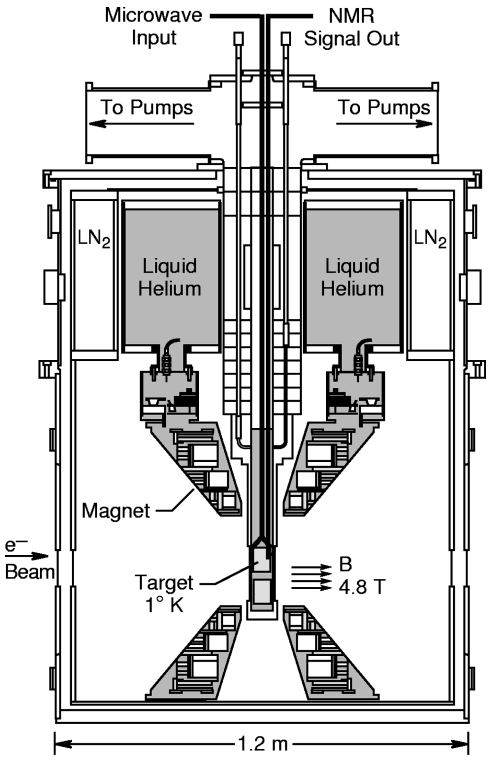

FIG. 7. E143 target schematic.

Ammonia was chosen as the target material because of its relatively large dilution factor compared to most other polarized target materials, its high polarizability, and its resistance to radiation damage. Furthermore, ^{15}N ammonia (spin $\frac{1}{2}$) was chosen over ^{14}N (spin 1) because in ^{15}N the spin is carried by an unpaired proton, in contrast to ^{14}N where the spin is carried by a proton-neutron pair. Using $^{15}NH_3$ reduces the systematic errors on the proton spin structure functions by eliminating unwanted contributions from the neutron asymmetry. In addition, the ^{15}N polarization is easier to measure.

The $^{15}NH_3$ and $^{15}ND_3$ targets were both prepared in the same way: First, the ammonia gas was slowly frozen in a test tube; the resulting solid lump of ammonia ice was crushed while immersed in liquid nitrogen and sifted to select granules of approximately 2 mm size. Smaller pieces were recycled in the same apparatus.

The paramagnetic radicals necessary for DNP were introduced by irradiation using various electron beams. Each sample was immersed in liquid argon and given a dose of about $3-5\times 10^{16}$ electrons cm^{-2}. Targets for E143 were irradiated at Bates (at an electron energy of 350 MeV), at the Naval Postgraduate School, Monterey (65 MeV), and at the High Energy Physics Laboratory at Stanford (30 MeV). Samples of ^{14}N ammonia were irradiated at Saskatoon (250

[1]Oxford Instruments, Eynsham, UK.

[2]CPI, Georgetown, Ontario, Canada.

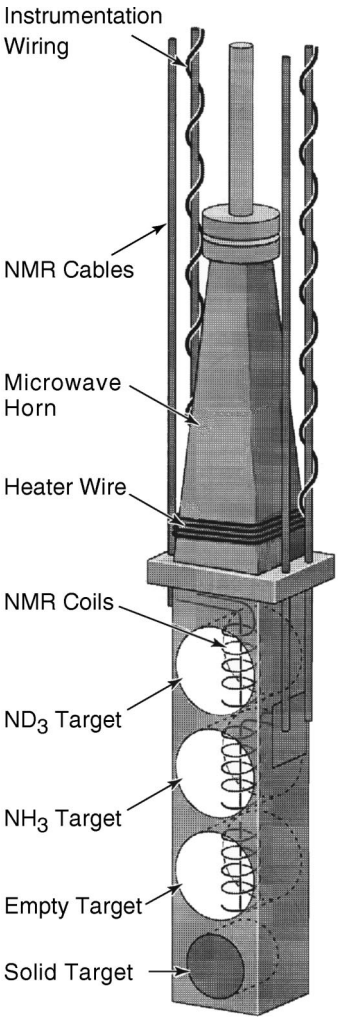

FIG. 8. Target insert schematic.

MeV) for the initial tests. All irradiated samples were packed into thin walled (0.0127 cm) torlon cylinders with 0.0025 cm aluminum end-cap windows. Each cylinder was 3 cm long and 2.5 cm in diameter, and contained two NMR coils made from 70/30 Cu/Ni tubing of 0.5 mm outer diameter and 0.0178 cm wall thickness. A straight piece of tubing was used to measure the proton polarization in the NH_3 cell and the residual proton polarization in the ND_3 cell. A coil of three to four turns with a 1 cm diameter measured the deuteron polarization and ^{15}N polarization in the ND_3 target, while a similar one measured the ^{15}N polarization in the NH_3 cell. During the course of E143 only the proton and deuteron polarizations were measured; the ^{15}N and residual proton polarizations were checked after the experiment.

2. Polarization measurement and performance

The polarization was measured via NMR with a series-tuned Liverpool Q-meter [97]. Each spin species in the targets was measured with its own separately tuned Q-meter. Only one Q-meter could measure at a given time, taking one polarization measurement per minute. The Q of the tuned circuit is changed by the presence of the appropriate polarized nuclei, and the integral of this response is proportional to the polarization. The response function was determined by subtracting the Q-curve measured when the magnetic field was moved off resonance from the Q-curve obtained when the magnetic field was moved on resonance. The integral is normalized by comparing to the signal area at thermal equilibrium (TE) where the polarization (P_{TE}) can be calculated. For the proton, $P_{TE}=\tanh[\mu B/kT]$, where μ is the magnetic moment of the proton and k is Boltzmann's constant. Therefore, $P_{TE}=0.0034$ for $B=5$ T and $T=1.5$ K.

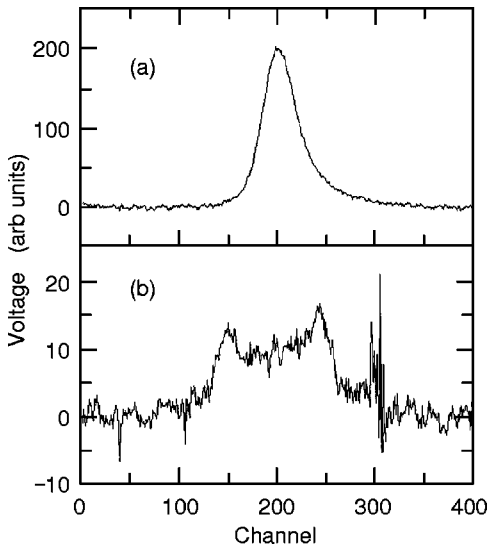

FIG. 9. Typical TE signals measured from polarized (a) protons and (b) deuterons. The spikes in the deuteron signal are an artifact of the synthesized signal generator that was used. The deuteron double-peaked line shape results from a splitting effect due to the interaction between the deuteron quadrupole moment and ammonia crystal electric field gradients. Similar lineshapes are seen in many other deuterated materials.

The TE signal for the proton is relatively easy to observe and measure, but the deuteron TE signal is about 500 times smaller than this, and thus requires advanced techniques of noise and drift suppression and signal averaging for a credible measurement [98]. Measurements were made of the proton TE signal area to a precision of about 0.2%, but repeated measurements, over a period of many weeks, showed considerable fluctuations in the mean value. Including this scatter, the overall precision of measuring the TE polarization was $\pm 2.5\%$. For the deuteron the precision of measuring the TE signal area was $\pm 3\%$ and $\pm 4\%$ overall. The fluctuation in signal area was attributed to small changes in the distribution of ammonia granules around the NMR coils. Typical TE signals for polarized protons and deuterons are shown in Fig. 9.

In our initial measurements of ^{15}N ammonia, the proton polarization performance was similar to that seen previously [99] ($>90\%$), but the deuteron only reached 13%. The maximum deuteron polarization was expected to increase with *in situ* irradiation [100]. Figure 10, which verifies this expectation, shows how the proton and deuteron polarizations performed as a function of beam dose for 5

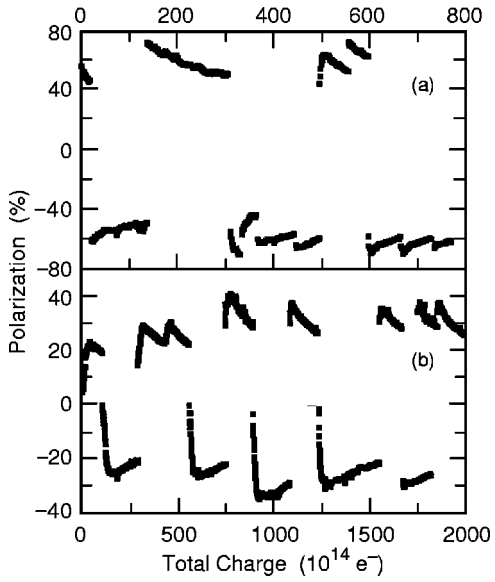

FIG. 10. The polarization history over the course of a few days is shown as a function of received charge for (a) proton and (b) deuteron targets.

$\times 10^{11}$ electrons/sec rastered over the face of a target.

The polarization decayed with beam dose as the ammonia became radiation-damaged. Once the polarization fell below a predetermined value, the other target was put into the beam until its polarization dropped to a specified level. Then both targets were annealed by warming them up to a temperature between 80 and 90 K. The sequence of polarization, irradiation and annealing affected $^{15}NH_3$ and $^{15}ND_3$ differently. For the proton, annealing brings the target back to its starting polarization, and there was no evidence of change over the period of irradiation. On the other hand, the deuteron polarization improved after each anneal, ultimately reaching a polarization of 42%. This value was obtained with frequency modulation of the microwave source. Previously, at CERN, in the Spin Muon Collaboration (SMC) experiment [101], frequency modulation had been found to improve the polarization of deuterated butanol by almost a factor of two. In deuterated ammonia the gain is more modest, with a factor of two improvement in the rate of polarization which leads to a gain in absolute polarization of 3–5%. The level of proton polarization in Fig. 10 is lower than the expected maximum of more than 90% seen in the early measurements. This was because the NH_3 target was situated below the ND_3 target which absorbed some fraction of the microwave power.

After the experiment the ^{15}N polarizations were measured as a function of both proton and deuteron polarizations. Residual proton polarizations were measured in the deuteron case. In addition, the protons in the torlon target cups became polarized once the electron beam created paramagnetic centers in that material. This led to a 3% correction of the proton polarization. The polarization values were also corrected for effects arising from inhomogeneities in target polarization due to local beam heating as discussed below.

The average polarizations for the entire experiment were 0.70 with a relative precision of 2.5% for the proton and 0.25 with a relative precision of 4% for the deuteron.

3. Beam heating corrections

As the beam passes through the polarized target, the temperature of the ammonia granules increases, and the polarization drops. By rastering the beam over the face of the target, this depolarization effect is greatly reduced. The average polarization measured by the standard NMR technique is generally not the same as what the beam sees locally. One reason for this is that ammonia granules outside the raster radius do not experience the same depolarization from beam heating as the granules inside the raster radius. The measured polarization, however, reflects a combined polarization of all the target granules. Another reason is that the polarization during the beam spill may be lower than during the time between spills when no beam heats the target. This latter effect has been studied in detail [102] and has been shown to be very small. Hence, it has been neglected in the present analysis.

If z is the relative contribution of the rastered granules to the NMR signal, then

$$P_m = zP_T + (1-z)P_i, \tag{36}$$

where P_i is the initial polarization with no incident beam, P_m is the measured polarization with incident beam, and P_T is the true polarization of the rastered granules. We define a correction to the measured polarization C_{heat} as

$$1 - C_{heat} \equiv P_T/P_m = \frac{P_m - (1-z)P_i}{zP_m}. \tag{37}$$

The parameter z depends on the geometry of the NMR coils, which is different for NH_3 and ND_3 targets, and on the direction of the target polarization (longitudinal or transverse). Values for P_i, P_m, P_T, z, and C_{heat} and the corresponding errors are given in Table II for a maximum beam intensity of 4×10^9 electrons/pulse. The errors on z include uncertainties for the target granule settling effect and for the rastering radius due to the finite size of the beam spot. For the ND_3 targets there is an additional uncertainty in the diameter of the 4 turns of the NMR coil. The corresponding corrections at other beam intensities can be extracted using the knowledge that the measured target depolarization is proportional to beam intensity.

E. Spectrometers

Two large acceptance spectrometers [103], situated at 4.5° and 7.0°, were used to detect the electrons scattered from the polarized target. The momentum acceptance of each spectrometer arm ranged from 7 to 20 GeV/c. Each spectrometer contained two dipole magnets, bending in opposite directions in the vertical plane, two gas threshold Cerenkov detectors, two scintillation hodoscope packages, each consisting of several planes, and an array of lead glass total

TABLE II. Beam heating correction results at beam intensity of 4×10^9 electrons/pulse.

Target	NH_3	NH_3	ND_3	ND_3
Polarization	Long.	Tran.	Long.	Tran.
P_i (%)	75±1.9	75±1.9	30±1.2	30±1.2
P_m (%)	68.3±1.7	68.5±1.7	24.9±1.0	24.8±1.0
z	0.924±0.029	0.903±0.033	0.912±0.023	0.931±0.021
P_T (%)	67.7±1.7	67.8±1.7	24.4±1.0	24.4±1.0
C_{heat}	0.0081±0.0036	0.0103±0.0040	0.0197±0.0064	0.0157±0.0053

absorption shower counters which were 24 radiation lengths in depth. The 4.5° spectrometer also contained a quadrupole magnet which was needed to spread the scattered electrons over a larger detector area. A schematic of the spectrometers is shown in Fig. 11.

The two-bend design was chosen to have maximum acceptance over a wide momentum range, and to shield the detectors from the considerable photon background produced by the electron beam interacting in the thick target. The Cerenkov detectors allowed discrimination against a large pion background. The hodoscopes were used to reconstruct the trajectory of each particle, which in turn could be used to determine the momentum and other kinematic variables. Finally the shower array provided the energy measurement as well as particle identification information.

The spectrometers were almost identical to those used in the E142 experiment [10]. The magnets, however, were operated at somewhat higher fields to accommodate the larger momenta of scattered electrons due to the higher beam energy. Also, the hodoscopes were modified to handle a higher instantaneous rate.

The two scintillator hodoscope arrays provided the track information of the incident particles for each spectrometer, and consisted of horizontal (y), vertical (x), and slanting (u) planes of fingers. The upstream hodoscope array contained four planes: u, x, and two y; the downstream hodoscope array contained an x, y, and u plane. The first y plane in each hodoscope array consisted of scintillator elements of 3.0 cm width, while the elements of the second y plane in the upstream hodoscopes were 4.76 cm wide. The elements in the first x plane of the 4.5° spectrometer were 2.0 cm wide, and the remaining x plane elements were 3.0 cm wide. The u planes contained elements that were 4.5 cm and 7.5 cm wide for the front and back hodoscopes respectively. Within each plane the hodoscope fingers overlapped by 1/3 of the width on both edges, resulting in a bin width of 1/3 of the element width. The moderately fine hodoscope segmentation (~210 scintillator elements per spectrometer) was chosen to tolerate the large photon and neutron backgrounds and to reconstruct with sufficient resolution the trajectory of the scattered particles. The signal from each finger was discriminated and fed into a multi-hit TDC which recorded all signals in a 100 ns window around each trigger.

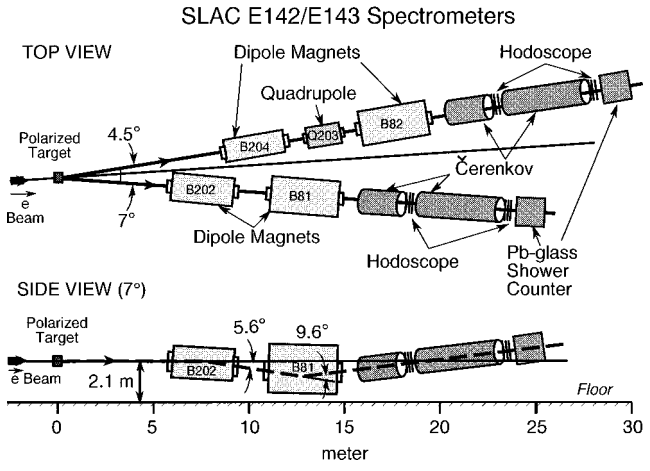

FIG. 11. A schematic of the E142/E143 spectrometer layout.

The separation of the two hodoscopes was 5.0 m in the 4.5° spectrometer arm and 5.1 m in the 7.0° arm. The scattering angle resolution at the target in the non-bend plane was 0.3 mrad for both spectrometers, whereas for the bend plane, it was ±0.9 mrad for the 4.5° arm and ±0.3 mrad for the 7.0° arm. The ideal momentum resolution was dependent on the absolute value of momentum and varied from ±0.3% to ±3.2% for the 4.5° arm and from ±0.6% to ±3.8% for the 7.0° arm.

The upstream Čerenkov counters were 2.24 m long aluminum tanks filled with nitrogen gas at a pressure of 6.3 psi for a pion threshold of 9 GeV, and the downstream counters were 4.3 m tanks containing nitrogen at 3.0 psi for a 13 GeV pion threshold. Pions below these threshold momenta did not emit Čerenkov light. The shorter tanks had inner radii of 60 cm and effective radiator lengths of 2.0 m, while the larger tanks had inner radii of 80 cm to cover the large spectrometer acceptances, and had effective radiator lengths of 4.0 m. To minimize δ-ray production and multiple scattering effects, thin tank entrance/exit windows were made from 1 mm thick aluminum.

Inside the tanks, spherical mirrors were positioned to reflect all of the emitted Čerenkov light back onto a single Hamamatsu R1584-01 five-inch photomultiplier tube coated with a p-terphenyl wavelength shifter and maintained at a base voltage of −2600 V. The mirrors had a radius of curvature of 1.63 m and 1.2 m for the large and small counters, respectively, and had reflectivity close to 90%. The large counters contained three mirrors vertically stacked and mounted on an adjustable frame for focusing purposes, and the small counters contained two mirrors mounted similarly. Signals from each photomultiplier tube were discriminated at four levels corresponding to 0.6, 1.5, 3, and 4 photoelectrons and fed into four channels of multi-hit TDC's as well as an ADC.

An electromagnetic shower calorimeter was positioned at the downstream end of each spectrometer. Each detector consisted of two hundred $6.2\times6.2\times75.0$ cm Schott type F2 lead glass blocks stacked 10 wide and 20 high in a fly's eye configuration. The glass had a radiation length of 3.17 cm and refractive index of 1.58. The incident electrons created showers via bremsstrahlung and e^+/e^- pair production in the lead glass. Electrons (and positrons) produced Čerenkov light in an amount proportional to the incident energy. The light was collected by phototubes attached to the back of the glass. To monitor the blocks, a high intensity Xe flash lamp system (Hamamatsu L2360) was installed in each calorimeter. The lamp delivered a luminous signal to each block via plastic optical fibers. The signal from one of the fibers, as well as that from a ^{241}Am source, was read out by a monitoring photomultiplier tube and sent to ADCs to detect possible Xe lamp intensity fluctuations and to monitor ADC gain changes by looking at shifts in averaged signals.

F. Trigger

The trigger consisted of a triple coincidence between discriminated signals from the two Čerenkov counters and the analogue sum of the shower counter elements. The shower discriminator threshold was set to be greater than 99% efficient for the lowest energy electrons and the Čerenkov thresholds were set to be efficient for one photoelectron signals. Up to four triggers could be generated in each beam spill. Each shower and Čerenkov counter signal was fanned out to four separate ADCs, and each trigger gated a different set of these ADCs. The detector signals to the multi-hit TDC's were filtered by a sub-trigger to reduce noise hits. Additional triggers were used to record a small fraction of the pions and to measure detector efficiencies.

G. Data acquisition

The data acquisition (DAQ) was distributed over a number of computers linked together by an ethernet-based network which implemented DECnet for communications. The distributed nature of the DAQ allowed us to build a system which could service interrupts at 120 Hz, read typically 3 KB of data for each interrupt, write data to tape at a sustained rate of nearly 300 KB/sec, control the electron beam position on target on a pulse-to-pulse basis, and analyze a substantial fraction of the event data online.

A VAX4000.200 qbus computer, referred to as real time front end (RTFE), was interrupted at 120 Hz, read data from three CAMAC branches, built an event, and then sent it via network to the data logger computer, a VAX4000.60 workstation. The RTFE ran an application which was developed with DEC's VAXeln development toolkit. The VAXeln application was able to access hardware resources more efficiently than usually possible under the DEC VMS operating system. Also, task scheduling was under programmer control. The data logger computer controlled two SCSI EXB8500 Exabyte tape drives. Event data received from the RTFE were packed into record-size buffers (approximately 32 KB in size) and written to tape. The data logger computer also distributed a sample of the event data via network to two VAX4000.60 workstations, one for online data analysis in each spectrometer. The event data were analyzed and various histograms and tables were presented for viewing in X11/Motif windows. Special purpose analyses could be performed by other VAX workstations which connected to the network. The electron beam was monitored and controlled by a microVAX II computer which, like the RTFE, was loaded with a VAXeln application specially developed for this task. A VAX cluster boot node, VAX4000.300 computer, was used to control, monitor, and log information on the spectrometer magnets and their power supplies, detector high voltage power supplies, NIM and CAMAC crate voltages, scalers, target parameters, pedestals, etc.

IV. DATA ANALYSIS

A. Event selection

Events which produced a trigger were further analyzed to identify electrons amid a background of mostly pions, and to determine the energy, momentum, and scattering angle. Raw asymmetries were then formed from the number of scattered electrons coming from each of the two states of incident electron polarization directions. These asymmetries are a function of x, Q^2, and beam energy.

Particle tracking was performed using the spatial and timing information provided by the hodoscopes and shower counter. Once a track was found, the particle's momentum and scattering angle were reconstructed. The efficiency of the hodoscope package was found to be 91% for the 4.5° spectrometer and 96% for the 7.0° spectrometer. The tracking efficiency was about 98% for the 4.5° and 99% for the 7° spectrometer. The hodoscope and tracking efficiencies were worse for the small angle spectrometer due to the higher count rate.

The shower counter was used to measure the energy deposited by the incident particle and to provide electron identification. In order to use the shower counter for energy measurements, it was necessary to calibrate each block for differences in phototube, lead glass, and ADC channel responses to the electrons. This was achieved using clean electron events which were selected using knowledge from the other detectors. In an iterative process, a set of calibration constants for the glass blocks was determined by requiring that the total energy of the cluster be equal, on average, to the momentum of the event.

Once calibrated, the shower counter was used to select electrons by comparing the energy of the particle as measured by the shower counter (E') to the momentum of the particle as measured by the hodoscope tracking system (P). Rejection of pions was achieved since typically electrons deposit all of their energy in the shower counter while pions do not. Thus, the electron events had an E'/P peak centered around unity, whereas the E'/P values for pions were in general much less than one. By making a cut around the electron peak of $0.8<E'/P<1.25$, we were able to reject the majority of pion contaminants left in our data sample. The E'/P requirement was approximately 96% efficient for electrons, and left a pion contamination of less than 1%. A sample plot of E'/P for this experiment is shown in Fig. 12.

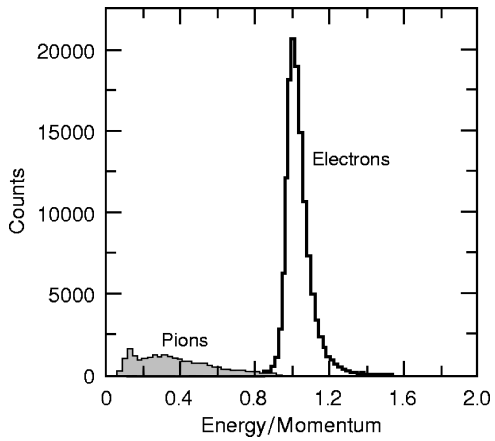

FIG. 12. Sample plot of events versus the ratio of energy to momentum as measured by the shower counter and tracking, respectively. The electron events are peaked at unity. The lower energy background pion events are removed when all cuts are applied to the data.

Electrons could also be identified over pions using the spatial profile of the shower formed by the incident particle. These profiles vary significantly depending on the type of incident particle. In particular, pion shower clusters are much smaller than electron clusters, and many of them are fully contained in one block. Electron clusters are typically contained in nine glass blocks. For electrons, the central block contained 50% to 90% of the energy and the eight neighbors contained the rest. We used a shower counter neural network algorithm [104] which modeled a typical electron cluster profile to determine which events were electron events and which were background. The neural network was approximately 98% efficient for identifying electrons and left a pion contamination of about 0.5%.

To further ensure a clean electron sample, spatial, timing, and pulse height cuts were made. A cut requiring a minimum Čerenkov ADC pulse height of 40 (more than two photoelectrons) was made yielding an efficiency of 95–99 % for the four counters. Next, we required that the track used for the momentum measurement was within 40 mm, horizontally and vertically, of the cluster from the shower counter that was used for the energy measurement. The track and the cluster were required to be within 10 ns of each other, and the track was required to point back to the target to within 13 mm to eliminate bad tracks. In addition, the few events with clusters on the outer edges of the shower counter were rejected due to the possibility of energy leakage from the sides of the counter.

B. Asymmetries and corrections

Electrons passing the event selection cuts were binned in x such that the resolution in x was slightly finer than the binning. The electrons were also tagged according to their relative target and beam helicity states, $N^{\uparrow\downarrow(\uparrow\uparrow)}$, and which spectrometer they entered. The asymmetries $A_\parallel$ and $A_\perp$ were formed:

TABLE III. Proton $A_\parallel$ and $A_\perp$ results with statistical errors for E=29.1 GeV at the measured Q^2 in $(\mathrm{GeV}/c)^2$. Also shown are the radiative corrections $A_{rc}^\parallel$ and $A_{rc}^\perp$ which were applied to the data.

x	$\langle Q^2\rangle$	$A_\parallel$	$A_{rc}^\parallel$	$A_\perp$	$A_{rc}^\perp$
		$\theta=4.5°$			
0.028	1.17	-0.026 ± 0.054	0.014	0.031 ± 0.063	0.004
0.031	1.27	0.048 ± 0.026	0.014	0.010 ± 0.032	0.004
0.035	1.40	0.091 ± 0.019	0.013	0.012 ± 0.024	0.004
0.039	1.52	0.060 ± 0.016	0.012	0.007 ± 0.020	0.004
0.044	1.65	0.076 ± 0.015	0.011	0.004 ± 0.018	0.004
0.049	1.78	0.083 ± 0.014	0.010	0.008 ± 0.017	0.004
0.056	1.92	0.082 ± 0.013	0.009	0.003 ± 0.016	0.004
0.063	2.07	0.082 ± 0.012	0.008	0.014 ± 0.015	0.004
0.071	2.22	0.086 ± 0.011	0.007	0.012 ± 0.014	0.004
0.079	2.38	0.102 ± 0.012	0.006	-0.009 ± 0.014	0.004
0.090	2.53	0.081 ± 0.012	0.005	-0.006 ± 0.014	0.004
0.101	2.69	0.114 ± 0.012	0.004	0.004 ± 0.014	0.004
0.113	2.84	0.108 ± 0.013	0.004	-0.012 ± 0.015	0.004
0.128	3.00	0.097 ± 0.013	0.003	0.010 ± 0.015	0.004
0.144	3.15	0.086 ± 0.013	0.003	-0.031 ± 0.015	0.004
0.162	3.30	0.113 ± 0.013	0.003	0.023 ± 0.016	0.004
0.182	3.45	0.110 ± 0.014	0.002	-0.021 ± 0.016	0.004
0.205	3.59	0.097 ± 0.014	0.002	0.043 ± 0.017	0.004
0.230	3.73	0.118 ± 0.015	0.002	-0.005 ± 0.018	0.004
0.259	3.85	0.107 ± 0.015	0.002	0.017 ± 0.019	0.004
0.292	3.98	0.096 ± 0.016	0.002	-0.055 ± 0.020	0.004
0.329	4.09	0.110 ± 0.018	0.002	-0.005 ± 0.022	0.004
0.370	4.20	0.080 ± 0.020	0.002	0.012 ± 0.024	0.003
0.416	4.30	0.140 ± 0.023	0.002	0.002 ± 0.028	0.003
0.468	4.40	0.140 ± 0.026	0.002	-0.048 ± 0.032	0.003
0.526	4.47	0.134 ± 0.031	0.002	-0.037 ± 0.038	0.002
0.592	4.55	0.066 ± 0.037	0.003	-0.029 ± 0.045	0.002
0.666	4.63	0.075 ± 0.045	0.000	-0.013 ± 0.055	0.002
0.749	4.70	0.128 ± 0.062	-0.007	-0.114 ± 0.074	0.004
		$\theta=7.0°$			
0.071	2.91	0.261 ± 0.095	0.018	-0.122 ± 0.102	0.006
0.079	3.17	0.159 ± 0.043	0.015	-0.002 ± 0.049	0.006
0.090	3.48	0.115 ± 0.029	0.012	0.040 ± 0.034	0.006
0.101	3.79	0.143 ± 0.024	0.010	-0.016 ± 0.027	0.006
0.113	4.11	0.158 ± 0.022	0.008	0.011 ± 0.025	0.006
0.128	4.43	0.164 ± 0.021	0.006	-0.026 ± 0.023	0.006
0.144	4.78	0.159 ± 0.020	0.005	0.007 ± 0.022	0.006
0.162	5.13	0.171 ± 0.019	0.004	0.018 ± 0.021	0.006
0.182	5.49	0.192 ± 0.019	0.003	0.052 ± 0.021	0.006
0.205	5.86	0.215 ± 0.019	0.003	0.012 ± 0.021	0.006
0.230	6.24	0.150 ± 0.019	0.002	0.007 ± 0.022	0.006
0.259	6.60	0.250 ± 0.020	0.002	0.001 ± 0.022	0.006
0.292	6.97	0.197 ± 0.021	0.002	-0.023 ± 0.023	0.005
0.329	7.34	0.195 ± 0.022	0.002	-0.012 ± 0.025	0.005
0.370	7.69	0.190 ± 0.024	0.002	-0.018 ± 0.027	0.005
0.416	8.04	0.244 ± 0.026	0.002	-0.009 ± 0.030	0.004
0.468	8.37	0.223 ± 0.030	0.002	0.005 ± 0.034	0.004
0.526	8.68	0.233 ± 0.034	0.002	-0.015 ± 0.039	0.003
0.592	8.99	0.224 ± 0.041	0.002	-0.011 ± 0.047	0.003
0.666	9.26	0.155 ± 0.051	0.002	-0.093 ± 0.063	0.002
0.749	9.53	0.223 ± 0.069	0.005	-0.097 ± 0.094	0.001

TABLE IV. Proton $A_\parallel$ results with statistical errors for E=16.2 GeV at the measured Q^2 in $(\mathrm{GeV}/c)^2$. Also shown are the radiative corrections $A_{rc}^\parallel$ which were applied to the data.

x	$\langle Q^2 \rangle$	$A_\parallel$	$A_{rc}^\parallel$
		$\theta = 4.5°$	
0.022	0.47	0.023±0.024	0.005
0.024	0.51	0.066±0.019	0.005
0.027	0.55	0.058±0.018	0.005
0.031	0.59	0.054±0.016	0.005
0.035	0.64	0.036±0.015	0.005
0.039	0.68	0.041±0.014	0.005
0.044	0.73	0.051±0.013	0.005
0.049	0.78	0.074±0.012	0.005
0.056	0.83	0.052±0.012	0.004
0.063	0.88	0.068±0.012	0.004
0.071	0.92	0.043±0.012	0.004
0.079	0.97	0.046±0.012	0.003
0.090	1.01	0.062±0.012	0.003
0.101	1.06	0.071±0.012	0.003
0.113	1.10	0.049±0.012	0.003
0.128	1.14	0.060±0.012	0.002
0.144	1.18	0.056±0.012	0.002
0.162	1.22	0.068±0.013	0.002
0.182	1.26	0.051±0.013	0.002
0.205	1.29	0.060±0.013	0.002
0.230	1.32	0.047±0.014	0.002
0.259	1.35	0.041±0.014	0.002
0.292	1.38	0.055±0.015	0.002
0.329	1.40	0.043±0.016	0.003
0.370	1.43	0.055±0.017	0.003
0.416	1.45	0.079±0.019	0.000
0.468	1.46	0.094±0.021	0.003
0.527	1.48	0.082±0.024	0.010
0.593	1.49	0.089±0.028	0.004
0.668	1.51	0.052±0.031	−0.009
0.752	1.52	0.258±0.449	−0.029
		$\theta = 7.0°$	
0.044	0.98	0.072±0.390	0.012
0.049	1.06	0.055±0.078	0.012
0.056	1.16	0.091±0.043	0.011
0.063	1.26	0.034±0.031	0.010
0.071	1.37	0.092±0.026	0.009
0.079	1.47	0.082±0.023	0.008
0.090	1.58	0.113±0.022	0.007
0.101	1.69	0.101±0.021	0.006
0.113	1.80	0.108±0.019	0.005
0.128	1.91	0.115±0.018	0.005
0.144	2.03	0.120±0.018	0.004
0.162	2.14	0.103±0.017	0.003
0.182	2.26	0.105±0.018	0.003
0.205	2.36	0.116±0.018	0.003
0.230	2.47	0.136±0.018	0.002
0.259	2.57	0.165±0.019	0.002
0.292	2.67	0.159±0.019	0.002
0.329	2.76	0.127±0.020	0.002
0.370	2.85	0.157±0.022	0.002
0.416	2.94	0.142±0.023	0.003
0.468	3.02	0.150±0.025	0.003
0.527	3.08	0.127±0.029	0.004
0.593	3.15	0.070±0.032	−0.001
0.668	3.21	0.136±0.038	0.003
0.752	3.27	−0.280±0.242	0.009

TABLE V. Proton $A_\parallel$ results with statistical errors for E=9.7 GeV at the measured Q^2 in $(\mathrm{GeV}/c)^2$. Also shown are the radiative corrections $A_{rc}^\parallel$ which were applied to the data.

x	$\langle Q^2 \rangle$	$A_\parallel$	$A_{rc}^\parallel$
		$\theta = 4.5°$	
0.028	0.28	0.021±0.046	0.003
0.031	0.30	0.021±0.022	0.002
0.035	0.31	0.048±0.019	0.002
0.039	0.33	0.011±0.017	0.002
0.044	0.35	0.046±0.016	0.001
0.049	0.36	0.043±0.016	0.001
0.056	0.38	0.040±0.015	0.001
0.063	0.40	0.026±0.015	0.001
0.071	0.41	0.030±0.015	0.001
0.080	0.43	0.032±0.015	0.001
0.090	0.44	0.018±0.014	0.000
0.101	0.45	0.024±0.014	0.000
0.113	0.47	0.041±0.013	0.000
0.128	0.48	0.002±0.013	0.000
0.144	0.49	0.002±0.013	0.000
0.162	0.50	0.018±0.013	0.000
0.182	0.51	0.024±0.013	−0.002
0.205	0.52	0.015±0.013	−0.008
0.231	0.53	0.054±0.014	−0.004
0.259	0.53	0.047±0.014	0.015
0.292	0.54	0.051±0.016	0.014
0.329	0.55	0.020±0.018	0.001
0.370	0.55	−0.002±0.019	−0.007
0.417	0.56	−0.004±0.021	−0.015
0.469	0.56	−0.034±0.021	−0.020
0.527	0.57	0.007±0.029	−0.034
0.594	0.57	−0.013±0.064	−0.043
0.669	0.57	0.010±0.179	−0.039
0.753	0.58	0.021±0.214	−0.036
0.847	0.58	0.031±0.257	−0.032
		$\theta = 7.0°$	
0.063	0.60	−0.013±0.093	0.003
0.071	0.64	0.031±0.038	0.003
0.080	0.69	0.076±0.025	0.003
0.090	0.74	0.064±0.019	0.003
0.101	0.78	0.057±0.016	0.003
0.113	0.82	0.073±0.015	0.003
0.128	0.86	0.048±0.015	0.003
0.144	0.90	0.047±0.014	0.002
0.162	0.93	0.065±0.013	0.002
0.182	0.97	0.087±0.013	0.002
0.205	1.00	0.068±0.013	0.002
0.231	1.03	0.084±0.013	0.002
0.259	1.06	0.070±0.013	0.003
0.292	1.09	0.055±0.013	0.004
0.329	1.12	0.088±0.014	0.005
0.370	1.14	0.088±0.014	−0.004
0.417	1.16	0.082±0.016	0.001
0.469	1.18	0.084±0.016	0.018
0.527	1.21	0.086±0.018	0.010
0.594	1.22	−0.001±0.018	−0.004
0.669	1.23	0.022±0.018	−0.026
0.753	1.25	−0.044±0.047	−0.061
0.847	1.26	−0.018±0.149	−0.064

TABLE VI. Deuteron $A_\parallel$ and $A_\perp$ results with statistical errors for $E=29.1$ GeV at the measured Q^2 in $(\mathrm{GeV}/c)^2$. Also shown are the radiative corrections $A_{rc}^\parallel$ and $A_{rc}^\perp$ which were applied to the data.

x	$\langle Q^2\rangle$	$A_\parallel$	$A_{rc}^\parallel$	$A_\perp$	$A_{rc}^\perp$
		$\theta=4.5°$			
0.028	1.17	-0.042 ± 0.075	-0.004	-0.138 ± 0.175	0.002
0.031	1.27	0.035 ± 0.030	-0.004	-0.114 ± 0.146	0.002
0.035	1.40	0.004 ± 0.021	-0.004	0.060 ± 0.083	0.002
0.039	1.52	0.043 ± 0.019	-0.004	0.038 ± 0.046	0.002
0.044	1.65	-0.011 ± 0.017	-0.004	0.050 ± 0.038	0.002
0.049	1.78	-0.009 ± 0.016	-0.004	0.022 ± 0.034	0.002
0.056	1.92	0.012 ± 0.015	-0.003	-0.043 ± 0.031	0.002
0.063	2.07	0.010 ± 0.014	-0.003	-0.040 ± 0.029	0.002
0.071	2.22	0.014 ± 0.013	-0.003	0.009 ± 0.028	0.002
0.079	2.38	0.023 ± 0.013	-0.003	-0.009 ± 0.029	0.002
0.090	2.53	0.038 ± 0.014	-0.003	0.032 ± 0.029	0.002
0.101	2.69	0.028 ± 0.014	-0.003	-0.031 ± 0.030	0.002
0.113	2.84	0.037 ± 0.015	-0.002	0.012 ± 0.031	0.002
0.128	3.00	0.079 ± 0.015	-0.002	-0.001 ± 0.032	0.002
0.144	3.15	0.053 ± 0.016	-0.002	-0.023 ± 0.033	0.002
0.162	3.30	0.046 ± 0.016	-0.001	0.043 ± 0.035	0.002
0.182	3.45	0.054 ± 0.017	-0.001	-0.042 ± 0.036	0.002
0.205	3.59	0.049 ± 0.017	0.000	-0.013 ± 0.038	0.002
0.230	3.73	0.020 ± 0.019	0.000	0.008 ± 0.040	0.002
0.259	3.85	0.021 ± 0.020	0.000	0.095 ± 0.043	0.002
0.292	3.98	0.054 ± 0.021	0.001	-0.016 ± 0.047	0.002
0.329	4.09	0.078 ± 0.023	0.001	-0.025 ± 0.052	0.002
0.370	4.20	0.072 ± 0.026	0.001	-0.026 ± 0.059	0.002
0.416	4.30	0.063 ± 0.030	0.001	-0.050 ± 0.068	0.001
0.468	4.40	0.010 ± 0.036	0.001	-0.071 ± 0.081	0.001
0.526	4.47	0.065 ± 0.043	0.001	0.077 ± 0.098	0.001
0.592	4.55	0.057 ± 0.052	0.001	-0.116 ± 0.120	0.001
0.666	4.62	0.023 ± 0.066	-0.002	0.160 ± 0.150	0.002
0.749	4.70	-0.190 ± 0.091	-0.006	0.150 ± 0.203	0.004
		$\theta=7.0°$			
0.071	2.91	0.044 ± 0.108	-0.004	0.088 ± 0.237	0.003
0.079	3.17	-0.020 ± 0.049	-0.004	0.081 ± 0.094	0.003
0.090	3.48	0.044 ± 0.033	-0.004	-0.024 ± 0.062	0.003
0.101	3.79	0.044 ± 0.027	-0.004	0.075 ± 0.050	0.003
0.113	4.11	0.023 ± 0.025	-0.004	-0.036 ± 0.046	0.003
0.128	4.44	0.053 ± 0.023	-0.003	-0.014 ± 0.043	0.003
0.144	4.78	0.110 ± 0.023	-0.003	-0.038 ± 0.041	0.003
0.162	5.13	0.051 ± 0.022	-0.003	-0.027 ± 0.041	0.003
0.182	5.49	0.133 ± 0.022	-0.002	0.035 ± 0.040	0.003
0.205	5.86	0.067 ± 0.022	-0.002	-0.085 ± 0.041	0.003
0.230	6.23	0.088 ± 0.023	-0.001	-0.056 ± 0.043	0.003
0.259	6.60	0.051 ± 0.024	0.000	0.065 ± 0.045	0.003
0.292	6.97	0.102 ± 0.026	0.000	-0.028 ± 0.048	0.003
0.329	7.33	0.108 ± 0.028	0.001	-0.034 ± 0.052	0.002
0.370	7.69	0.143 ± 0.030	0.001	-0.024 ± 0.057	0.002
0.416	8.03	0.089 ± 0.034	0.001	-0.018 ± 0.064	0.002
0.468	8.37	0.125 ± 0.039	0.000	-0.003 ± 0.073	0.002
0.526	8.67	0.172 ± 0.046	0.000	-0.023 ± 0.086	0.002
0.592	8.98	0.094 ± 0.056	-0.001	0.235 ± 0.108	0.002
0.666	9.26	0.086 ± 0.070	-0.001	-0.125 ± 0.147	0.002
0.749	9.52	0.193 ± 0.096	0.000	-0.068 ± 0.212	0.002

TABLE VII. Deuteron $A_\parallel$ results with statistical errors for E=16.2 GeV at the measured Q^2 in $(\mathrm{GeV}/c)^2$. Also shown are the radiative corrections $A_{rc}^\parallel$ which were applied to the data.

x	$\langle Q^2\rangle$	$A_\parallel$	$A_{rc}^\parallel$
		$\theta=4.5°$	
0.022	0.47	-0.018 ± 0.064	-0.006
0.024	0.51	-0.035 ± 0.049	-0.006
0.027	0.55	-0.012 ± 0.045	-0.005
0.031	0.59	0.012 ± 0.041	-0.005
0.035	0.64	-0.009 ± 0.038	-0.004
0.039	0.68	0.056 ± 0.034	-0.004
0.044	0.73	-0.021 ± 0.028	-0.004
0.049	0.78	0.046 ± 0.026	-0.003
0.056	0.83	0.003 ± 0.025	-0.003
0.063	0.87	0.021 ± 0.025	-0.003
0.071	0.92	0.026 ± 0.025	-0.003
0.079	0.97	-0.016 ± 0.025	-0.002
0.090	1.01	0.038 ± 0.025	-0.002
0.101	1.06	0.019 ± 0.025	-0.002
0.113	1.10	0.016 ± 0.025	-0.001
0.128	1.14	0.063 ± 0.025	-0.001
0.144	1.18	0.050 ± 0.025	-0.001
0.162	1.22	-0.025 ± 0.025	-0.001
0.182	1.25	0.043 ± 0.026	0.000
0.205	1.29	0.042 ± 0.027	0.000
0.230	1.32	0.016 ± 0.027	0.000
0.259	1.35	0.022 ± 0.029	0.001
0.292	1.37	0.062 ± 0.031	0.001
0.329	1.40	0.023 ± 0.033	0.001
0.370	1.42	-0.031 ± 0.036	0.001
0.416	1.44	0.013 ± 0.040	-0.001
0.468	1.46	0.089 ± 0.045	0.001
0.527	1.48	0.014 ± 0.053	0.003
0.593	1.49	0.071 ± 0.063	-0.002
0.668	1.50	0.037 ± 0.076	-0.013
		$\theta=7.0°$	
0.049	1.06	-0.075 ± 0.201	-0.005
0.056	1.16	0.062 ± 0.106	-0.005
0.063	1.26	-0.003 ± 0.075	-0.004
0.071	1.36	0.054 ± 0.060	-0.004
0.079	1.47	-0.073 ± 0.054	-0.004
0.090	1.58	0.121 ± 0.049	-0.004
0.101	1.69	0.054 ± 0.046	-0.003
0.113	1.80	0.027 ± 0.041	-0.003
0.128	1.91	0.018 ± 0.038	-0.002
0.144	2.03	0.039 ± 0.036	-0.002
0.162	2.14	0.060 ± 0.036	-0.002
0.182	2.25	0.097 ± 0.036	-0.001
0.205	2.36	0.045 ± 0.036	-0.001
0.230	2.47	0.041 ± 0.038	0.000
0.259	2.57	0.041 ± 0.039	0.000
0.292	2.67	0.115 ± 0.040	0.001
0.329	2.76	0.160 ± 0.042	0.001
0.370	2.85	0.039 ± 0.045	0.001
0.416	2.93	0.055 ± 0.049	0.001
0.468	3.01	0.168 ± 0.054	0.001
0.527	3.08	0.139 ± 0.062	0.001
0.593	3.15	0.055 ± 0.073	-0.002
0.668	3.21	-0.013 ± 0.088	-0.001

TABLE VIII. Deuteron $A_\parallel$ results with statistical errors for E=9.7 GeV at the measured Q^2 in $(\mathrm{GeV}/c)^2$. Also shown are the radiative corrections $A_{rc}^{\parallel}$ which were applied to the data.

x	$\langle Q^2 \rangle$	$A_\parallel$	$A_{rc}^{\parallel}$
		$\theta = 4.5°$	
0.028	0.28	0.053±0.069	−0.005
0.031	0.30	−0.067±0.034	−0.005
0.035	0.31	−0.014±0.028	−0.004
0.039	0.33	0.017±0.025	−0.004
0.044	0.35	0.001±0.024	−0.004
0.050	0.36	0.022±0.023	−0.004
0.056	0.38	−0.017±0.022	−0.003
0.063	0.40	−0.002±0.021	−0.003
0.071	0.41	0.032±0.022	−0.003
0.080	0.43	−0.004±0.022	−0.003
0.090	0.44	0.008±0.021	−0.002
0.101	0.45	0.038±0.020	−0.002
0.113	0.47	−0.002±0.019	−0.002
0.128	0.48	−0.017±0.019	−0.002
0.144	0.49	−0.004±0.019	−0.002
0.162	0.50	0.015±0.019	−0.002
0.182	0.51	0.028±0.019	−0.002
0.205	0.52	0.012±0.020	−0.005
0.231	0.53	0.016±0.021	−0.003
0.259	0.53	0.009±0.022	0.005
0.292	0.54	0.028±0.024	0.005
0.329	0.55	0.031±0.026	−0.004
0.370	0.55	−0.032±0.027	−0.009
0.417	0.56	0.029±0.030	−0.014
0.469	0.56	−0.039±0.032	−0.019
0.527	0.57	−0.005±0.045	−0.029
0.594	0.57	−0.008±0.074	−0.036
0.669	0.57	−0.021±0.110	−0.039
0.753	0.58	0.001±0.117	−0.042
0.847	0.58	0.010±0.142	−0.046
		$\theta = 7.0°$	
0.063	0.60	0.116±0.133	−0.005
0.071	0.64	−0.036±0.054	−0.005
0.080	0.69	0.013±0.037	−0.004
0.090	0.74	−0.013±0.028	−0.003
0.101	0.78	0.016±0.024	−0.003
0.113	0.82	0.024±0.022	−0.003
0.128	0.86	0.052±0.021	−0.002
0.144	0.90	0.012±0.020	−0.002
0.162	0.93	0.036±0.020	−0.001
0.182	0.97	0.027±0.019	−0.001
0.205	1.00	0.005±0.019	0.000
0.231	1.03	0.044±0.019	0.000
0.259	1.06	0.019±0.020	0.001
0.292	1.09	0.021±0.020	0.002
0.329	1.12	0.034±0.021	0.002
0.370	1.14	0.036±0.022	−0.003
0.417	1.16	0.068±0.023	−0.001
0.469	1.19	0.020±0.025	0.007
0.527	1.21	0.024±0.029	0.001
0.594	1.22	0.022±0.033	−0.011
0.669	1.24	0.028±0.039	−0.029
0.753	1.25	0.000±0.068	−0.054
0.847	1.26	−0.018±0.118	−0.066

$$A_\parallel (\text{or } A_\perp) = C_1 \left(\frac{1}{f P_b P_t} \frac{N_L - N_R}{N_L + N_R} - C_2 \right) + A_{rc}. \quad (38)$$

Here f is the dilution factor, P_b and P_t are the beam and target polarizations, A_{rc} is the radiative correction to the asymmetry, and $C_{1(2)}$ are the corrections needed due to the presence of nitrogen in the targets, with C_2 disappearing for the proton target. These corrections are discussed in more detail below. Here $N_{L(R)}$ is the number of left or right-handed helicity events corrected as

$$N_{L(R)} = N_{L(R)}^{(raw)} \frac{d_{L(R)}}{Q_{L(R)}} \quad (39)$$

where $d_{L(R)}$ is the appropriate dead time correction and $Q_{L(R)}$ is the appropriate incident charge.

1. Polarized nitrogen and residual proton corrections

In measuring the proton and the deuteron asymmetries, it was necessary to correct for events which scattered from other polarizable nuclei in the target aside from the desired protons or deuterons [105]. The targets were made of $^{15}NH_3$ and $^{15}ND_3$, and both the ^{15}N and the $\approx 2\%$ contamination of ^{14}N were polarizable. In addition, the $^{15}ND_3$ target contained $\approx 1.5\%$ of unsubstituted or residual polarizable protons from $^{15}NH_3$.

The polarization of ^{15}N and the residual protons was measured after the experiment. The unpaired proton in ^{15}N contributes to the measured proton asymmetry proportionally to the nitrogen polarization and with a negative sign because of the negative magnetic moment of ^{15}N. For the target material $^{15}NH_3$, the following fit was used to express the ^{15}N polarization P_N in terms of the polarization of the protons P_p:

$$P_N = 0.136 P_p - 0.183 P_p^2 + 0.335 P_p^3 \approx 0.12. \quad (40)$$

The correction C_1^p to the proton asymmetry ($C_2^p = 0$) which is referred to in Eq. (38) is given by

$$C_1^p = 1 - \frac{1}{3} \frac{1}{3} \frac{P_N}{P_p} g_{\mathrm{EMC}}(x) \approx 0.98. \quad (41)$$

Here $g_{\mathrm{EMC}}(x)$ is the correction for the European Muon Collaboration (EMC) effect [106] taken at atomic mass number 15. The first factor $-\frac{1}{3}$ comes from Clebsch-Gordan coefficients involving the nitrogen wave function. The second factor $\frac{1}{3}$ reflects the fact that ammonia has three hydrogen atoms for each nitrogen atom. The error on the second term in C_1^p was estimated to be about 20% relative which yields a systematic error of 0.004 on C_1^p. Here the contribution of ^{14}N to the asymmetry was neglected.

For the target material $^{15}ND_3$, the corrections were more complicated because they account for both the residual protons and the unpaired proton in the ^{15}N. For each case, the correction involved the measured proton asymmetry.

The ^{15}N polarization P_N is given by

$$P_N = -0.40 P_d, \quad (42)$$

TABLE IX. Results for g_1/F_1 in the DIS region ($W^2 \geq 4$ GeV^2). There is an additional normalization uncertainty due to beam and target polarization shown in Table XV.

x	$\langle Q^2 \rangle$	E(GeV)	$g_1^p/F_1^p \pm \text{stat} \pm \text{syst}$	$g_1^d/F_1^d \pm \text{stat} \pm \text{syst}$	$g_1^n/F_1^n \pm \text{stat} \pm \text{syst}$
0.024	0.51	16.2	0.092±0.027±0.014	−0.048±0.068±0.009	−0.205±0.153±0.023
0.027	0.55	16.2	0.086±0.026±0.013	−0.018±0.065±0.009	−0.131±0.146±0.022
0.027	1.17	29.1	−0.032±0.068±0.010	−0.058±0.092±0.009	−0.099±0.225±0.020
0.031	0.59	16.2	0.084±0.026±0.012	0.019±0.065±0.008	−0.048±0.144±0.020
0.031	1.27	29.1	0.064±0.034±0.009	0.041±0.040±0.008	0.021±0.095±0.019
0.035	0.31	9.7	0.096±0.037±0.018	−0.027±0.055±0.008	−0.161±0.125±0.024
0.035	0.64	16.2	0.059±0.024±0.011	−0.015±0.062±0.007	−0.097±0.139±0.018
0.035	1.40	29.1	0.123±0.025±0.008	0.008±0.029±0.007	−0.115±0.069±0.017
0.039	0.33	9.7	0.024±0.037±0.018	0.035±0.053±0.008	0.050±0.122±0.024
0.039	0.68	16.2	0.072±0.024±0.011	0.099±0.060±0.007	0.140±0.136±0.017
0.039	1.52	29.1	0.083±0.023±0.008	0.062±0.026±0.007	0.049±0.063±0.016
0.044	0.35	9.7	0.106±0.037±0.019	0.003±0.054±0.008	−0.109±0.126±0.024
0.044	0.73	16.2	0.096±0.023±0.011	−0.038±0.052±0.006	−0.191±0.120±0.017
0.044	0.98	16.2	0.097±0.520±0.010	−0.943±1.296±0.008	−2.222±2.964±0.019
0.044	1.65	29.1	0.110±0.021±0.008	−0.013±0.025±0.006	−0.150±0.060±0.014
0.049	0.36	9.7	0.108±0.039±0.020	0.055±0.057±0.008	0.003±0.134±0.025
0.049	0.78	16.2	0.147±0.024±0.011	0.092±0.052±0.006	0.045±0.121±0.016
0.049	1.06	16.2	0.078±0.109±0.010	−0.104±0.280±0.008	−0.321±0.646±0.018
0.049	1.78	29.1	0.125±0.020±0.008	−0.013±0.024±0.005	−0.168±0.058±0.013
0.056	0.38	9.7	0.108±0.041±0.021	−0.045±0.059±0.008	−0.221±0.141±0.027
0.056	0.57	9.7	−0.214±1.891±0.014	2.992±2.465±0.007	7.028±5.977±0.020
0.056	0.83	16.2	0.110±0.025±0.011	0.007±0.054±0.006	−0.106±0.127±0.016
0.056	1.16	16.2	0.132±0.063±0.010	0.091±0.153±0.007	0.060±0.357±0.017
0.056	1.92	29.1	0.130±0.020±0.008	0.016±0.023±0.005	−0.109±0.058±0.012
0.063	0.40	9.7	0.078±0.043±0.022	−0.006±0.062±0.009	−0.101±0.149±0.029
0.063	0.60	9.7	−0.024±0.177±0.014	0.221±0.252±0.007	0.531±0.609±0.019
0.063	0.87	16.2	0.157±0.027±0.012	0.049±0.057±0.005	−0.064±0.135±0.016
0.063	1.26	16.2	0.052±0.046±0.009	−0.004±0.112±0.006	−0.068±0.262±0.015
0.063	2.07	29.1	0.138±0.020±0.008	0.014±0.023±0.004	−0.123±0.057±0.011
0.063	2.69	29.1	1.138±0.833±0.009	−0.446±2.060±0.006	−2.318±4.857±0.016
0.071	0.41	9.7	0.096±0.049±0.023	0.104±0.070±0.011	0.129±0.171±0.032
0.071	0.64	9.7	0.064±0.077±0.014	−0.072±0.109±0.006	−0.240±0.267±0.019
0.071	0.92	16.2	0.107±0.029±0.012	0.064±0.061±0.005	0.026±0.145±0.016
0.071	1.36	16.2	0.144±0.041±0.009	0.085±0.095±0.005	0.033±0.225±0.014
0.071	2.22	29.1	0.150±0.020±0.008	0.025±0.023±0.004	−0.114±0.059±0.011
0.071	2.91	29.1	0.324±0.121±0.010	0.063±0.139±0.006	−0.223±0.353±0.015
0.079	0.43	9.7	0.113±0.053±0.025	−0.014±0.075±0.014	−0.161±0.185±0.038
0.079	0.69	9.7	0.164±0.053±0.014	0.029±0.078±0.006	−0.121±0.194±0.019
0.079	0.97	16.2	0.122±0.031±0.013	−0.043±0.066±0.005	−0.242±0.159±0.016
0.079	1.47	16.2	0.135±0.039±0.009	−0.119±0.088±0.005	−0.436±0.212±0.013
0.079	2.38	29.1	0.188±0.021±0.009	0.041±0.025±0.004	−0.121±0.063±0.012
0.079	3.17	29.1	0.209±0.057±0.010	−0.020±0.065±0.005	−0.289±0.167±0.014
0.090	0.44	9.7	0.069±0.055±0.027	0.031±0.078±0.018	−0.008±0.193±0.045
0.090	0.74	9.7	0.145±0.043±0.014	−0.028±0.062±0.007	−0.236±0.156±0.019
0.090	1.01	16.2	0.178±0.034±0.013	0.110±0.071±0.006	0.054±0.173±0.017
0.090	1.58	16.2	0.196±0.037±0.009	0.209±0.085±0.004	0.268±0.207±0.013
0.090	2.53	29.1	0.159±0.023±0.010	0.077±0.027±0.004	−0.003±0.070±0.013
0.090	3.48	29.1	0.157±0.040±0.010	0.057±0.045±0.004	−0.049±0.117±0.013
0.101	0.45	9.7	0.102±0.057±0.030	0.158±0.081±0.023	0.252±0.203±0.054
0.101	0.78	9.7	0.138±0.040±0.014	0.039±0.058±0.007	−0.070±0.147±0.021
0.101	1.06	16.2	0.221±0.037±0.012	0.058±0.077±0.006	−0.121±0.189±0.017
0.101	1.69	16.2	0.184±0.037±0.009	0.098±0.083±0.004	0.016±0.205±0.012

TABLE IX. *(Continued).*

x	$\langle Q^2 \rangle$	E(GeV)	$g_1^p/F_1^p \pm \text{stat} \pm \text{syst}$	$g_1^d/F_1^d \pm \text{stat} \pm \text{syst}$	$g_1^n/F_1^n \pm \text{stat} \pm \text{syst}$
0.101	2.69	29.1	0.237±0.025±0.010	0.056±0.030±0.004	−0.148±0.078±0.013
0.101	3.79	29.1	0.196±0.033±0.010	0.067±0.038±0.004	−0.075±0.099±0.013
0.113	0.47	9.7	0.185±0.059±0.033	−0.008±0.086±0.027	−0.237±0.215±0.064
0.113	0.82	9.7	0.191±0.040±0.015	0.063±0.057±0.009	−0.076±0.147±0.023
0.113	1.10	16.2	0.168±0.041±0.012	0.054±0.083±0.007	−0.071±0.208±0.018
0.113	1.80	16.2	0.208±0.037±0.009	0.052±0.078±0.004	−0.126±0.196±0.012
0.113	2.84	29.1	0.239±0.028±0.012	0.082±0.033±0.005	−0.090±0.087±0.015
0.113	4.11	29.1	0.225±0.031±0.010	0.029±0.036±0.004	−0.203±0.094±0.013
0.128	0.48	9.7	0.011±0.064±0.036	−0.082±0.092±0.031	−0.209±0.233±0.072
0.128	0.86	9.7	0.135±0.041±0.015	0.146±0.059±0.010	0.191±0.152±0.026
0.128	1.14	16.2	0.221±0.045±0.013	0.230±0.090±0.008	0.293±0.227±0.020
0.128	1.91	16.2	0.234±0.037±0.010	0.037±0.077±0.005	−0.197±0.194±0.013
0.128	3.00	29.1	0.230±0.030±0.013	0.186±0.036±0.005	0.171±0.096±0.017
0.128	4.44	29.1	0.237±0.030±0.010	0.077±0.035±0.004	−0.106±0.093±0.013
0.144	0.90	9.7	0.141±0.042±0.016	0.036±0.060±0.012	−0.087±0.158±0.029
0.144	1.18	16.2	0.222±0.049±0.013	0.200±0.099±0.009	0.217±0.251±0.022
0.144	2.03	16.2	0.259±0.038±0.011	0.085±0.078±0.005	−0.114±0.198±0.015
0.144	3.15	29.1	0.213±0.033±0.014	0.132±0.039±0.006	0.057±0.106±0.018
0.144	4.78	29.1	0.242±0.030±0.010	0.163±0.034±0.004	0.097±0.093±0.013
0.162	0.93	9.7	0.212±0.043±0.017	0.117±0.063±0.014	0.024±0.166±0.032
0.162	1.22	16.2	0.293±0.054±0.013	−0.107±0.108±0.011	−0.639±0.279±0.025
0.162	2.14	16.2	0.237±0.040±0.012	0.137±0.082±0.007	0.039±0.211±0.018
0.162	3.30	29.1	0.306±0.036±0.014	0.128±0.044±0.007	−0.075±0.119±0.020
0.162	5.13	29.1	0.272±0.030±0.010	0.078±0.035±0.005	−0.159±0.096±0.014
0.182	0.97	9.7	0.303±0.045±0.018	0.095±0.067±0.015	−0.151±0.178±0.035
0.182	1.25	16.2	0.239±0.060±0.014	0.201±0.121±0.012	0.196±0.315±0.028
0.182	2.25	16.2	0.257±0.043±0.014	0.236±0.087±0.008	0.261±0.227±0.021
0.182	3.45	29.1	0.313±0.040±0.014	0.152±0.048±0.008	−0.030±0.134±0.021
0.182	5.49	29.1	0.320±0.031±0.011	0.222±0.036±0.006	0.136±0.101±0.016
0.205	1.00	9.7	0.253±0.048±0.017	0.017±0.071±0.016	−0.291±0.192±0.036
0.205	1.29	16.2	0.304±0.066±0.015	0.211±0.135±0.014	0.135±0.355±0.031
0.205	2.36	16.2	0.301±0.046±0.015	0.116±0.094±0.009	−0.110±0.250±0.023
0.205	3.59	29.1	0.303±0.044±0.015	0.150±0.054±0.009	−0.026±0.151±0.023
0.205	5.86	29.1	0.371±0.032±0.012	0.107±0.038±0.007	−0.235±0.108±0.018
0.230	1.03	9.7	0.332±0.050±0.018	0.175±0.075±0.017	0.001±0.205±0.039
0.230	1.32	16.2	0.255±0.073±0.017	0.086±0.150±0.015	−0.126±0.401±0.034
0.230	2.47	16.2	0.376±0.050±0.015	0.112±0.104±0.010	−0.230±0.281±0.026
0.230	3.73	29.1	0.389±0.049±0.015	0.066±0.062±0.010	−0.374±0.176±0.025
0.230	6.23	29.1	0.273±0.035±0.012	0.153±0.042±0.009	0.014±0.120±0.021
0.259	1.35	16.2	0.236±0.082±0.018	0.130±0.169±0.015	0.011±0.459±0.036
0.259	2.57	16.2	0.485±0.055±0.016	0.121±0.114±0.012	−0.378±0.315±0.028
0.259	3.85	29.1	0.384±0.055±0.016	0.089±0.071±0.011	−0.321±0.205±0.027
0.259	6.60	29.1	0.477±0.038±0.014	0.105±0.046±0.010	−0.422±0.137±0.024
0.292	1.37	16.2	0.340±0.091±0.020	0.385±0.192±0.015	0.538±0.530±0.036
0.292	2.67	16.2	0.498±0.061±0.017	0.359±0.126±0.013	0.232±0.355±0.031
0.292	3.98	29.1	0.361±0.063±0.017	0.205±0.082±0.013	0.014±0.243±0.031
0.292	6.97	29.1	0.395±0.043±0.015	0.202±0.053±0.012	−0.051±0.158±0.028
0.329	2.76	16.2	0.419±0.068±0.021	0.533±0.142±0.017	0.830±0.409±0.040
0.329	4.09	29.1	0.456±0.075±0.018	0.317±0.097±0.014	0.168±0.297±0.034
0.329	7.33	29.1	0.418±0.048±0.020	0.227±0.060±0.013	−0.031±0.186±0.033
0.370	2.85	16.2	0.553±0.077±0.023	0.135±0.161±0.014	−0.511±0.477±0.037
0.370	4.20	29.1	0.362±0.089±0.020	0.319±0.118±0.016	0.321±0.371±0.037

TABLE IX. *(Continued).*

x	$\langle Q^2 \rangle$	E(GeV)	$g_1^p/F_1^p \pm \text{stat} \pm \text{syst}$	$g_1^d/F_1^d \pm \text{stat} \pm \text{syst}$	$g_1^n/F_1^n \pm \text{stat} \pm \text{syst}$
0.370	7.69	29.1	$0.432 \pm 0.055 \pm 0.022$	$0.325 \pm 0.070 \pm 0.015$	$0.217 \pm 0.225 \pm 0.038$
0.416	2.93	16.2	$0.529 \pm 0.087 \pm 0.020$	$0.204 \pm 0.186 \pm 0.014$	$-0.297 \pm 0.569 \pm 0.035$
0.416	4.30	29.1	$0.676 \pm 0.108 \pm 0.021$	$0.295 \pm 0.145 \pm 0.017$	$-0.298 \pm 0.474 \pm 0.039$
0.416	8.03	29.1	$0.597 \pm 0.065 \pm 0.021$	$0.216 \pm 0.083 \pm 0.017$	$-0.413 \pm 0.278 \pm 0.040$
0.468	3.01	16.2	$0.590 \pm 0.101 \pm 0.027$	$0.669 \pm 0.216 \pm 0.013$	$0.990 \pm 0.689 \pm 0.038$
0.468	4.40	29.1	$0.713 \pm 0.136 \pm 0.022$	$0.037 \pm 0.185 \pm 0.017$	$-1.205 \pm 0.628 \pm 0.040$
0.468	8.37	29.1	$0.584 \pm 0.078 \pm 0.023$	$0.328 \pm 0.102 \pm 0.019$	$-0.077 \pm 0.356 \pm 0.044$
0.526	4.47	29.1	$0.731 \pm 0.169 \pm 0.022$	$0.375 \pm 0.237 \pm 0.015$	$-0.224 \pm 0.838 \pm 0.038$
0.526	8.67	29.1	$0.652 \pm 0.096 \pm 0.024$	$0.478 \pm 0.129 \pm 0.020$	$0.257 \pm 0.471 \pm 0.047$
0.592	4.55	29.1	$0.382 \pm 0.217 \pm 0.021$	$0.310 \pm 0.310 \pm 0.012$	$0.243 \pm 1.129 \pm 0.032$
0.592	8.98	29.1	$0.670 \pm 0.123 \pm 0.025$	$0.325 \pm 0.168 \pm 0.021$	$-0.331 \pm 0.640 \pm 0.048$
0.666	9.26	29.1	$0.478 \pm 0.165 \pm 0.026$	$0.251 \pm 0.226 \pm 0.019$	$-0.192 \pm 0.876 \pm 0.046$
0.749	9.52	29.1	$0.744 \pm 0.237 \pm 0.031$	$0.646 \pm 0.331 \pm 0.033$	$0.569 \pm 1.233 \pm 0.073$

where P_d is the polarization of the deuterons. The residual proton polarization is expressed as

$$P_p^{res} = 0.191 + 0.683 P_d \quad \text{for} \quad P_d > 0.16$$
$$= 1.875 P_d \quad \text{for} \quad P_d \leqslant 0.16. \tag{43}$$

The polarization of ^{14}N was obtained from the measured ^{15}N polarization by assuming that the polarization was equal and opposite in sign to that of ^{15}N. The corrections used in Eq. (38) for the $^{15}ND_3$ target are given by:

$$C_1^d = \frac{1}{1 - \eta_p + D_n/(1 - 1.5\omega_D)} \approx 1.02,$$

$$C_2^d = \frac{U_p F_2^p}{U_d F_2^d}(D_n - D_p)(A^p - A_{rc})$$
$$\approx -0.03(A^p - A_{rc}). \tag{44}$$

A^p is the final proton (Born) asymmetry $A_\parallel$ or $A_\perp$, and by subtracting the appropriate proton radiative correction A_{rc} we are left with the radiated asymmetry. U_p and U_d are the radiative corrections to the unpolarized cross-sections. The remaining factors are defined as

$$\eta_p = \frac{\text{number of protons}}{\text{number of deuterons} + \text{number of protons}} \approx 0.015,$$

$$D_n = \eta_N \frac{P_N}{P_d} \frac{g_{\text{EMC}}(x)}{9},$$

$$D_p = \eta_p \frac{P_p^{res}}{P_d} + (2\eta_N - 1) \frac{P_N}{P_d} \frac{g_{\text{EMC}}(x)}{9}, \tag{45}$$

$$\eta_N = \frac{\text{number of } ^{14}\text{N}}{\text{number of } ^{14}\text{N} + \text{number of } ^{15}\text{N}} \approx 0.02.$$

The error on C_1^d was neglected since this value was very small and stable. The factor C_2^d contains the proton asymmetry and was calculated for each x-bin using the measured proton asymmetry and its error.

2. Background subtraction of positrons and pions

The data collected in each of the spectrometers included background events coming from a small number of misidentified pions and from electrons produced in pair-symmetric processes (mostly $\pi^0 \to 2\gamma$, $\gamma \to e^- + e^+$). This background (mostly pair-symmetric) was responsible for up to 10% of the events in the lowest x-bin, but close to zero events for $x > 0.3$. To measure the background, data were taken with the spectrometer magnets' polarity flipped to measure π^+ and e^+. The same cuts were applied to eliminate the majority of pions as in the electron runs. A positive particle asymmetry A_+ was formed and was corrected just as in the case of the electron asymmetry A_- for varying experimental conditions such as beam and target polarizations. This positive particle asymmetry was found to be consistent with zero. The background-corrected electron asymmetry was determined by

$$A = A_- \frac{N_-}{N_- - N_+} - A_+ \frac{N_+}{N_- - N_+}, \tag{46}$$

where N_-, N_+ are the number of events per incoming charge for electron and positron runs. The misidentified pion background was subtracted along with that of the positron background since A_+ also contained a measure of the misidentified pions and assuming $A_{\pi^+} \sim A_{\pi^-}$.

3. False asymmetries

It is important to make sure that our experimental data are free from significant false asymmetries which could systematically shift the data. During the experiment, data were taken (either longitudinal or transverse) with the target B-field pointing in either one of the two possible directions. For each field direction, two different target polarization directions were used, parallel or antiparallel to the B-field. We then had four different configurations, and approximately the

TABLE X. Results for A_1 in the DIS region ($W^2 \geq 4\ \mathrm{GeV}^2$). There is an additional normalization uncertainty due to beam and target polarization shown in Table XV.

x	$\langle Q^2 \rangle$	E(GeV)	$A_1^p \pm \mathrm{stat} \pm \mathrm{syst}$	$A_1^d \pm \mathrm{stat} \pm \mathrm{syst}$	$A_1^n \pm \mathrm{stat} \pm \mathrm{syst}$
0.024	0.51	16.2	0.091±0.027±0.014	−0.049±0.068±0.009	−0.205±0.153±0.023
0.027	0.55	16.2	0.085±0.026±0.013	−0.018±0.065±0.009	−0.131±0.146±0.022
0.027	1.17	29.1	−0.034±0.068±0.010	−0.048±0.092±0.009	−0.073±0.225±0.020
0.031	0.59	16.2	0.084±0.026±0.012	0.019±0.065±0.008	−0.048±0.144±0.020
0.031	1.27	29.1	0.063±0.034±0.009	0.050±0.040±0.008	0.044±0.095±0.019
0.035	0.31	9.7	0.093±0.037±0.018	−0.027±0.055±0.008	−0.159±0.125±0.024
0.035	0.64	16.2	0.058±0.024±0.011	−0.015±0.062±0.007	−0.097±0.139±0.018
0.035	1.40	29.1	0.122±0.025±0.008	0.002±0.028±0.007	−0.126±0.069±0.017
0.039	0.33	9.7	0.022±0.037±0.018	0.035±0.053±0.008	0.053±0.122±0.024
0.039	0.68	16.2	0.072±0.024±0.011	0.098±0.060±0.007	0.140±0.136±0.017
0.039	1.52	29.1	0.083±0.023±0.008	0.059±0.026±0.007	0.041±0.063±0.016
0.044	0.35	9.7	0.103±0.037±0.019	0.003±0.054±0.008	−0.106±0.126±0.025
0.044	0.73	16.2	0.095±0.023±0.011	−0.039±0.052±0.006	−0.191±0.120±0.017
0.044	0.98	16.2	0.096±0.520±0.010	−0.944±1.296±0.008	−2.222±2.964±0.019
0.044	1.65	29.1	0.110±0.021±0.008	−0.019±0.025±0.006	−0.162±0.060±0.014
0.049	0.36	9.7	0.103±0.039±0.020	0.054±0.057±0.008	0.007±0.135±0.026
0.049	0.78	16.2	0.146±0.024±0.011	0.091±0.052±0.006	0.045±0.121±0.016
0.049	1.06	16.2	0.077±0.109±0.010	−0.104±0.280±0.008	−0.321±0.646±0.018
0.049	1.78	29.1	0.125±0.020±0.008	−0.016±0.024±0.005	−0.173±0.058±0.013
0.056	0.38	9.7	0.103±0.041±0.021	−0.046±0.059±0.009	−0.217±0.141±0.027
0.056	0.57	9.7	−0.217±1.891±0.014	2.991±2.465±0.007	7.031±5.978±0.020
0.056	0.83	16.2	0.109±0.025±0.011	0.007±0.054±0.006	−0.106±0.127±0.016
0.056	1.16	16.2	0.131±0.063±0.010	0.090±0.153±0.007	0.061±0.358±0.017
0.056	1.92	29.1	0.129±0.020±0.008	0.021±0.023±0.005	−0.095±0.058±0.012
0.063	0.40	9.7	0.071±0.043±0.022	−0.007±0.062±0.010	−0.096±0.149±0.029
0.063	0.60	9.7	−0.027±0.177±0.014	0.220±0.252±0.007	0.532±0.609±0.020
0.063	0.87	16.2	0.155±0.027±0.012	0.048±0.057±0.005	−0.064±0.135±0.016
0.063	1.26	16.2	0.050±0.046±0.010	−0.005±0.112±0.006	−0.068±0.262±0.016
0.063	2.07	29.1	0.136±0.020±0.008	0.020±0.023±0.004	−0.107±0.058±0.012
0.063	2.69	29.1	1.146±0.834±0.009	−0.309±2.063±0.006	−2.009±4.864±0.016
0.071	0.41	9.7	0.088±0.049±0.023	0.102±0.070±0.012	0.135±0.171±0.033
0.071	0.64	9.7	0.060±0.077±0.014	−0.074±0.109±0.007	−0.239±0.267±0.019
0.071	0.92	16.2	0.105±0.029±0.012	0.063±0.061±0.006	0.026±0.145±0.017
0.071	1.36	16.2	0.143±0.041±0.009	0.084±0.095±0.005	0.033±0.225±0.014
0.071	2.22	29.1	0.149±0.020±0.008	0.023±0.023±0.004	−0.115±0.059±0.011
0.071	2.91	29.1	0.340±0.122±0.010	0.052±0.139±0.006	−0.267±0.353±0.015
0.079	0.43	9.7	0.102±0.053±0.025	−0.016±0.075±0.015	−0.154±0.186±0.039
0.079	0.69	9.7	0.160±0.053±0.014	0.027±0.078±0.007	−0.120±0.194±0.019
0.079	0.97	16.2	0.120±0.031±0.013	−0.044±0.066±0.006	−0.241±0.159±0.017
0.079	1.47	16.2	0.134±0.039±0.009	−0.120±0.088±0.005	−0.437±0.212±0.014
0.079	2.38	29.1	0.191±0.021±0.009	0.043±0.025±0.004	−0.119±0.064±0.012
0.079	3.17	29.1	0.210±0.057±0.010	−0.031±0.065±0.005	−0.316±0.167±0.014
0.090	0.44	9.7	0.057±0.055±0.027	0.028±0.078±0.018	0.000±0.193±0.046
0.090	0.74	9.7	0.140±0.043±0.014	−0.030±0.062±0.007	−0.235±0.156±0.020
0.090	1.01	16.2	0.175±0.034±0.013	0.109±0.071±0.006	0.054±0.173±0.018
0.090	1.58	16.2	0.194±0.037±0.010	0.208±0.085±0.005	0.268±0.207±0.013
0.090	2.53	29.1	0.160±0.023±0.010	0.070±0.027±0.004	−0.022±0.071±0.013
0.090	3.48	29.1	0.152±0.040±0.010	0.061±0.045±0.004	−0.033±0.117±0.014
0.101	0.45	9.7	0.087±0.057±0.030	0.154±0.081±0.023	0.262±0.203±0.055
0.101	0.78	9.7	0.132±0.040±0.014	0.037±0.058±0.008	−0.069±0.147±0.021
0.101	1.06	16.2	0.217±0.037±0.012	0.057±0.077±0.006	−0.121±0.189±0.018
0.101	1.69	16.2	0.183±0.037±0.009	0.097±0.083±0.004	0.016±0.205±0.012

TABLE X. *(Continued).*

x	$\langle Q^2 \rangle$	E(GeV)	$A_1^p \pm \text{stat} \pm \text{syst}$	$A_1^d \pm \text{stat} \pm \text{syst}$	$A_1^n \pm \text{stat} \pm \text{syst}$
0.101	2.69	29.1	0.237±0.026±0.011	0.064±0.030±0.004	−0.129±0.079±0.014
0.101	3.79	29.1	0.199±0.033±0.010	0.055±0.038±0.004	−0.106±0.099±0.013
0.113	0.47	9.7	0.167±0.059±0.033	−0.012±0.086±0.028	−0.226±0.215±0.064
0.113	0.82	9.7	0.185±0.040±0.015	0.061±0.057±0.009	−0.075±0.147±0.023
0.113	1.10	16.2	0.164±0.041±0.013	0.052±0.083±0.007	−0.071±0.208±0.019
0.113	1.80	16.2	0.206±0.037±0.009	0.051±0.078±0.004	−0.126±0.196±0.012
0.113	2.84	29.1	0.243±0.028±0.012	0.079±0.033±0.005	−0.103±0.088±0.016
0.113	4.11	29.1	0.224±0.031±0.010	0.035±0.036±0.004	−0.187±0.094±0.013
0.128	0.48	9.7	−0.010±0.064±0.036	−0.087±0.092±0.031	−0.196±0.233±0.072
0.128	0.86	9.7	0.129±0.041±0.015	0.143±0.059±0.011	0.193±0.152±0.026
0.128	1.14	16.2	0.217±0.045±0.013	0.229±0.090±0.008	0.294±0.227±0.021
0.128	1.91	16.2	0.233±0.037±0.010	0.037±0.077±0.005	−0.197±0.194±0.014
0.128	3.00	29.1	0.228±0.031±0.013	0.187±0.037±0.006	0.176±0.098±0.018
0.128	4.44	29.1	0.243±0.031±0.010	0.080±0.035±0.005	−0.106±0.093±0.014
0.144	0.90	9.7	0.134±0.042±0.016	0.033±0.060±0.012	−0.085±0.158±0.029
0.144	1.18	16.2	0.218±0.049±0.013	0.199±0.099±0.009	0.218±0.251±0.023
0.144	2.03	16.2	0.258±0.038±0.011	0.085±0.078±0.006	−0.114±0.198±0.016
0.144	3.15	29.1	0.227±0.033±0.014	0.141±0.041±0.007	0.064±0.109±0.020
0.144	4.78	29.1	0.242±0.030±0.010	0.171±0.035±0.005	0.118±0.094±0.014
0.162	0.93	9.7	0.205±0.043±0.017	0.115±0.063±0.014	0.027±0.166±0.033
0.162	1.22	16.2	0.290±0.054±0.014	−0.108±0.108±0.011	−0.638±0.279±0.026
0.162	2.14	16.2	0.237±0.040±0.013	0.137±0.082±0.007	0.039±0.211±0.019
0.162	3.30	29.1	0.297±0.037±0.015	0.109±0.045±0.008	−0.112±0.124±0.021
0.162	5.13	29.1	0.269±0.030±0.011	0.084±0.035±0.005	−0.138±0.097±0.015
0.182	0.97	9.7	0.298±0.045±0.018	0.094±0.067±0.016	−0.148±0.178±0.036
0.182	1.25	16.2	0.237±0.060±0.014	0.200±0.121±0.012	0.198±0.315±0.029
0.182	2.25	16.2	0.258±0.043±0.014	0.237±0.087±0.008	0.261±0.227±0.022
0.182	3.45	29.1	0.326±0.041±0.015	0.175±0.051±0.009	0.013±0.140±0.023
0.182	5.49	29.1	0.309±0.031±0.011	0.214±0.037±0.006	0.132±0.102±0.017
0.205	1.00	9.7	0.251±0.048±0.017	0.017±0.071±0.016	−0.285±0.190±0.037
0.205	1.29	16.2	0.305±0.066±0.016	0.213±0.135±0.014	0.137±0.355±0.032
0.205	2.36	16.2	0.304±0.046±0.015	0.117±0.094±0.010	−0.109±0.250±0.024
0.205	3.59	29.1	0.278±0.045±0.015	0.159±0.057±0.010	0.032±0.160±0.025
0.205	5.86	29.1	0.370±0.033±0.012	0.132±0.039±0.008	−0.167±0.110±0.019
0.230	1.03	9.7	0.335±0.050±0.018	0.178±0.075±0.017	0.005±0.204±0.039
0.230	1.32	16.2	0.260±0.073±0.017	0.090±0.150±0.015	−0.123±0.401±0.035
0.230	2.47	16.2	0.381±0.050±0.016	0.116±0.104±0.011	−0.228±0.281±0.027
0.230	3.73	29.1	0.396±0.051±0.016	0.061±0.067±0.011	−0.398±0.189±0.027
0.230	6.23	29.1	0.272±0.036±0.013	0.173±0.043±0.009	0.067±0.123±0.022
0.259	1.35	16.2	0.249±0.082±0.019	0.138±0.169±0.016	0.014±0.457±0.037
0.259	2.57	16.2	0.496±0.055±0.017	0.127±0.114±0.012	−0.373±0.312±0.029
0.259	3.85	29.1	0.372±0.057±0.017	0.005±0.078±0.012	−0.529±0.225±0.029
0.259	6.60	29.1	0.480±0.039±0.014	0.081±0.048±0.011	−0.491±0.141±0.025
0.292	1.37	16.2	0.362±0.091±0.020	0.398±0.192±0.015	0.540±0.529±0.037
0.292	2.67	16.2	0.515±0.061±0.017	0.369±0.126±0.013	0.234±0.355±0.031
0.292	3.98	29.1	0.423±0.067±0.018	0.225±0.093±0.014	−0.026±0.273±0.033
0.292	6.97	29.1	0.409±0.043±0.016	0.216±0.055±0.012	−0.033±0.164±0.029
0.329	2.76	16.2	0.446±0.068±0.021	0.548±0.142±0.018	0.829±0.408±0.041
0.329	4.09	29.1	0.468±0.079±0.019	0.352±0.114±0.015	0.248±0.343±0.036
0.329	7.33	29.1	0.428±0.049±0.021	0.247±0.063±0.014	0.009±0.196±0.035
0.370	2.85	16.2	0.594±0.077±0.024	0.157±0.161±0.015	−0.515±0.476±0.038
0.370	4.20	29.1	0.349±0.096±0.021	0.362±0.143±0.017	0.469±0.443±0.040

TABLE X. *(Continued).*

x	$\langle Q^2 \rangle$	E(GeV)	$A_1^p \pm \text{stat} \pm \text{syst}$	$A_1^d \pm \text{stat} \pm \text{syst}$	$A_1^n \pm \text{stat} \pm \text{syst}$
0.370	7.69	29.1	0.448±0.057±0.023	0.343±0.075±0.016	0.243±0.239±0.040
0.416	2.93	16.2	0.589±0.087±0.021	0.235±0.186±0.015	−0.310±0.569±0.037
0.416	4.30	29.1	0.681±0.118±0.023	0.390±0.184±0.018	−0.020±0.588±0.043
0.416	8.03	29.1	0.611±0.067±0.022	0.232±0.091±0.018	−0.392±0.300±0.043
0.468	3.01	16.2	0.677±0.101±0.028	0.710±0.216±0.015	0.962±0.689±0.040
0.468	4.40	29.1	0.828±0.151±0.024	0.190±0.246±0.019	−0.940±0.814±0.044
0.468	8.37	29.1	0.589±0.082±0.025	0.335±0.113±0.020	−0.064±0.392±0.048
0.526	4.47	29.1	0.841±0.194±0.025	0.182±0.335±0.018	−1.063±1.150±0.044
0.526	8.67	29.1	0.678±0.102±0.028	0.508±0.147±0.022	0.304±0.530±0.053
0.592	4.55	29.1	0.479±0.255±0.026	0.672±0.464±0.016	1.249±1.639±0.042
0.592	8.98	29.1	0.695±0.133±0.031	0.065±0.198±0.024	−1.283±0.744±0.057
0.666	9.26	29.1	0.612±0.182±0.033	0.423±0.284±0.024	0.112±1.078±0.059
0.749	9.52	29.1	0.914±0.273±0.041	0.769±0.443±0.039	0.613±1.605±0.088

same amount of data were taken for each configuration, thus canceling out the electroweak contributions to our measurement so that no correction to the data was necessary. The asymmetries in each configuration were compared by looking at the χ^2 distributions of the asymmetry differences. For the proton, the χ^2 distributions were all nicely centered at one, and the mean value of the asymmetry differences was approximately one standard deviation from zero. For the deuteron the results were slightly worse, yet still very reasonable. The χ^2 distributions were centered around one with a few points greater than two, and the mean values of the asymmetry differences were within two standard deviations of zero. We conclude that there were no significant systematic effects on the asymmetry due to changes in target B-field or target enhancement field directions. Also, no statistically significant variation of the asymmetry was found for either NH_3 or ND_3 targets as a function of raster position.

4. Dilution factor

In general, incident electrons will scatter both from polarized target nucleons and unpolarized nuclei that are part of the target assembly. These unpolarized materials include liquid helium, ^{15}N, NMR pick-up coils, and vacuum windows. Scattering from unpolarized materials will dilute the measured asymmetry, and a correction must be applied. The dilution factor f is a function of x and Q^2, and is defined as the ratio of the total event rate from polarizable nucleons, to the

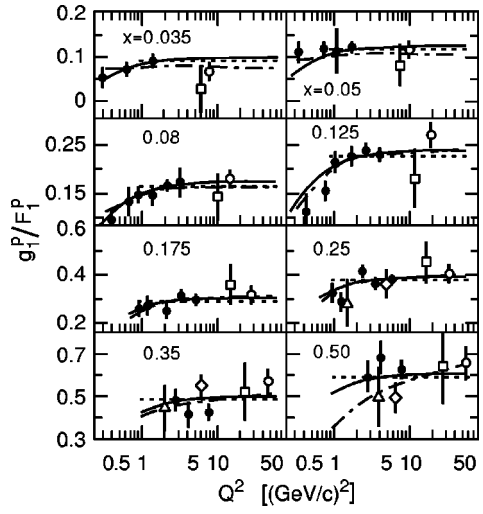

FIG. 13. g_1^p/F_1^p as a function of Q^2 for 8 different x bins. The data are from this experiment (solid circle), SMC [7] (open circle), EMC [6] (squares), SLAC E80 [2] (triangle), and SLAC E130 [3] (diamond). The dashed and solid curves correspond to global fits II (g_1/F_1 Q^2-independent) and III (g_1/F_1 Q^2-dependent) in Table XI, respectively. The E154 NLO pQCD fit [125] is shown as the dot-dashed curve.

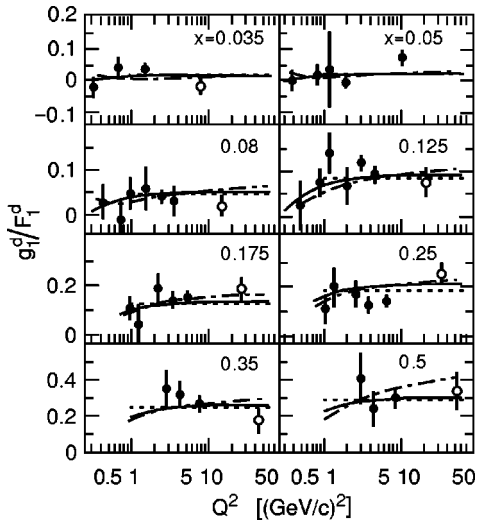

FIG. 14. g_1^d/F_1^d as a function of Q^2 for 8 different x bins. The data are from this experiment (solid circles) and SMC [7] (open circles). The dashed and solid curves correspond to global fits II (g_1/F_1 Q^2-independent) and III (g_1/F_1 Q^2-dependent) in Table XI, respectively. The E154 NLO pQCD fit [125] is shown as the dot-dashed curve.

TABLE XI. Coefficients for fits to all available data with $Q^2 \geqslant Q^2_{min}$ of the form $ax^\alpha(1+bx+cx^2)[1+Cf(Q^2)]$, along with the χ^2 for the indicated number of degrees of freedom, calculated with the statistical errors only. Fits I to IV are to g_1/F_1, while fit V is to A_1.

Fit to	Q^2_{min}	f(Q^2)	α	a	b	c	C	χ^2	DF
I. g_1^p/F_1^p	0.3	none	0.62	0.641	2.231	−2.666	0.000	145	117
II. g_1^p/F_1^p	1.0	none	0.64	0.749	1.466	−1.982	0.000	112	106
III. g_1^p/F_1^p	0.3	$1/Q^2$	0.62	0.762	1.434	−1.917	−0.160	116	116
IV. g_1^p/F_1^p	0.3	$-\ln(Q^2)$	0.66	0.728	0.850	−1.384	−0.100	120	116
V. A_1^p	0.3	$1/Q^2$	0.66	0.898	0.595	−0.371	−0.180	118	116
I. g_1^d/F_1^d	0.3	none	1.52	2.439	−1.718	0.867	0.000	122	111
II. g_1^d/F_1^d	1.0	none	1.46	2.222	−1.666	0.829	0.000	115	100
III. g_1^d/F_1^d	0.3	$1/Q^2$	1.44	2.342	−1.724	0.902	−0.260	119	110
IV. g_1^d/F_1^d	0.3	$-\ln(Q^2)$	1.48	2.030	−1.812	0.979	−0.100	120	110
V. A_1^d	0.3	$1/Q^2$	1.46	2.493	−1.915	1.376	−0.260	119	110

TABLE XII. Results for averaged g_1/F_1 for $Q^2 \geqslant 1$ (GeV/c)^2.

x	$\langle Q^2 \rangle$	$g_1^p/F_1^p \pm$ stat $\pm$ syst	$g_1^d/F_1^d \pm$ stat $\pm$ syst	$g_1^n/F_1^n \pm$ stat $\pm$ syst
0.031	1.27	0.064±0.034±0.009	0.041±0.040±0.008	0.021±0.095±0.019
0.035	1.40	0.123±0.025±0.008	0.008±0.029±0.007	−0.115±0.069±0.017
0.039	1.52	0.083±0.023±0.008	0.062±0.026±0.007	0.049±0.063±0.016
0.044	1.65	0.110±0.021±0.008	−0.013±0.025±0.006	−0.150±0.060±0.014
0.049	1.78	0.124±0.020±0.008	−0.014±0.024±0.005	−0.169±0.058±0.013
0.056	1.91	0.130±0.019±0.008	0.017±0.023±0.005	−0.105±0.057±0.012
0.063	2.04	0.125±0.018±0.008	0.013±0.022±0.004	−0.121±0.056±0.012
0.071	2.19	0.153±0.018±0.008	0.029±0.022±0.004	−0.108±0.056±0.011
0.079	2.41	0.179±0.018±0.009	0.024±0.022±0.004	−0.163±0.057±0.012
0.090	2.55	0.169±0.016±0.011	0.084±0.021±0.004	0.012±0.055±0.013
0.101	2.85	0.215±0.016±0.010	0.063±0.022±0.004	−0.110±0.056±0.013
0.113	3.13	0.217±0.016±0.011	0.057±0.022±0.005	−0.135±0.058±0.014
0.128	3.41	0.232±0.017±0.011	0.128±0.023±0.005	0.025±0.061±0.015
0.144	3.71	0.235±0.018±0.012	0.146±0.024±0.005	0.068±0.064±0.016
0.162	4.03	0.276±0.019±0.012	0.090±0.025±0.006	−0.139±0.068±0.017
0.182	4.34	0.296±0.020±0.013	0.200±0.027±0.007	0.102±0.074±0.019
0.205	4.15	0.319±0.020±0.014	0.109±0.027±0.009	−0.165±0.075±0.023
0.230	4.37	0.322±0.021±0.015	0.130±0.029±0.011	−0.103±0.083±0.026
0.259	5.26	0.434±0.026±0.015	0.103±0.036±0.011	−0.369±0.104±0.026
0.292	5.53	0.405±0.029±0.016	0.227±0.041±0.012	0.029±0.121±0.029
0.329	6.01	0.427±0.035±0.020	0.284±0.048±0.014	0.130±0.147±0.034
0.370	6.29	0.451±0.040±0.022	0.300±0.056±0.015	0.139±0.178±0.038
0.416	6.56	0.592±0.047±0.021	0.232±0.067±0.017	−0.371±0.221±0.039
0.468	6.79	0.608±0.056±0.024	0.319±0.083±0.018	−0.126±0.282±0.042
0.526	7.72	0.671±0.083±0.024	0.455±0.113±0.019	0.141±0.411±0.045
0.592	7.97	0.600±0.107±0.025	0.322±0.148±0.019	−0.191±0.557±0.045
0.666	9.26	0.478±0.165±0.026	0.251±0.226±0.019	−0.192±0.876±0.046
0.749	9.52	0.744±0.237±0.031	0.646±0.331±0.033	0.569±1.233±0.073

TABLE XIII. Results for averaged A_1 for $Q^2 \geqslant 1\ (\mathrm{GeV}/c)^2$.

x	$\langle Q^2 \rangle$	$A_1^p \pm \mathrm{stat} \pm \mathrm{syst}$	$A_1^d \pm \mathrm{stat} \pm \mathrm{syst}$	$A_1^n \pm \mathrm{stat} \pm \mathrm{syst}$
0.031	1.27	0.063±0.034±0.009	0.050±0.040±0.008	0.044±0.095±0.019
0.035	1.40	0.122±0.025±0.008	0.002±0.028±0.007	−0.126±0.069±0.017
0.039	1.52	0.083±0.023±0.008	0.059±0.026±0.007	0.041±0.063±0.016
0.044	1.65	0.110±0.021±0.008	−0.019±0.025±0.006	−0.162±0.060±0.014
0.049	1.78	0.123±0.020±0.008	−0.016±0.024±0.005	−0.175±0.058±0.013
0.056	1.91	0.130±0.019±0.008	0.023±0.023±0.005	−0.091±0.057±0.012
0.063	2.04	0.123±0.018±0.008	0.019±0.022±0.004	−0.105±0.056±0.012
0.071	2.19	0.152±0.018±0.009	0.028±0.022±0.004	−0.110±0.056±0.012
0.079	2.41	0.180±0.018±0.009	0.024±0.022±0.004	−0.165±0.057±0.012
0.090	2.55	0.168±0.016±0.011	0.080±0.022±0.004	0.004±0.055±0.014
0.101	2.85	0.214±0.016±0.011	0.063±0.022±0.004	−0.110±0.057±0.014
0.113	3.13	0.217±0.017±0.011	0.058±0.022±0.005	−0.135±0.059±0.015
0.128	3.41	0.232±0.017±0.011	0.128±0.023±0.005	0.025±0.061±0.016
0.144	3.71	0.238±0.018±0.012	0.154±0.024±0.006	0.081±0.065±0.017
0.162	4.03	0.272±0.019±0.012	0.086±0.026±0.007	−0.142±0.069±0.018
0.182	4.34	0.294±0.020±0.013	0.204±0.027±0.008	0.115±0.075±0.020
0.205	4.15	0.314±0.020±0.014	0.123±0.027±0.010	−0.122±0.076±0.024
0.230	4.37	0.325±0.022±0.015	0.142±0.030±0.011	−0.075±0.085±0.027
0.259	5.26	0.437±0.026±0.016	0.071±0.038±0.011	−0.457±0.108±0.027
0.292	5.53	0.432±0.030±0.017	0.245±0.043±0.013	0.036±0.127±0.031
0.329	6.01	0.441±0.036±0.021	0.308±0.052±0.015	0.180±0.157±0.036
0.370	6.29	0.471±0.041±0.023	0.319±0.061±0.016	0.162±0.192±0.040
0.416	6.56	0.616±0.049±0.022	0.258±0.074±0.018	−0.314±0.242±0.042
0.468	6.79	0.654±0.059±0.026	0.383±0.093±0.019	0.019±0.314±0.046
0.526	7.72	0.713±0.090±0.027	0.456±0.135±0.022	0.064±0.481±0.051
0.592	7.97	0.649±0.118±0.030	0.159±0.182±0.023	−0.851±0.677±0.054
0.666	9.26	0.612±0.182±0.033	0.423±0.284±0.024	0.112±1.078±0.059
0.749	9.52	0.914±0.273±0.041	0.769±0.443±0.039	0.613±1.605±0.088

total event rate from all target materials. The measured asymmetry is then corrected for unpolarized events by dividing by the dilution factor.

For a material of density ρ and thickness z, the event rate from Born processes was calculated as follows:

$$r(x,Q^2) = \rho z [Z F_2^p(x,Q^2) + N F_2^n(x,Q^2)] g_{EMC}(x,Q^2), \tag{47}$$

where Z and N are the number of protons and neutrons in the nucleus. F_2^p and F_2^n are unpolarized proton and neutron deep-inelastic structure functions. They were obtained from a parameterization of the NMC data [107]. The factor g corrects for the ''EMC effect'' which accounts for the difference in nucleon cross sections for free and bound nucleons.

With this model for rates, the dilution factor can then be calculated as follows:

$$f(x,Q^2) = \left(\frac{r_{pol}(x,Q^2)}{r_{pol}(x,Q^2) + \Sigma_i r_i(x,Q^2)} \right) \times r_c, \tag{48}$$

where we are summing the rates from all unpolarized materials which contribute to the overall event rate. The factor r_c corrects the dilution factor for radiative effects and was typically less than a 5% correction.

The target material was in the form of frozen granules which were tightly packed into a target cell. The volume fraction of the target cell which the target material occupied is known as the packing fraction, and was determined independently by three different methods. The first consisted of studying the difference in event rates for empty, carbon, and full target cells. The second method was a measurement of the attenuation of a mono-energetic X-ray beam as it passed through the target material. The attenuation of the incident beam is directly related to the thickness and attenuation coefficient of material it passes through, and was therefore sensitive to the packing fraction. Finally, the target material was weighed, and the packing fraction was determined using the known volume of the target cell. The measured packing fraction was different for each target used, and varied from 0.57 to 0.64.

Over the kinematic range of interest, the dilution factor typically varied from 0.15–0.19 for the NH_3 target and from

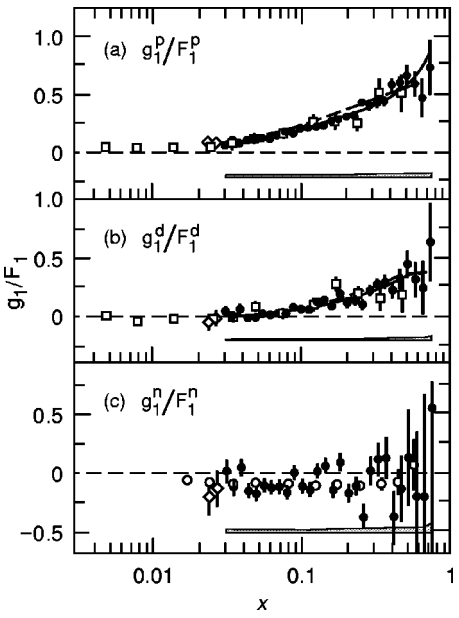

FIG. 15. g_1/F_1 averaged over all beam energies and spectrometer angles as a function of x. The solid circles are at $Q^2 \geqslant 1\,(\mathrm{GeV}/c)^2$, while the diamonds are at $Q^2 \leqslant 1\,(\mathrm{GeV}/c)^2$ for $x \leqslant 0.03$. The data from SMC [7] (squares) are shown for proton and deuteron, and the data from E154 [11] (open circles) are shown for neutron. The curves are NLO pQCD fits by Altarelli, Ball, Forte, and Ridolfi [37] (solid) and Glück, Reya, Stratmann, and Vogelsang [59] (dashed).

$0.23-0.25$ for the ND_3 target, with relative errors of 2% and 1.5%, respectively. The error on the dilution factor comes from several sources. The packing fraction was known to 4% for both targets. The relative error from the cross-section ratio σ_n/σ_p was 1.0% [108]. This was one of the dominant errors for the NH_3 target and did not contribute to the ND_3 target. The ratio of nuclear to deuterium cross sections, the EMC effect, is known to 1.5% relative and was another large source of error. This effect has a 1% overall normalization and another 1% uncorrelated error [106]. The small mass of the NMR coil (~ 0.1 gm) was known to 20% but did not contribute significantly to the overall error.

5. Dead time

All the signals from various detectors went through discriminators before forming the various triggers. These discriminators have an output pulse width of 25 ns and a double pulse resolution of 8 ns. They were operated in an updating mode such that a second signal entering the discriminator after 8 ns and before 25 ns produced a single output pulse with an extended width. The effective dead time was 32 ns instead of 25 ns, due to slight mis-timing between various signals and signal jitter, especially from the shower counters. Rates measured with each beam helicity were corrected separately.

Using a Monte Carlo simulation, the probability matrix $M(i,j)$ for observing i hits when there were really j hits was generated using a typical spill length of 2200 ns and a dead time of 32 ns as inputs. The observed trigger frequency distribution $T_o(i)$ is related to the true distribution (without dead time) $T_t(i)$ by

$$T_o(i) = \sum_j M(i,j) \times T_t(j). \tag{49}$$

Since there are practically no hits beyond 10, the sum is safely truncated at $j=16$. The matrix M is inverted to solve for $T_t(i)$, and the dead time correction factor d to the measured rates is defined as

$$d = \frac{\Sigma_{i=1}^{16} i T_t(i)}{\Sigma_{i=1}^{4} i T_o(i) + 4\Sigma_{i=5}^{16} T_o(i)}. \tag{50}$$

Here, the sum over T_o is split into two parts because only four triggers could be recorded per beam spill.

The correction factor varies smoothly from 1 at very low rates to 1.07 at an average rate of 2 events/pulse. The systematic error on the corrections was calculated assuming upper and lower limits to the beam width of 2600 ns and 1800 ns. The dead time was found to be accurate to a few parts in 1000, and the error for the corrected asymmetry by applying these factors is found to be less than 2×10^{-5}, which is completely negligible. No uncertainty in the dead time itself was considered because only the ratio of the beam spill length to the dead time is important.

6. Radiative corrections

Our experimental goal was to measure a single photon exchange process (Born) at specific kinematics. In reality there are higher order contributing processes (internal), and the actual scattering kinematics can change due to energy losses in materials along the electrons' paths (external). The radiative corrections account for these unwanted effects.

The radiative correction calculation is different for the unpolarized (σ^u) and polarized (σ^p) components of the helicity-dependent cross sections which are given by $\sigma^{\uparrow\downarrow}$ and $\sigma^{\uparrow\uparrow}$ for a longitudinally polarized target, and $\sigma^{\rightarrow\downarrow}$ and $\sigma^{\rightarrow\uparrow}$ for a transversely polarized target. The longitudinal and transverse asymmetries can be written as

$$A_\parallel = \frac{\sigma^{\uparrow\downarrow} - \sigma^{\uparrow\uparrow}}{\sigma^{\uparrow\downarrow} + \sigma^{\uparrow\uparrow}} = \frac{(\sigma^u + \sigma^{p\uparrow}) - (\sigma^u - \sigma^{p\uparrow})}{(\sigma^u + \sigma^{p\uparrow}) + (\sigma^u - \sigma^{p\uparrow})} = \frac{\sigma^{p\uparrow}}{\sigma^u},$$

$$A_\perp = \frac{\sigma^{\rightarrow\downarrow} - \sigma^{\rightarrow\uparrow}}{\sigma^{\rightarrow\downarrow} + \sigma^{\rightarrow\uparrow}} = \frac{(\sigma^u + \sigma^{p\rightarrow}) - (\sigma^u - \sigma^{p\rightarrow})}{(\sigma^u + \sigma^{p\rightarrow}) + (\sigma^u - \sigma^{p\rightarrow})} = \frac{\sigma^{p\rightarrow}}{\sigma^u}, \tag{51}$$

which is equally valid for Born, internally radiated, or fully radiated cross sections and asymmetries. For the remainder of the radiative correction discussion, quantities which are Born, internally radiated, or fully radiated are subscripted with 0, r, and R respectively. Also, for simplicity, references to a particular target polarization are dropped such that A could be either $A_\parallel$ or $A_\perp$, and σ^p could be either $\sigma^{p\uparrow}$ or $\sigma^{p\rightarrow}$.

Calculation of the polarization-dependent internal corrections was done using code based on the work of Kuchto,

TABLE XIV. Results for g_1 obtained from average g_1/F_1 for $Q^2 \geq 1$ ((GeV/c)^2). Not included in the systematic errors listed are normalization uncertainties shown in Table XV.

$\langle x \rangle$	x range	$\langle Q^2 \rangle$	$g_1^p \pm$stat$\pm$syst	$g_1^d \pm$stat$\pm$syst	$g_1^n \pm$stat$\pm$syst
0.031	0.029–0.033	1.27	0.248±0.132±0.034	0.150±0.147±0.030	0.077±0.345±0.074
0.035	0.033–0.037	1.40	0.436±0.089±0.032	0.027±0.097±0.025	−0.378±0.227±0.063
0.039	0.037–0.042	1.52	0.269±0.073±0.025	0.191±0.080±0.021	0.145±0.188±0.054
0.044	0.042–0.047	1.65	0.322±0.062±0.022	−0.036±0.068±0.017	−0.401±0.160±0.043
0.049	0.047–0.053	1.78	0.327±0.053±0.019	−0.034±0.059±0.013	−0.405±0.139±0.036
0.056	0.053–0.059	1.91	0.309±0.045±0.017	0.039±0.052±0.010	−0.224±0.121±0.029
0.063	0.059–0.067	2.04	0.266±0.039±0.015	0.027±0.045±0.008	−0.230±0.106±0.023
0.071	0.067–0.075	2.19	0.294±0.034±0.014	0.053±0.041±0.006	−0.182±0.095±0.021
0.079	0.075–0.084	2.41	0.310±0.031±0.014	0.039±0.037±0.005	−0.245±0.086±0.019
0.090	0.084–0.095	2.55	0.260±0.024±0.012	0.123±0.031±0.005	0.015±0.073±0.019
0.101	0.095–0.107	2.85	0.299±0.022±0.012	0.082±0.029±0.004	−0.130±0.067±0.017
0.113	0.107–0.120	3.13	0.272±0.021±0.011	0.067±0.026±0.003	−0.142±0.061±0.015
0.128	0.120–0.136	3.41	0.262±0.019±0.010	0.135±0.024±0.004	0.023±0.057±0.017
0.144	0.136–0.153	3.71	0.239±0.018±0.010	0.138±0.022±0.004	0.056±0.052±0.017
0.162	0.153–0.172	4.03	0.253±0.017±0.010	0.075±0.021±0.003	−0.100±0.049±0.014
0.182	0.172–0.193	4.34	0.243±0.016±0.009	0.147±0.020±0.005	0.064±0.046±0.018
0.205	0.193–0.218	4.15	0.231±0.014±0.009	0.070±0.017±0.005	−0.088±0.040±0.015
0.230	0.218–0.245	4.37	0.206±0.014±0.008	0.072±0.016±0.005	−0.047±0.038±0.014
0.259	0.245–0.276	5.26	0.242±0.014±0.008	0.049±0.017±0.004	−0.140±0.040±0.013
0.292	0.276–0.310	5.53	0.192±0.014±0.007	0.089±0.016±0.004	0.009±0.037±0.013
0.329	0.310–0.349	6.01	0.168±0.014±0.006	0.091±0.015±0.004	0.032±0.036±0.013
0.370	0.349–0.393	6.29	0.144±0.013±0.005	0.076±0.014±0.004	0.026±0.034±0.011
0.416	0.393–0.442	6.56	0.148±0.012±0.005	0.045±0.013±0.003	−0.051±0.030±0.009
0.468	0.442–0.497	6.79	0.114±0.011±0.004	0.045±0.012±0.002	−0.012±0.027±0.007
0.526	0.497–0.559	7.72	0.084±0.010±0.003	0.043±0.011±0.002	0.009±0.025±0.006
0.592	0.559–0.629	7.97	0.048±0.009±0.002	0.019±0.009±0.001	−0.007±0.021±0.003
0.666	0.629–0.708	9.26	0.021±0.007±0.001	0.008±0.007±0.001	−0.004±0.017±0.001
0.749	0.708–0.791	9.52	0.015±0.005±0.001	0.009±0.005±0.001	0.005±0.011±0.001

Shumeiko, and Akusevich [109], who are also responsible for the development of their own code POLRAD. The two codes were carefully compared and found to be completely equivalent when the same input models were used. The calculation of the internally radiated cross sections can be decomposed into components:

$$\sigma_r^p = \sigma_0^p(1+\delta_v) + \sigma_{el}^p + \sigma_q^p + \sigma_{in}^p,$$

$$\sigma_r^u = \sigma_0^u(1+\delta_v) + \sigma_{el}^u + \sigma_q^u + \sigma_{in}^u, \qquad (52)$$

where δ_v includes corrections for the electron vertex and vacuum polarization contributions, as well as a term that is left after the infrared-divergent contributions are cancelled out. The vacuum polarization correction includes contributions from both leptons and light quarks. The terms σ_{el}, σ_q, and σ_{in} are the radiative tails due to internal bremsstrahlung (occurring within the field of the scattering nucleon) for elastic, quasielastic, and inelastic scattering processes.

The nuclear elastic tail for the deuteron was evaluated using fits to data [110] over a large range in Q^2. The elastic tail for the proton (and quasielastic for the deuteron) were evaluated using various form factor models [111] which agree well with existing data over the kinematic region. Note that some of these models agree well with data for some of the four elastic form factors and not others, so different models were combined for the best representation of all four nucleon elastic form factors. Quasielastic cross sections were Fermi-smeared only for corrections to our resonance data since this smearing has a negligible impact on the radiative correction in the deep-inelastic region. Unpolarized cross sections were modeled using fits to structure function data in the deep-inelastic region [107,83], and fits to cross sections in the resonance region [112,113]. The polarized component to the deep-inelastic cross sections was modeled using Q^2-dependent fits to A_1 as given in this paper. The polarized resonance region model was based on parametrizations of previous data and data presented here. For the transverse contributions, we used $g_2 = g_2^{WW}$ [73] or $g_2 = 0$ which are both consistent with our data.

The external corrections account for bremsstrahlung radiative effects which occur as the electrons pass through ma-

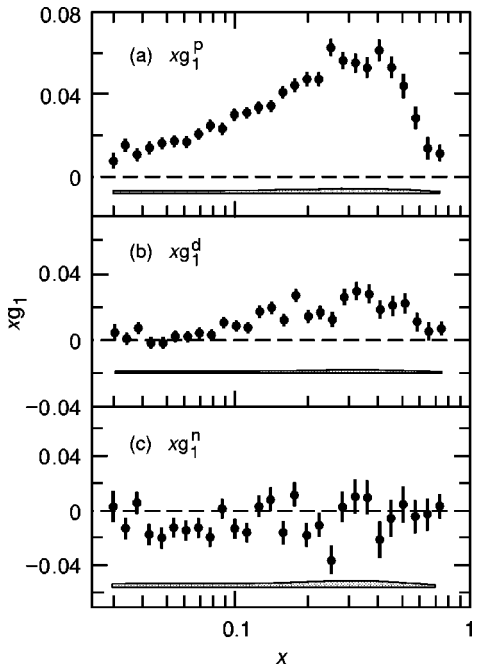

FIG. 16. $xg_1(x,Q^2)$ evaluated at the average measured Q^2 at each x.

terial in their path. Ionization effects were completely negligible at our kinematics. At any given interaction point within the target the radiative correction depends on the amount of material (in radiation lengths) the electron sees before (t_b) and after (t_a) scattering. Because the radiation lengths before and after scattering did not vary significantly over the beam raster area, it was not necessary to integrate the external corrections over the raster area. Also, it was an excellent approximation to replace the target integration over the length of the target with the evaluation of the external radiative corrections at one point, namely the center of the target. At this point, $t_b=0.026$, $t_a=0.047$ for the 4.5° spectrometer, and $t_a=0.040$ for the 7° spectrometer. These radiation lengths, which are valid for both our proton and deuteron polarized target, are dominated by the target material, but also include contributions from various windows which are not part of the polarized target itself. The external corrections were thus calculated using [114]

$$\sigma_R^p(E_0,E_F',\theta)=\int_{E_{min}}^{E_o}\int_{E_F'}^{E'_{max}} I_b(E_0,E,t_b)\sigma_r^p(E,E',\theta) \times I_b(E',E_F',t_a)[1-D(E_0,E,Z)]dEdE'$$

$$\sigma_R^u(E_0,E_F',\theta)=\int_{E_{min}}^{E_o}\int_{E_F'}^{E'_{max}} I_b(E_0,E,t_b)\sigma_r^u(E,E',\theta) \times I_b(E',E_F',t_a)dEdE' \quad (53)$$

where E_0 is the electron initial energy, E_F' is the final scattered electron momentum, and E_{min} and E'_{max} are the minimum incident energy and maximum scattered energy as defined by elastic scattering. $I_b(E_1,E_2,t)$ is the probability [114] that a particle with initial energy E_1 ends up with energy E_2 after passing through a radiator of thickness t, and $D(E_0,E,Z)$ is the electron depolarization correction [115] which corrects for the depolarization of the electron beam due to the bremsstrahlung emission of polarized photons. This correction depends weakly on the Z of the target material.

TABLE XV. Normalization systematic uncertainties (%).

Parameter	Proton	Deuteron
Beam polarization	2.4	2.4
Target polarization	2.5	4.0
Dilution factor	1.2	1.4
Nitrogen correction	0.4	
Total	3.7	4.9

An additive correction A_{rc} to the data was formed by taking the difference between the fully radiated and Born model asymmetries

$$A_{rc}=A_0-A_R=\frac{\sigma_0^p}{\sigma_0^u}-\frac{\sigma_R^p}{\sigma_R^u}. \quad (54)$$

Our fits to A_1 and the radiative corrections were iterated until they converged. For the purposes of statistical error propagation on our measured asymmetries, a ''radiative correction dilution factor'' f_{rc} was evaluated. This dilution factor is simply a ratio of events coming from deep-inelastic processes to all events and multiplies the usual dilution factor in Eq. (38). We only used f_{rc} for the error propagation and not for correcting the data directly. Systematic uncertainties were estimated by varying input models within reasonable limits and measuring how much the radiative correction changed. These uncertainties for the various models were then combined in quadrature for each x bin. Results for A_{rc} are listed with data in Tables III–VIII, XVI–XIX, and XXXVI–XXXVII.

C. Analysis of resonance region data

The resonance data [116] were taken with a 9.7 GeV beam. The spectrometer angles of 4.5° and 7° corresponded to $Q^2\simeq 0.5$ and 1.2 $(\mathrm{GeV}/c)^2$ in the resonance region ($W^2<5\,\mathrm{GeV}^2$), respectively. We have extracted g_1 from the measured asymmetries $A_\parallel$, and from the absolute cross-section differences given in Eq. (7). Each method has its own set of systematic errors. The difference method requires good knowledge of spectrometer acceptances, the number density of polarizable protons or deuterons in the target, and detector efficiencies. The asymmetry method requires knowledge of the dilution factor for the resonance region, which means an accurate model of the rapidly varying unpolarized cross sections is needed. We found that the two methods agreed to within a fraction of the statistical errors on each point (typically better than 3%). In our previous report [16] we have used the difference method. The current reanalysis uses the asymmetry method, since we now believe that the systematic

TABLE XVI. Significant systematic errors for g_1^d for $E=29$ GeV. The beam and target polarization errors are each completely correlated and the F_2 error includes a correlated normalization error of $\sim 1\%$.

x	Q^2	f	F_2	R	P_B	P_T	A_{rc}	Total
				$\theta=4.5°$				
0.031	1.30	0.0010	0.0009	0.0016	0.0018	0.0030	0.0298	0.0301
0.035	1.40	0.0010	0.0009	0.0014	0.0018	0.0030	0.0249	0.0252
0.050	1.80	0.0011	0.0012	0.0011	0.0020	0.0033	0.0130	0.0137
0.080	2.30	0.0013	0.0015	0.0007	0.0023	0.0038	0.0044	0.0066
0.125	2.90	0.0014	0.0017	0.0005	0.0025	0.0041	0.0024	0.0058
0.175	3.40	0.0014	0.0018	0.0003	0.0025	0.0042	0.0031	0.0062
0.250	3.80	0.0013	0.0017	0.0001	0.0023	0.0038	0.0039	0.0063
0.350	4.10	0.0009	0.0014	0.0001	0.0017	0.0029	0.0037	0.0053
0.500	4.40	0.0005	0.0008	0.0000	0.0009	0.0015	0.0018	0.0027
				$\theta=7.0°$				
0.080	3.40	0.0013	0.0016	0.0029	0.0024	0.0040	0.0067	0.0089
0.125	4.40	0.0014	0.0017	0.0016	0.0026	0.0044	0.0027	0.0064
0.175	5.30	0.0014	0.0018	0.0009	0.0026	0.0044	0.0028	0.0063
0.250	6.40	0.0013	0.0017	0.0005	0.0023	0.0039	0.0035	0.0061
0.350	7.50	0.0009	0.0013	0.0003	0.0017	0.0028	0.0032	0.0048
0.500	8.60	0.0004	0.0006	0.0001	0.0007	0.0012	0.0018	0.0024
0.700	9.30	0.0001	0.0001	0.0000	0.0002	0.0003	0.0003	0.0005

TABLE XVII. Significant systematic errors for g_1^d/F_1^d for $E=29$ GeV. The beam and target polarization errors are each completely correlated.

x	Q^2	f	R	P_B	P_T	A_{rc}	Total
			$\theta=4.5°$				
0.031	1.30	0.0003	0.0005	0.0005	0.0008	0.0080	0.0081
0.035	1.40	0.0003	0.0006	0.0005	0.0009	0.0074	0.0075
0.050	1.80	0.0004	0.0009	0.0008	0.0013	0.0052	0.0055
0.080	2.30	0.0008	0.0020	0.0014	0.0023	0.0027	0.0044
0.125	2.90	0.0013	0.0040	0.0023	0.0039	0.0023	0.0066
0.175	3.40	0.0018	0.0053	0.0033	0.0055	0.0041	0.0095
0.250	3.80	0.0025	0.0063	0.0046	0.0077	0.0080	0.0138
0.350	4.10	0.0032	0.0077	0.0059	0.0099	0.0124	0.0189
0.500	4.40	0.0037	0.0084	0.0068	0.0114	0.0139	0.0213
				$\theta=7.0°$			
0.080	3.40	0.0008	0.0017	0.0014	0.0023	0.0039	0.0051
0.125	4.40	0.0013	0.0030	0.0024	0.0039	0.0024	0.0061
0.175	5.30	0.0019	0.0041	0.0034	0.0056	0.0035	0.0087
0.250	6.40	0.0026	0.0060	0.0047	0.0078	0.0071	0.0132
0.350	7.50	0.0032	0.0082	0.0060	0.0099	0.0115	0.0185
0.500	8.60	0.0037	0.0099	0.0069	0.0114	0.0166	0.0238
0.700	9.30	0.0037	0.0101	0.0069	0.0115	0.0132	0.0217

TABLE XVIII. Significant systematic errors for g_1^p for $E=29$ GeV. The beam and target polarization errors are each completely correlated and the F_2 error includes a correlated normalization error of $\sim 1\%$.

x	Q^2	f	F_2	R	P_B	P_T	A_{rc}	Total
				$\theta=4.5°$				
0.031	1.30	0.0052	0.0062	0.0104	0.0071	0.0074	0.0320	0.0361
0.035	1.40	0.0053	0.0061	0.0085	0.0070	0.0073	0.0269	0.0310
0.050	1.80	0.0051	0.0059	0.0049	0.0068	0.0071	0.0156	0.0206
0.080	2.30	0.0047	0.0056	0.0023	0.0064	0.0067	0.0094	0.0153
0.125	2.90	0.0043	0.0055	0.0014	0.0060	0.0063	0.0060	0.0128
0.175	3.40	0.0041	0.0054	0.0008	0.0057	0.0060	0.0047	0.0117
0.250	3.80	0.0036	0.0050	0.0003	0.0052	0.0054	0.0038	0.0104
0.350	4.10	0.0028	0.0039	0.0001	0.0041	0.0043	0.0033	0.0083
0.500	4.40	0.0016	0.0022	0.0000	0.0024	0.0025	0.0017	0.0047
				$\theta=7.0°$				
0.080	3.40	0.0046	0.0059	0.0095	0.0066	0.0069	0.0130	0.0202
0.125	4.40	0.0046	0.0057	0.0042	0.0064	0.0067	0.0070	0.0143
0.175	5.30	0.0043	0.0056	0.0022	0.0060	0.0063	0.0043	0.0122
0.250	6.40	0.0037	0.0050	0.0012	0.0053	0.0055	0.0027	0.0102
0.350	7.50	0.0027	0.0037	0.0006	0.0040	0.0041	0.0020	0.0076
0.500	8.60	0.0014	0.0018	0.0002	0.0020	0.0021	0.0012	0.0039
0.700	9.30	0.0003	0.0005	0.0000	0.0005	0.0005	0.0004	0.0010

TABLE XIX. Significant systematic errors for g_1^p/F_1^p for $E=29$ GeV. The beam and target polarization errors are each completely correlated.

x	Q^2	f	R	P_B	P_T	A_{rc}	Total
			$\theta=4.5°$				
0.031	1.30	0.0013	0.0030	0.0018	0.0019	0.0082	0.0092
0.035	1.40	0.0015	0.0034	0.0020	0.0021	0.0076	0.0089
0.050	1.80	0.0019	0.0040	0.0026	0.0027	0.0059	0.0083
0.080	2.30	0.0027	0.0062	0.0037	0.0039	0.0055	0.0102
0.125	2.90	0.0037	0.0095	0.0052	0.0055	0.0052	0.0138
0.175	3.40	0.0048	0.0111	0.0068	0.0071	0.0055	0.0165
0.250	3.80	0.0062	0.0122	0.0089	0.0093	0.0066	0.0199
0.350	4.10	0.0079	0.0146	0.0114	0.0119	0.0091	0.0251
0.500	4.40	0.0096	0.0175	0.0140	0.0146	0.0100	0.0301
			$\theta=7.0°$				
0.080	3.40	0.0025	0.0051	0.0036	0.0038	0.0072	0.0106
0.125	4.40	0.0038	0.0073	0.0053	0.0055	0.0057	0.0126
0.175	5.30	0.0048	0.0086	0.0069	0.0071	0.0049	0.0148
0.250	6.40	0.0063	0.0115	0.0090	0.0094	0.0045	0.0190
0.350	7.50	0.0079	0.0156	0.0115	0.0120	0.0057	0.0248
0.500	8.60	0.0096	0.0206	0.0142	0.0148	0.0081	0.0317
0.700	9.30	0.0100	0.0229	0.0149	0.0156	0.0129	0.0355

TABLE XX. Deuteron results for g_1 at fixed Q^2 of 2, 3, and 5 $(\mathrm{GeV}/c)^2$ evaluated assuming g_1/F_1 is independent of Q^2. In addition to the systematic errors shown, there are normalization uncertainties shown in Table XV.

x	$g_1^d(Q^2=2)\pm\mathrm{stat}\pm\mathrm{syst}$	$g_1^d(Q^2=3)\pm\mathrm{stat}\pm\mathrm{syst}$	$g_1^d(Q^2=5)\pm\mathrm{stat}\pm\mathrm{syst}$
0.031	0.166±0.162±0.033	0.180±0.176±0.036	0.198±0.194±0.040
0.035	0.029±0.104±0.027	0.031±0.112±0.029	0.034±0.124±0.032
0.039	0.202±0.084±0.022	0.218±0.091±0.024	0.239±0.100±0.027
0.044	−0.038±0.071±0.017	−0.040±0.076±0.019	−0.044±0.083±0.020
0.049	−0.035±0.060±0.014	−0.037±0.064±0.014	−0.040±0.070±0.016
0.056	0.040±0.052±0.011	0.042±0.056±0.011	0.046±0.061±0.012
0.063	0.027±0.045±0.008	0.028±0.048±0.008	0.031±0.052±0.009
0.071	0.053±0.040±0.006	0.056±0.042±0.007	0.060±0.046±0.007
0.079	0.038±0.036±0.005	0.040±0.038±0.005	0.044±0.041±0.006
0.090	0.120±0.030±0.005	0.125±0.032±0.005	0.135±0.034±0.005
0.101	0.079±0.028±0.004	0.083±0.029±0.004	0.089±0.031±0.004
0.113	0.064±0.025±0.003	0.067±0.026±0.004	0.072±0.028±0.004
0.128	0.128±0.023±0.004	0.133±0.024±0.004	0.141±0.025±0.004
0.144	0.130±0.021±0.004	0.135±0.022±0.004	0.142±0.023±0.004
0.162	0.071±0.020±0.003	0.073±0.020±0.004	0.076±0.021±0.004
0.182	0.141±0.019±0.004	0.143±0.019±0.004	0.148±0.020±0.005
0.205	0.068±0.017±0.005	0.069±0.017±0.005	0.070±0.017±0.005
0.230	0.071±0.016±0.005	0.071±0.016±0.005	0.072±0.016±0.005
0.259	0.049±0.017±0.004	0.049±0.017±0.004	0.049±0.017±0.004
0.292	0.094±0.017±0.004	0.092±0.016±0.004	0.090±0.016±0.004
0.329	0.100±0.017±0.004	0.096±0.016±0.004	0.092±0.016±0.004
0.370	0.089±0.017±0.004	0.083±0.016±0.004	0.078±0.015±0.004
0.416	0.057±0.016±0.004	0.051±0.015±0.003	0.047±0.014±0.003
0.468	0.064±0.017±0.004	0.055±0.014±0.003	0.048±0.012±0.002
0.526	0.074±0.019±0.004	0.060±0.015±0.003	0.049±0.012±0.002
0.592	0.043±0.020±0.002	0.031±0.014±0.002	0.023±0.011±0.001
0.666	0.026±0.024±0.002	0.017±0.016±0.001	0.011±0.010±0.001
0.749	0.048±0.025±0.002	0.028±0.014±0.001	0.016±0.008±0.001

errors are slightly better in this case. Other improvements on Ref. [16] include better modeling of the resonance region for radiative and resolution effects.

The resonance asymmetries were calculated as specified in Sec. IV B for the deep-inelastic analysis. In the present case, we have determined the dilution factor f using a Monte Carlo routine as described below. The term A_{rc} also included a resolution correction in the resonance region.

We developed a Monte Carlo code which simulated all relevant aspects of the experiment. It was used to predict total count rates and count rate differences from a set of tables of cross sections and asymmetries generated by the radiative corrections routine. The unpolarized cross sections came from parametrizations for the resonance region [112] and the deep-inelastic region [107,83]. The asymmetries contain both resonant and non-resonant contributions. The resonance contribution was calculated using the code AO [117], which includes parametrizations of all of the existing resonance data; however, the helicity amplitudes $A_{1/2}$ and $A_{3/2}$ for S_{11} and D_{13} were tuned to agree with our data. The non-resonant part came from a parameterization of all existing deep-inelastic data (fit III of Ref. [5]), which was extrapolated into the resonance region. Specifically, for $W^2 < 2.5\ \mathrm{GeV}^2$, A_1 was given by the tuned AO result alone; above $W^2 = 3.0\ \mathrm{GeV}^2$, A_1 was taken as the sum of the AO resonant contribution and the fit III inelastic background; and in the region $2.5 < W^2 < 3.0\ \mathrm{GeV}^2$ the two extremes were linearly interpolated. A_2 was calculated using g_2^{WW}, which yields values close to zero. The model-dependence of this choice for A_2 was determined by alternately considering $g_2 = 0$ and $A_2 = 0$.

The observed raw parallel asymmetry $A_\parallel^{raw}$ is proportional to the combination of photon asymmetries $A_1 + \eta A_2$. Therefore, we first extracted $A_1 + \eta A_2$ from the data, and then deduced g_1 from this using various assumptions about g_2. The following steps were required to produce $A_1 + \eta A_2$ and g_1:

(1) The radiative corrections code was run with the options as specified above to create the Born cross sections, the

TABLE XXI. Proton results for g_1 at fixed Q^2 of 2, 3, and 5 $(\mathrm{GeV}/c)^2$ evaluated assuming g_1/F_1 is independent of Q^2. In addition to the systematic errors shown, there are normalization uncertainties shown in Table XV.

x	$g_1^p(Q^2=2)\pm\mathrm{stat}\pm\mathrm{syst}$	$g_1^p(Q^2=3)\pm\mathrm{stat}\pm\mathrm{syst}$	$g_1^p(Q^2=5)\pm\mathrm{stat}\pm\mathrm{syst}$
0.031	$0.272\pm0.145\pm0.037$	$0.294\pm0.157\pm0.040$	$0.322\pm0.172\pm0.044$
0.035	$0.468\pm0.096\pm0.032$	$0.504\pm0.103\pm0.035$	$0.552\pm0.113\pm0.041$
0.039	$0.283\pm0.077\pm0.026$	$0.304\pm0.083\pm0.028$	$0.333\pm0.091\pm0.031$
0.044	$0.334\pm0.065\pm0.022$	$0.357\pm0.069\pm0.024$	$0.390\pm0.075\pm0.027$
0.049	$0.334\pm0.054\pm0.019$	$0.357\pm0.058\pm0.020$	$0.389\pm0.063\pm0.023$
0.056	$0.312\pm0.046\pm0.017$	$0.332\pm0.049\pm0.018$	$0.362\pm0.053\pm0.020$
0.063	$0.267\pm0.039\pm0.014$	$0.283\pm0.041\pm0.016$	$0.308\pm0.045\pm0.017$
0.071	$0.292\pm0.034\pm0.013$	$0.309\pm0.036\pm0.014$	$0.336\pm0.039\pm0.016$
0.079	$0.305\pm0.030\pm0.013$	$0.322\pm0.032\pm0.014$	$0.349\pm0.034\pm0.015$
0.090	$0.257\pm0.024\pm0.011$	$0.270\pm0.025\pm0.012$	$0.292\pm0.027\pm0.013$
0.101	$0.292\pm0.022\pm0.011$	$0.306\pm0.023\pm0.012$	$0.330\pm0.025\pm0.013$
0.113	$0.264\pm0.020\pm0.010$	$0.276\pm0.021\pm0.011$	$0.296\pm0.022\pm0.011$
0.128	$0.253\pm0.019\pm0.010$	$0.263\pm0.019\pm0.010$	$0.281\pm0.021\pm0.010$
0.144	$0.229\pm0.017\pm0.009$	$0.238\pm0.018\pm0.009$	$0.252\pm0.019\pm0.009$
0.162	$0.242\pm0.016\pm0.009$	$0.250\pm0.017\pm0.009$	$0.263\pm0.018\pm0.009$
0.182	$0.232\pm0.016\pm0.008$	$0.238\pm0.016\pm0.008$	$0.248\pm0.017\pm0.009$
0.205	$0.225\pm0.014\pm0.008$	$0.229\pm0.014\pm0.008$	$0.236\pm0.014\pm0.009$
0.230	$0.202\pm0.013\pm0.008$	$0.204\pm0.013\pm0.008$	$0.208\pm0.014\pm0.008$
0.259	$0.241\pm0.014\pm0.008$	$0.241\pm0.014\pm0.008$	$0.242\pm0.014\pm0.008$
0.292	$0.197\pm0.014\pm0.007$	$0.195\pm0.014\pm0.007$	$0.192\pm0.014\pm0.007$
0.329	$0.179\pm0.015\pm0.006$	$0.174\pm0.014\pm0.006$	$0.169\pm0.014\pm0.006$
0.370	$0.161\pm0.014\pm0.005$	$0.153\pm0.014\pm0.005$	$0.146\pm0.013\pm0.005$
0.416	$0.177\pm0.014\pm0.005$	$0.164\pm0.013\pm0.005$	$0.151\pm0.012\pm0.005$
0.468	$0.151\pm0.014\pm0.005$	$0.134\pm0.012\pm0.004$	$0.118\pm0.011\pm0.004$
0.526	$0.139\pm0.017\pm0.004$	$0.115\pm0.014\pm0.003$	$0.095\pm0.012\pm0.003$
0.592	$0.105\pm0.019\pm0.003$	$0.078\pm0.014\pm0.002$	$0.059\pm0.011\pm0.002$
0.666	$0.070\pm0.024\pm0.002$	$0.046\pm0.016\pm0.001$	$0.030\pm0.010\pm0.001$
0.749	$0.080\pm0.025\pm0.002$	$0.046\pm0.014\pm0.001$	$0.026\pm0.008\pm0.001$

Born asymmetries, and the predicted values of A_1, A_2, g_1 and g_2 for both NH_3 and ND_3 targets at E143 kinematics.

(2) The radiative corrections code was run to create tables of cross sections and asymmetries over a wide range of kinematics, fully internally radiated, to use as input to the Monte Carlo generator.

(3) The Monte Carlo routine was run for both polarized protons and deuterons alone, and for full ND_3 and NH_3 targets. This simulation included external radiation, spectrometer acceptance, resolution, multiple scattering and Fermi motion, as well as the reconstructed kinematic variables and raw asymmetries.

(4) The raw data was corrected for efficiencies, polarization, polarized nitrogen and polarized protons in ND_3 using the standard E143 procedure. Then, the data was corrected by the dilution factor (the ratio of Monte Carlo events from polarizable protons or deuterons to those from all target components), and the additive radiative correction term A_{rc} (obtained from the difference between fully radiated Monte Carlo results and the model Born asymmetry) was applied in order to generate the fully corrected values of $A_\parallel$.

(5) The ratios $(A_1+\eta A_2)/A_\parallel$ and $g_1/A_\parallel$ were used as calculated in the Born version of the radiative correction routine to find g_1 and $A_1+\eta A_2$ for our data.

This extraction method required that the Monte Carlo routine provide a detailed and realistic simulation of the data, including resolution effects which are very important in the resonance region. Therefore, we performed a series of tests to insure that the Monte Carlo simulation described the data well, and provided radiative and resolution corrections with sufficient precision compared to the statistical accuracy of our data. Without any normalization factors, the generated unpolarized counts versus W^2 agree with the data to better than 2.2% (3.4%) in the 4.5° (7°) spectrometer. The shape as a function of W^2 is in even better agreement in the region

TABLE XXII. Neutron results for g_1 at fixed Q^2 of 2, 3, and 5 $(\mathrm{GeV}/c)^2$ evaluated from g_1^p and g_1^d assuming g_1/F_1 is independent of Q^2. In addition there is a normalization uncertainty common to all data of 2.4% due to beam polarization.

x	$g_1^n(Q^2=2)\pm\mathrm{stat}\pm\mathrm{syst}$	$g_1^n(Q^2=3)\pm\mathrm{stat}\pm\mathrm{syst}$	$g_1^n(Q^2=5)\pm\mathrm{stat}\pm\mathrm{syst}$
0.031	0.085±0.378±0.081	0.091±0.408±0.088	0.100±0.448±0.097
0.035	−0.406±0.244±0.067	−0.437±0.262±0.072	−0.479±0.287±0.080
0.039	0.153±0.197±0.056	0.164±0.212±0.060	0.180±0.232±0.066
0.044	−0.415±0.166±0.044	−0.444±0.177±0.048	−0.485±0.194±0.053
0.049	−0.413±0.141±0.036	−0.440±0.151±0.039	−0.480±0.164±0.043
0.056	−0.225±0.122±0.029	−0.240±0.130±0.030	−0.261±0.142±0.033
0.063	−0.229±0.106±0.023	−0.243±0.112±0.024	−0.264±0.122±0.027
0.071	−0.180±0.094±0.019	−0.190±0.099±0.021	−0.206±0.107±0.022
0.079	−0.240±0.084±0.017	−0.252±0.088±0.018	−0.273±0.095±0.020
0.090	0.015±0.071±0.017	0.016±0.074±0.018	0.017±0.080±0.019
0.101	−0.125±0.064±0.015	−0.131±0.067±0.016	−0.141±0.072±0.017
0.113	−0.136±0.058±0.013	−0.141±0.061±0.014	−0.151±0.065±0.015
0.128	0.022±0.054±0.015	0.023±0.056±0.016	0.024±0.059±0.017
0.144	0.053±0.050±0.015	0.055±0.051±0.016	0.058±0.054±0.016
0.162	−0.095±0.047±0.012	−0.098±0.048±0.012	−0.102±0.050±0.013
0.182	0.061±0.044±0.016	0.062±0.045±0.016	0.064±0.046±0.017
0.205	−0.086±0.039±0.014	−0.087±0.039±0.014	−0.089±0.040±0.014
0.230	−0.047±0.038±0.014	−0.047±0.038±0.014	−0.047±0.038±0.014
0.259	−0.144±0.041±0.012	−0.141±0.040±0.012	−0.140±0.040±0.012
0.292	0.009±0.040±0.013	0.009±0.039±0.013	0.009±0.038±0.013
0.329	0.036±0.041±0.013	0.034±0.039±0.013	0.032±0.037±0.012
0.370	0.031±0.040±0.012	0.029±0.037±0.011	0.027±0.035±0.011
0.416	−0.067±0.040±0.010	−0.060±0.036±0.009	−0.054±0.032±0.009
0.468	−0.018±0.040±0.009	−0.015±0.034±0.008	−0.013±0.029±0.007
0.526	0.016±0.047±0.009	0.013±0.037±0.008	0.010±0.029±0.006
0.592	−0.018±0.051±0.007	−0.012±0.036±0.005	−0.009±0.026±0.004
0.666	−0.015±0.067±0.005	−0.009±0.041±0.003	−0.006±0.026±0.002
0.749	0.034±0.073±0.007	0.018±0.039±0.004	0.009±0.021±0.002

of the resonances. This provides confidence that the acceptance and resolution of the spectrometer are properly modeled. In addition, we have found that the measured and simulated count-rate differences agree well with each other. These rates were integrated over the (quasi-)elastic region ($W^2<1\ \mathrm{GeV}^2$) where model uncertainties are minimal because of reasonably good knowledge of elastic form factors and radiative corrections. The overall χ^2 for the four degrees of freedom corresponding to p(4.5°), p(7°), d(4.5°) and d(7°) is 3.85.

V. RESULTS AND COMPARISON TO THEORY

Table III gives the results for $A_\parallel^p$ and $A_\perp^p$ with the proton target for the beam energy of 29.1 GeV and for the 4.5° and 7° spectrometers, respectively, along with the total radiative corrections to each point. Tables IV–V give the results for $A_\parallel^p$ and radiative corrections for the beam energies of 16.2 and 9.7 GeV and for the two spectrometers. Tables VI–VIII give the corresponding results for the deuteron target. Since the 29 GeV data include both $A_\parallel$ and $A_\perp$, Eqs. (4) are used to determine the asymmetries A_1 and A_2, and Eqs. (2) are used to determine the structure functions g_1 and g_2 and the ratio of structure functions g_1/F_1. The NMC fit [107] was used for F_2. The SLAC global analysis [83] was used for R. While the fit to R was made to data with a limited Q^2 range and $x\geqslant 0.1$, it is consistent with recent measurements at lower x [118,119] and different Q^2 [120]. Estimated errors on these unpolarized structure functions are given in Sec. V B. The neutron spin structure function can be extracted from the deuteron and proton results in a manner similar to that used for the unpolarized structure functions. For both g_1 and g_2 we use the relation:

$$g^n(x,Q^2)=2g^d(x,Q^2)/(1-1.5\omega_D)-g^p(x,Q^2), \quad (55)$$

where ω_D is the probability that the deuteron will be in a D-state. We use $\omega_D=0.05\pm0.01$ [121] given by N-N potential calculations. No other nuclear contributions to ω_D are included. In the measured x range of this experiment, a constant ω_D is adequate, although at higher and lower x more refined corrections become important [122–124]. The neutron asymmetries can then be calculated using Eqs. (4).

A. A_1 and g_1

For beam energies of 16.2 and 9.7 GeV there are no $A_\perp$ data available. We have assumed that $g_2(x,Q^2)$ is given by either g_2^{WW} or $g_2=0$, both of which are consistent with our g_2 data at 29 GeV. These different assumptions lead to very similar results. We have then determined A_1 and g_1 using Eq. (5).

Tables IX and X show the values of g_1/F_1 and A_1 for deep-inelastic scattering ($W^2 \geq 4\ \mathrm{GeV}^2$) for all three beam energies and both spectrometers using $g_2=g_2^{WW}$ for the 16.2 and 9.7 GeV data and $A_\parallel$ and $A_\perp$ for the 29.1 GeV data. Figures 13 and 14 show g_1/F_1 for proton and deuteron as functions of Q^2 averaged into 8 x bins. Data from EMC [6], SMC [7,9,14], SLAC E80 [2], and SLAC E130 [3] are also included. The results are consistent with g_1/F_1 and A_1 being independent of Q^2 for $Q^2 \geq 1\ (\mathrm{GeV}/c)^2$. We fit all the deuteron and proton data (including the SMC data at $Q^2 \leq 1$), with the empirical parametrization $ax^\alpha(1+bx+cx^2)[1+Cf(Q^2)]$. The coefficients of the fit are shown in Table XI, and the fits are shown in Figs. 13 and 14. We chose three forms for $f(Q^2)$ shown in column 3 of the table. They are

$f(Q^2)=0$: no Q^2 dependence,

$f(Q^2)=1/Q^2$: higher twist behavior,

$f(Q^2)=\ln(1/Q^2)$: pQCD behavior.

The minimum Q^2 of the fits is shown in column 2 and is either 0.3 or 1.0 $(\mathrm{GeV}/c)^2$. For the proton data, the χ^2 per DF is less than unity for all the fits except fit I, indicating that there is Q^2 dependence for $Q^2 \leq 1\ (\mathrm{GeV}/c)^2$. Fit II indicates that there is no need for any Q^2-dependent term for $Q^2 \geq 1\ (\mathrm{GeV}/c)^2$, which is our cut-off for deep-inelastic scattering. For the deuteron data, the fits are not as good, but still have a confidence level of about 10%. Fit V, which has $Q^2_{min}=0.3\ (\mathrm{GeV}/c)^2$, is used to evaluate g_2^{WW} and to iterate the radiative corrections described above.

Also shown in Figs. 13 and 14 are the results from the E154 [125] leading order pQCD evolution fit to world data including preliminary results from this experiment. It is in good agreement with the data, including the data for $Q^2 \leq 1\ (\mathrm{GeV}/c)^2$ which was not used in the fit. However, for the proton it does have an exaggerated Q^2 dependence at the highest x. Since g_1/F_1 and A_1 are both consistent with being independent of Q^2 for $Q^2 \geq 1\ (\mathrm{GeV}/c)^2$, we choose to combine our data at fixed x by averaging them over all measured values for $Q^2 \geq 1\ (\mathrm{GeV}/c)^2$. Tables XII and XIII and Fig. 15 show these averaged values as a function of x. The band at the bottom of Fig. 15 represents the size of the systematic errors. Also shown are results from other experiments [6,7,9,14] averaged in a similar way. The various experiments are in agreement with each other. Results for g_1/F_1 and A_1 are similar at low x and diverge slightly at high x. For the proton, both g_1/F_1 and A_1 are small and positive at low x and rise steeply toward unity as $x \to 1$. For the deuteron, both g_1/F_1 and A_1 are close to zero at low x and increase slowly with increasing x. For the neutron, both g_1/F_1 and A_1 are negative over most of the x region, showing almost no indication of becoming positive at high x as expected from earlier predictions [27].

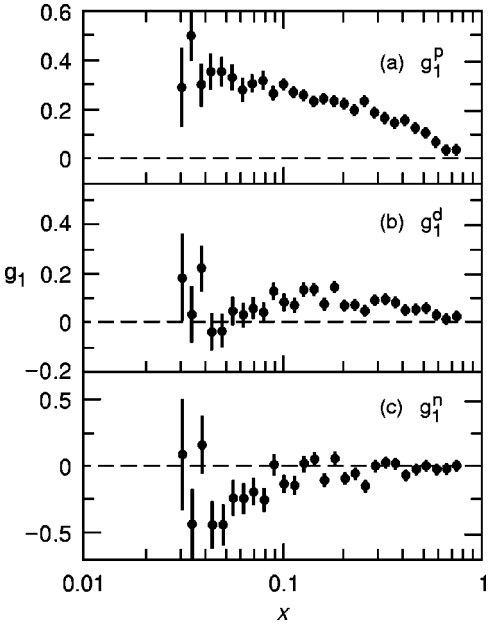

FIG. 17. $g_1(x,Q^2)$ evaluated at $Q^2=3\ (\mathrm{GeV}/c)^2$ (assuming g_1/F_1 is independent of Q^2) as a function of x.

Table XIV shows g_1 at the averaged measured value of Q^2 obtained from the average value of g_1/F_1. The quantity g_1^n was obtained using Eq. (55). Figure 16 shows xg_1 as a function of $\log x$. The area between the data and zero is the integral forming the sum rules $\int_0^1 g(x)dx = \int_{-\infty}^0 xg(x)d\ \ln x$.

B. Systematic errors

The systematic errors were calculated for g_1/F_1, A_1, and g_1. Only the systematic error due to $A^\parallel$ was considered since the systematic errors due to $A_\perp$ were negligible compared to the statistical errors. Some of the errors were multiplicative and independent of x while others were x-dependent. The errors due to multiplicative factors (beam and target polarization) are shown in Table XV. The errors on g_1 and g_1/F_1 from these normalizations were obtained using a smoothed fit to g_1/F_1. The breakdown of the major sources of error for a sample of our x bins is shown in Tables XVI–XIX for deuteron and proton targets for both g_1 and g_1/F_1. The radiative correction error dominated at low x. The errors due to multiplicative factors were only significant when either g_1 or g_1/F_1 were large at middle and high x, respectively.
Multiplicative systematic errors:

(1) The error of the beam polarization P_B was estimated to be 0.024 (relative). See Section III C 5.

(2) The error of the target polarization P_T had a relative systematic error of 0.025 for protons and 0.04 for deuterons. The error was assumed to be 100% correlated between runs, since the systematic error was obtained from the spread of the thermal equilibrium measurement results, each of which provided the calibration constants for large groups of runs. See Sec. III D 2.

(3) The proton in nitrogen correction [see Eq. (41)] contributed with a 0.004 relative systematic error since the cor-

TABLE XXIII. $\int_{.03}^{.8} g_1(x)dx$ at different Q^2 by different methods. The first error is statistical and the second is systematic. There are additional normalization uncertainties shown in Table XV.

	Method	$Q^2=2(\mathrm{GeV}/c)^2$	$Q^2=3(\mathrm{GeV}/c)^2$	$Q^2=5(\mathrm{GeV}/c)^2$
Deuteron	g_1/F_1	$0.050\pm0.004\pm0.003$	$0.046\pm0.003\pm0.003$	$0.043\pm0.003\pm0.002$
Deuteron	A_1	$0.047\pm0.005\pm0.003$	$0.044\pm0.004\pm0.003$	$0.043\pm0.003\pm0.002$
Proton	g_1/F_1	$0.129\pm0.004\pm0.006$	$0.121\pm0.003\pm0.006$	$0.117\pm0.003\pm0.006$
Proton	A_1	$0.120\pm0.004\pm0.006$	$0.116\pm0.003\pm0.006$	$0.116\pm0.003\pm0.006$
Neutron	g_1/F_1	$-0.022\pm0.011\pm0.006$	$-0.023\pm0.008\pm0.006$	$-0.025\pm0.007\pm0.006$
Neutron	A_1	$-0.019\pm0.013\pm0.005$	$-0.021\pm0.009\pm0.005$	$-0.023\pm0.007\pm0.005$

rection C_1 was always around 0.02, while the relative error on C_1 was estimated to be 0.2.

Systematic errors dependent on x:

(1) The error of the dilution factor f came from several sources. The component dependent on our experimental setup (the amount of ammonia in the target cell) was known to 4% for both targets. The relative error from the cross-section ratio σ_n/σ_p was 1% [108]. It was one of the dominant errors for the NH_3 target and did not contribute for the ND_3 target. The ratio of nuclear to deuterium cross sections, the EMC effect, is known to 1.5% relative and was another large error source. It has a 1% overall normalization and another 1% of uncorrelated error [106]. The small mass of the NMR coil was known to 20% but did not contribute significantly to the overall error. This leads to an average error on f of 2% for NH_3 and 1.5% for ND_3.

(2) The nitrogen correction was applied via two factors, C_1 and C_2 [see Eq. (44)]. The error on C_1 was neglected since this value was very small and stable. The factor C_2 (ND_3 only) contained the proton asymmetry and was calculated for each x bin using our measured proton asymmetry and its error.

(3) The systematic error on the radiative corrections was calculated for each x bin by varying several classes of input models. See Section IV B 6 for details. It is shown in Tables XVI-XIX for typical values of x at 29 GeV beam energy for g_1 and g_1/F_1.

(4) The error due to the structure function $R(x,Q^2)$ contributed to g_1/F_1 and g_1 quite differently due to the relationship between F_1 and F_2. For g_1 the effect of R is negligible whereas for g_1/F_1 it is one of the significant errors. Its systematic error was taken from the SLAC global analysis [83] and ranged from 3% to about 7.5%. While this fit to R was made to data with a limited Q^2 range and $x\geqslant 0.1$, it is consistent with recent measurements at lower x [118,119] and different Q^2 [120].

(5) The error in the structure function F_2 was obtained from the NMC fit [107]. The error returned from the fit was taken as completely correlated point-to-point.

(6) Pion and charge-symmetric backgrounds were treated as statistical errors from the measurement with spectrometers set at opposite polarity. No systematic error was assigned to the model of charge symmetry.

When averaging g_1/F_1 over spectrometers and beam energies, the weight of each data point included statistical and point-to-point uncorrelated systematic errors. For the systematic error of the neutron structure function g_1^n as well as of the difference $g_1^p-g_1^n$, the beam polarization error and the dilution factor errors due to the unpolarized cross sections were assumed to be 100% correlated, while the other errors were assumed to be uncorrelated.

The systematic error on the integral was calculated using the separated correlated and uncorrelated systematic errors. The systematic errors of the low-x and high-x extrapolations were added together with the systematic error for the data region. The sum was then quadratically combined with the fit errors for the low- and high-x extrapolations to yield the total systematic error on the integral.

C. Integrals

The Ellis-Jaffe [Eq. (21)] and Bjorken [Eq. (20)] sum rules involve integrals over all values of x at a fixed Q^2. The experimental results do not cover all x at any single Q^2. In the measured region of x we must either interpolate or extrapolate our results from the measured Q^2 to some fixed Q_o^2. In the regions of x above and below the measured region, we use model-dependent extrapolations.

1. Measured region

Several methods have been used to determine g_1 at fixed Q_0^2.

TABLE XXIV. Systematic errors on the measured integral at $Q^2=3\,(\mathrm{GeV}/c)^2$.

Source	Deuteron	Proton	Neutron	p-n
F_2	0.001	0.003	0.001	0.003
R	0.000	0.001	0.000	0.001
A_{rc}	0.001	0.002	0.003	0.005
f	0.001	0.002	0.001	0.003
P_B	0.001	0.003	0.001	0.003
P_T	0.002	0.003	0.005	0.007
Total	0.003	0.006	0.006	0.010

TABLE XXV. Estimates of $\int_0^{0.03} g_1(x,Q^2)dx$ at $Q^2=3\ (\mathrm{GeV}/c)^2$ using various hypotheses. Columns 3–5 have the Regge form $g_1=\beta x^\alpha$ fitted to $g_1(x,Q^2)$ at the Q^2 shown in the second row, with α shown in the first row, in the range $0.03\leqslant x\leqslant x_{cut}$ shown in column 2. Column 6 has a fit of the form $\ln(1/x)$. Column 7 has results of global fit II of Table XI. The last column is the integral of the SMC data with flat Regge extrapolation ($\alpha=0$) below $x=0.003$.

	x_{cut}	$\alpha=0$ $Q^2=3$	$\alpha=0$ $Q^2=1$	$\alpha=0.5$ $Q^2=3$	$\ln(1/x)$ $Q^2=3$	global II $Q^2=3$	SMC $Q^2=3$
Deuteron	0.10	0.002	0.002	0.001	0.003	0.001	-0.005 ± 0.003
Proton	0.10	0.009	0.010	0.004	0.015	0.018	0.014 ± 0.003
Neutron	0.10	-0.005	-0.006	-0.002	-0.009	-0.016	-0.025 ± 0.007
p-n	0.10	0.014	0.016	0.006	0.024	0.034	0.039 ± 0.009
Deuteron	0.06	0.001	0.001	0.000	0.002		
Proton	.06	0.010	0.011	0.005	0.015		
Neutron	.06	-0.008	-0.009	-0.004	-0.012		
p-n	.06	0.018	0.020	0.010	0.026		

(1) Assume g_1/F_1 is independent of Q^2 and determine g_1 from $g_1(x,Q_o^2)=g_1/F_1\times F_1(x,Q_o^2)$.
(2) Assume A_1 is independent of Q^2 and determine g_1 from $[g_1(x,Q_o^2)=A_1(x)\times F_1(x,Q_0^2)+\gamma_o^2 g_2^{WW}(x,Q^2)]$.
(3) Fit the data to a functional form which has semi-empirical dependencies on x and Q^2 such as the fits described above.
(4) Do a pQCD fit to determine the quark and gluon distributions and then calculate the change in g_1 going from the measured to the desired kinematics.

In this paper we will pursue the first two options with emphasis on the first. We note that the pQCD fits indicated in Figs. 13 and 14 show little Q^2 dependence (compared to the errors of the experiments) for g_1/F_1 at $x\leqslant0.5$ in the relevant Q^2 range. For $x\geqslant0.6$, theoretical papers often use approximations in defining the relationship between F_2 and F_1 and sometimes use pQCD fits to F_2 instead of empirical fits to the data. At $x=0.75$ typical pQCD fits [59,125,126] show g_1^p/F_1^p differing by 30–50% between the measured $Q^2\sim9.5\ (\mathrm{GeV}/c)^2$ and $Q^2=3(\mathrm{GeV}/c)^2$, but these predictions are questionable due to the assumptions used.

Tables XX–XXII list g_1 as a function of x at fixed Q^2 values of 2, 3, and 5 $(\mathrm{GeV}/c)^2$ for proton, deuteron, and neutron. These results were evaluated by method 1 (g_1/F_1 independent of Q^2). Figure 17 shows the corresponding method 1 results for g_1 at $Q^2=3\ (\mathrm{GeV}/c)^2$. Results for $\int_{0.03}^{0.8} g_1(x)dx$ using methods 1 and 2 (A_1 independent of Q^2, g_2^{WW}) at the same three values of Q^2 are given in Table XXIII. Method 1 yields slightly larger results in magnitude

TABLE XXVI. Integral of g_1 in the measured region as well as extrapolations to high and low x as described in the text. Slight differences between the measured targets and derived targets, n and p-n, are due to correlations among systematic errors. The structure function g_1 was calculated at fixed Q^2 assuming g_1/F_1 independent of Q^2.

	$\langle Q^2\rangle$ $(\mathrm{GeV}/c)^2$	Measured $\int_{.03}^{.8} g_1$	High x $\int_{.8}^{1} g_1$	Low x $\int_{0}^{.03} g_1$	Total $\int_0^1 g_1$
Deuteron	2	$0.050\pm0.004\pm0.003$	0.000 ± 0.001	0.001 ± 0.006	$0.051\pm0.004\pm0.006$
Proton	2	$0.129\pm0.004\pm0.006$	0.001 ± 0.001	0.011 ± 0.007	$0.140\pm0.004\pm0.010$
Neutron	2	$-0.022\pm0.011\pm0.006$	0.001 ± 0.001	-0.009 ± 0.016	$-0.030\pm0.011\pm0.017$
p-n	2	$0.149\pm0.012\pm0.011$	0.001 ± 0.001	0.020 ± 0.019	$0.169\pm0.012\pm0.022$
Deuteron	3	$0.046\pm0.003\pm0.003$	0.000 ± 0.001	0.001 ± 0.006	$0.047\pm0.003\pm0.006$
Proton	3	$0.121\pm0.003\pm0.006$	0.001 ± 0.001	0.011 ± 0.007	$0.133\pm0.003\pm0.009$
Neutron	3	$-0.023\pm0.008\pm0.006$	0.001 ± 0.001	-0.010 ± 0.015	$-0.032\pm0.008\pm0.016$
p-n	3	$0.143\pm0.009\pm0.010$	0.001 ± 0.001	0.021 ± 0.018	$0.164\pm0.009\pm0.021$
Deuteron	5	$0.043\pm0.003\pm0.002$	0.000 ± 0.001	0.001 ± 0.006	$0.044\pm0.003\pm0.006$
Proton	5	$0.117\pm0.003\pm0.006$	0.001 ± 0.001	0.012 ± 0.008	$0.129\pm0.003\pm0.010$
Neutron	5	$-0.025\pm0.007\pm0.006$	0.001 ± 0.001	-0.010 ± 0.015	$-0.034\pm0.007\pm0.016$
p-n	5	$0.141\pm0.008\pm0.010$	0.001 ± 0.001	0.022 ± 0.017	$0.164\pm0.008\pm0.020$

TABLE XXVII. Comparison of integrals from this experiment and E142 [10] and SMC [7,9]. Note that the SMC and E143 results used g_1/F_1 independent of Q^2 and E142 used A_1 independent of Q^2 to evaluate g_1 at fixed Q^2 from measurements at different Q^2, and that the different experiments had different mean Q^2.

	Q^2	Method	x range	This experiment	← Other experiments →	
Proton	5	g_1/F_1	$0.03 \leqslant x \leqslant 0.7$	0.115 ± 0.006	SMC	0.128 ± 0.006
			$0 \leqslant x \leqslant 1$	0.129 ± 0.010		0.140 ± 0.011
Deuteron	5	g_1/F_1	$0.03 \leqslant x \leqslant 0.7$	0.041 ± 0.004	SMC	0.043 ± 0.007
			$0 \leqslant x \leqslant 1$	0.044 ± 0.007		0.039 ± 0.008
Neutron	2	A_1	$0.03 \leqslant x \leqslant 0.6$	-0.021 ± 0.009	E142	-0.028 ± 0.008
			$0 \leqslant x \leqslant 1$	-0.030 ± 0.020		-0.031 ± 0.011

than method 2, but the difference is smaller than the total error for all targets at fixed $Q^2 \geqslant 3\,(\mathrm{GeV}/c)^2$. The components of the systematic error on the integral are shown in Table XXIV. The correlated systematic errors due to beam and target polarization and F_2 dominate. The radiative correction errors tend to be anti-correlated between low and high x and thus partly cancel in the integral.

2. Low x

The evaluation of $\int_0^{0.03} g_1(x,Q_o^2)dx$ can be done by several methods.

(1) Using Regge trajectory-type behavior, $g_1 = x^\alpha g_1^0$ at fixed Q^2 and low x. The difference $g_1^p - g_1^n$ has isospin 1 and only one Regge trajectory contributes. The value of α is in the general range $0.5 \geqslant \alpha \geqslant 0$ [127–129]. For the individual proton and deuteron targets there may be more than one pole contributing [127]. There also may be even more complex behavior of the singlet term.
(2) Using SMC data from $0.003 \leqslant x \leqslant 0.03$ and Regge extrapolations below $x = 0.003$.
(3) Using the form $g_1 \propto \ln(1/x)$ [129,130].
(4) Using the parametrization II from Table XI (the form is Regge inspired at low x).
(5) Using pQCD fits.

The Regge method requires a choice of x range to determine the pole parameter and a choice of other possible Regge trajectories. In addition, if g_1 has Regge behavior at a given Q^2, it will not have Regge behavior at other Q^2 since g_1 evolves with Q^2 differently at different values of x. Table XXV shows the results of various options, including using the Regge form at $Q^2 = 1$ and $3\,(\mathrm{GeV}/c)^2$. Constraining $\alpha = 0$ gives good fits at both $Q^2 = 1$ and $3\,(\mathrm{GeV}/c)^2$. However, requiring $\alpha = 0.5$ gives a rather poor fit ($\chi^2/df \approx 2$) for the proton. We take the average of the four fits in Table XXV with $\alpha = 0$ as the central value of the low x extrapolation. The error encompasses all the other models indicated. These averages are shown in Table XXVI. The values of the integral for proton, deuteron, neutron, and proton-neutron (p-n) may not add up exactly due to the non-linearity of the fits.

TABLE XXVIII. Experimental value of Γ_1 compared to the Ellis-Jaffe sum rule and Bjorken sum rule (p-n). For the theoretical input we take $\alpha_s(M_Z) = 0.118 \pm 0.003$ and $3F - D = 0.58$ with uncertainties of either 0.032 (small) or 0.120 (large). The Ellis-Jaffe sum is evaluated with both the invariant and Q^2-dependent pQCD singlet corrections. The Bjorken sum rule depends only on the non-singlet correction.

	$\langle Q^2 \rangle$ $(\mathrm{GeV}/c)^2$	Γ_1^{exp}	Γ_1^{theory} invariant	Γ_1^{theory} Q^2-dependent	Error (small)	Error (large)
Deuteron	2	0.051 ± 0.008	0.070	0.065	± 0.004	± 0.014
Proton	2	0.140 ± 0.010	0.161	0.156	± 0.005	± 0.016
Neutron	2	-0.030 ± 0.020	-0.010	-0.015	± 0.005	± 0.016
p-n	2	0.169 ± 0.025	0.171	0.171	± 0.006	± 0.006
Deuteron	3	0.047 ± 0.007	0.071	0.066	± 0.004	± 0.014
Proton	3	0.133 ± 0.010	0.165	0.160	± 0.005	± 0.016
Neutron	3	-0.032 ± 0.018	-0.012	-0.017	± 0.004	± 0.016
p-n	3	0.164 ± 0.023	0.177	0.177	± 0.004	± 0.004
Deuteron	5	0.044 ± 0.007	0.072	0.068	± 0.004	± 0.015
Proton	5	0.129 ± 0.010	0.169	0.164	± 0.005	± 0.016
Neutron	5	-0.034 ± 0.017	-0.014	-0.018	± 0.004	± 0.016
p-n	5	0.164 ± 0.021	0.182	0.182	± 0.003	± 0.003

TABLE XXIX. The evaluated quark spins using both the ''invariant'' and Q^2-dependent pQCD singlet coefficients, with an assumed error on F/D of 0.016. If the more conservative estimate of $\delta(3F-D)=0.12$ is used, the only change is to the error on Δs which is shown in the last column.

	Method	$\Sigma=a_o$	Δu	Δd	Δs	Conservative $\delta\Delta s$
Deuterium	invariant	0.35 ± 0.07	0.84 ± 0.02	-0.42 ± 0.02	-0.08 ± 0.03	±0.05
Proton	invariant	0.29 ± 0.09	0.83 ± 0.03	-0.43 ± 0.03	-0.10 ± 0.03	±0.06
Deuterium	$Q^2=3$ (GeV/c)^2	0.37 ± 0.08	0.85 ± 0.03	-0.41 ± 0.03	-0.07 ± 0.03	±0.06
Proton	$Q^2=3$ (GeV/c)^2	0.32 ± 0.10	0.83 ± 0.03	-0.43 ± 0.03	-0.09 ± 0.04	±0.06

Recent results from SLAC [11] indicate that g_1^n may be behaving as $\sim x^{-0.8}$ at low x. If the proton behaves in a similar way, then the above extrapolations would be open to question.

3. High x

The extrapolation to high x was done by two methods: (1) assuming $g_1 \propto (1-x)^3$ [131] and fitting to the four highest x bins and (2) assuming $A_1^p=0.75(19-16F_2^n/F_2^p)/15$ and $A_1^n=0.75(2-3F_2^n/F_2^p)/(5F_2^n/F_2^p)$ [27]. For both g_1^d and g_1^p, both methods gave almost identical values of $\int_{0.8}^1 g_1(x)dx$. For the deuteron the value is 0.000 and for the proton 0.001. We assign an error of ±0.001 in both cases. For the neutron the value of the integral is 0.001 ± 0.001 where rounding errors account for inexact match with proton and deuteron results. The small value of the integral is mostly due to the small value of F_1 and not the properties of the individual models. The average values are shown in Table XXVI.

4. Total integral

Table XXVI shows Γ_1, the total integral from $x=0$ to 1, in the last column for proton, deuteron, neutron, and the difference proton-neutron. The experimentally measured portion of the integral makes the largest contribution to $\delta\Gamma_1$ with the low x extrapolation error a close second. The correlation between the measurement errors at low x and the extrapolation errors is small compared to the model dependence of the extrapolation.

The integrals from this experiment, E142 [10], and SMC [7,9,14] are compared in Table XXVII at Q^2 values reported by the other experiments. Comparisons are made for the full range in x of 0 to 1, as well as for the common measured x range between experiments. For each comparison, we evaluated the integral using the same assumptions about Q^2 dependence that the other experimenters used. (SMC results were calculated by us from their tables.) In the experimental range there is good agreement between this experiment and the other results. Γ_1 for each experiment, as shown in Table XXVII, are also in excellent agreement with the caveat that different x ranges were measured and different extrapolations used in the unmeasured region.

5. Ellis-Jaffe sum rule

Ellis-Jaffe sum rule predictions for the integrals [Eq. (21)] are shown at three values of Q^2 in Table XXVIII. We use $\alpha_s(M_Z)=0.118\pm0.003$ [26], three active flavors, and $3F-D=0.58$ [27] with uncertainties of either 0.03 (small) [27] or 0.12 (large) [20]. This larger error, as discussed in Section II B 1, is likely to be an overestimate. For the Ellis-Jaffe sum rule, the values for both the ''invariant'' and Q^2-dependent singlet pQCD corrections [see Eq. (17)] are given. They differ by an amount which is larger than the theoretical error due to α_s. In the case of the deuteron, the experimental errors are comparable to the theoretical difference. The measured values of Γ_1^p and Γ_1^d are shown in the table along with the derived value of Γ_1^n. Using the small errors on $3F-D$ and the ''invariant'' singlet term the Ellis-Jaffe sum rules are violated by 0.023 ± 0.007 (deuteron) and 0.032 ± 0.012 (proton). A violation implies that there could be a significant SU(3) symmetry breaking effect or that there is strange and/or gluon spin contributing to the proton spin. If we consider the large $3F-D$ errors (larger error due to possible symmetry breaking) combined with the Q^2-dependent singlet term, the deviations from the sum rule reduce to 0.018 ± 0.015 (deuteron) and 0.027 ± 0.019 (proton).

6. Bjorken sum rule

The Bjorken sum rule integral [Eq. (20)] is given in Table XXVIII for three different values of Q^2. The theoretical

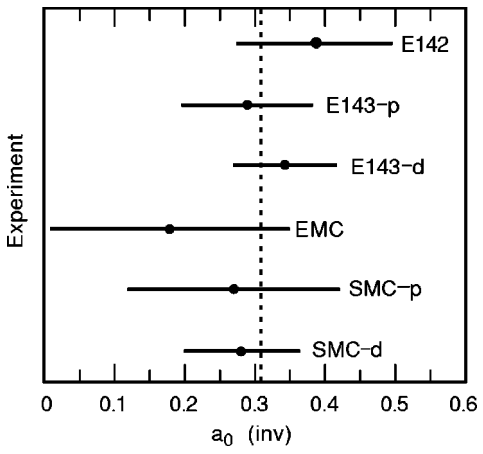

FIG. 18. Measured singlet matrix elements a_0^{inv} from this experiment, E142 [10], SMC [7,9], and EMC/E80/E130 combined [6]. These results were calculated from the published first moments of g_1 using up-to-date ''invariant'' singlet pQCD corrections and $\delta(3F-D)=0.032$. The dashed curve indicates the world average of 0.31 ± 0.04.

TABLE XXX. Results for A_2, g_2 and $\overline{g_2}$ for the proton measured in the 4.5° and 7.0° spectrometers at the indicated average values of x and Q^2 and beam energy of 29.1 GeV. The highest x bin shown is in the resonance region defined by missing mass $W^2<4$ GeV^2.

x interval	$\langle x\rangle$	$\langle$Q2$\rangle$ (GeV/c)^2	$A_2^p \pm$stat$\pm$syst	$g_2^p \pm$stat$\pm$syst	$\overline{g_2^p} \pm$stat$\pm$syst
0.029–0.047	0.038	1.49	$0.016\pm0.018\pm0.006$	$0.489\pm0.980\pm0.332$	$0.223\pm0.983\pm0.332$
0.047–0.075	0.060	2.01	$0.025\pm0.014\pm0.005$	$0.397\pm0.374\pm0.138$	$0.223\pm0.375\pm0.138$
0.075–0.120	0.095	2.60	$0.004\pm0.015\pm0.006$	$-0.236\pm0.203\pm0.074$	$-0.295\pm0.204\pm0.074$
0.120–0.193	0.152	3.21	$0.021\pm0.021\pm0.008$	$-0.136\pm0.125\pm0.049$	$-0.127\pm0.127\pm0.049$
0.193–0.310	0.241	3.77	$0.091\pm0.032\pm0.011$	$-0.046\pm0.079\pm0.026$	$0.027\pm0.080\pm0.026$
0.310–0.498	0.379	4.22	$0.135\pm0.060\pm0.014$	$-0.050\pm0.048\pm0.009$	$0.051\pm0.050\pm0.009$
0.498–0.799	0.595	4.55	$0.061\pm0.154\pm0.028$	$-0.037\pm0.020\pm0.004$	$-0.005\pm0.022\pm0.004$
0.075–0.120	0.101	3.76	$0.025\pm0.025\pm0.007$	$0.060\pm0.366\pm0.116$	$0.000\pm0.368\pm0.116$
0.120–0.193	0.155	4.97	$0.048\pm0.019\pm0.007$	$0.171\pm0.141\pm0.049$	$0.198\pm0.142\pm0.049$
0.193–0.310	0.243	6.37	$0.053\pm0.022\pm0.007$	$-0.068\pm0.070\pm0.021$	$0.023\pm0.071\pm0.021$
0.310–0.498	0.382	7.76	$0.077\pm0.035\pm0.008$	$-0.039\pm0.034\pm0.007$	$0.043\pm0.035\pm0.007$
0.498–0.799	0.584	8.85	$0.106\pm0.083\pm0.016$	$-0.022\pm0.011\pm0.002$	$0.001\pm0.012\pm0.002$

value involves only non-singlet pQCD corrections and is thus independent of ambiguities associated with the singlet corrections (invariant or Q^2-dependent). Theoretical errors depend only on the uncertainty in α_s. The measured values are from this experiment only and the errors include all correlations. The experimental errors are considerably larger than the theoretical errors. Experiment and theory agree within one standard deviation.

A more precise result can be obtained by combining all the experiments [7,9,6,11] which published a value of the integrals. SLAC experiment E154 [11] on the neutron was not included because they did not publish an integral of their data alone. We consistently used the method with g_1/F_1 independent of Q^2 to evolve the results to constant Q^2. In all experiments, the low-x extrapolation errors were limited to g_1 being constant or approaching zero as $x\to0$. At $Q^2=5$ (GeV/c)^2, the combined results are $\Gamma_1^{Bj}=0.170\pm0.012$, $\Gamma_1^p=0.130\pm0.006$, and $\Gamma_1^n=-0.040\pm0.008$ with a very small χ^2 per DF. Γ_1^{Bj} is one standard deviation from the theoretical value of 0.182 determined from Eq. (20) with $\alpha_s(M_Z)=0.118$. The addition of higher twist and other effects described below make the agreement even better. If we assume the Bjorken sum rule is true and solve Eq. (20) for α_s we obtain $\alpha_s(M_z)=0.123^{+0.010}_{-0.006}$.

D. Quark polarization

We used Eqs. (14)–(15) to extract our measured value of a_0 from the proton and deuteron first moments. Then using Eq. (20) (with $\Delta G=0$), we extracted the individual polariza-

TABLE XXXI. Results for A_2, g_2 and $\overline{g_2}$ for the deuteron measured in the 4.5° and 7° spectrometers at the indicated average values of x and Q^2 and beam energy of 29.1 GeV. The highest x bin shown is in the resonance region defined by missing mass $W^2<4$ GeV^2.

x interval	$\langle x\rangle$	$\langle Q^2\rangle$ (GeV/c)^2	$A_2^d \pm$stat$\pm$syst	$g_2^d \pm$stat$\pm$syst	$\overline{g_2^d} \pm$stat$\pm$syst
0.029–0.047	0.038	1.49	$0.070\pm0.045\pm0.010$	$3.426\pm2.157\pm0.575$	$3.275\pm2.161\pm0.575$
0.047–0.075	0.060	2.01	$-0.025\pm0.028\pm0.006$	$-0.655\pm0.707\pm0.157$	$-0.799\pm0.709\pm0.157$
0.075–0.120	0.095	2.60	$0.008\pm0.032\pm0.010$	$0.008\pm0.390\pm0.118$	$-0.048\pm0.392\pm0.118$
0.120–0.193	0.152	3.21	$0.005\pm0.045\pm0.016$	$-0.118\pm0.243\pm0.080$	$-0.095\pm0.245\pm0.080$
0.193–0.310	0.241	3.77	$0.078\pm0.072\pm0.020$	$0.127\pm0.154\pm0.041$	$0.134\pm0.156\pm0.041$
0.310–0.498	0.378	4.22	$-0.079\pm0.144\pm0.017$	$-0.127\pm0.094\pm0.010$	$-0.095\pm0.096\pm0.010$
0.498–0.799	0.595	4.56	$0.327\pm0.390\pm0.044$	$0.037\pm0.039\pm0.004$	$0.027\pm0.041\pm0.004$
0.075–0.120	0.101	3.77	$0.024\pm0.046\pm0.009$	$0.172\pm0.621\pm0.133$	$0.084\pm0.624\pm0.133$
0.120–0.193	0.154	4.97	$-0.007\pm0.036\pm0.011$	$-0.109\pm0.235\pm0.076$	$-0.086\pm0.237\pm0.076$
0.193–0.310	0.242	6.37	$-0.043\pm0.043\pm0.015$	$-0.133\pm0.116\pm0.041$	$-0.117\pm0.118\pm0.041$
0.310–0.498	0.381	7.76	$0.000\pm0.073\pm0.014$	$-0.042\pm0.056\pm0.011$	$-0.006\pm0.057\pm0.011$
0.498–0.799	0.584	8.86	$0.235\pm0.183\pm0.030$	$0.000\pm0.018\pm0.003$	$0.011\pm0.019\pm0.003$

TABLE XXXII. Results for A_2, g_2 and $\overline{g_2}$ for the neutron measured in the 4.5° and 7° spectrometers at the indicated average values of x and Q^2 and beam energy of 29.1 GeV. The highest x bin shown is in the resonance region defined by missing mass $W^2<4\ \mathrm{GeV}^2$.

x interval	$\langle x\rangle$	$\langle Q^2\rangle$ $(\mathrm{GeV}/c)^2$	$A_2^n \pm \mathrm{stat} \pm \mathrm{syst}$	$g_2^n \pm \mathrm{stat} \pm \mathrm{syst}$	$\overline{g_2^n} \pm \mathrm{stat} \pm \mathrm{syst}$
0.029–0.047	0.038	1.49	$0.143 \pm 0.105 \pm 0.023$	$7.024 \pm 4.777 \pm 1.288$	$6.963 \pm 4.787 \pm 1.288$
0.047–0.075	0.060	2.01	$-0.085 \pm 0.065 \pm 0.015$	$-1.811 \pm 1.574 \pm 0.367$	$-1.948 \pm 1.579 \pm 0.367$
0.075–0.120	0.095	2.60	$0.013 \pm 0.076 \pm 0.025$	$0.254 \pm 0.868 \pm 0.266$	$0.192 \pm 0.872 \pm 0.266$
0.120–0.193	0.152	3.21	$-0.013 \pm 0.114 \pm 0.040$	$-0.118 \pm 0.541 \pm 0.180$	$-0.079 \pm 0.545 \pm 0.180$
0.193–0.310	0.241	3.77	$0.067 \pm 0.192 \pm 0.056$	$0.320 \pm 0.342 \pm 0.093$	$0.263 \pm 0.347 \pm 0.093$
0.310–0.498	0.378	4.22	$-0.433 \pm 0.419 \pm 0.058$	$-0.225 \pm 0.209 \pm 0.024$	$-0.256 \pm 0.214 \pm 0.024$
0.498–0.799	0.595	4.56	$0.926 \pm 1.302 \pm 0.200$	$0.116 \pm 0.086 \pm 0.010$	$0.064 \pm 0.091 \pm 0.010$
0.075–0.120	0.101	3.77	$0.028 \pm 0.113 \pm 0.024$	$0.315 \pm 1.392 \pm 0.312$	$0.184 \pm 1.399 \pm 0.312$
0.120–0.193	0.154	4.97	$-0.078 \pm 0.091 \pm 0.029$	$-0.407 \pm 0.528 \pm 0..172$	$-0.384 \pm 0.533 \pm 0.172$
0.193–0.310	0.242	6.37	$-0.195 \pm 0.118 \pm 0.041$	$-0.219 \pm 0.261 \pm 0.091$	$-0.276 \pm 0.265 \pm 0.091$
0.310–0.498	0.381	7.76	$-0.131 \pm 0.218 \pm 0.045$	$-0.052 \pm 0.125 \pm 0.025$	$-0.057 \pm 0.128 \pm 0.025$
0.498–0.799	0.584	8.86	$0.544 \pm 0.627 \pm 0.120$	$0.021 \pm 0.041 \pm 0.006$	$0.023 \pm 0.042 \pm 0.006$

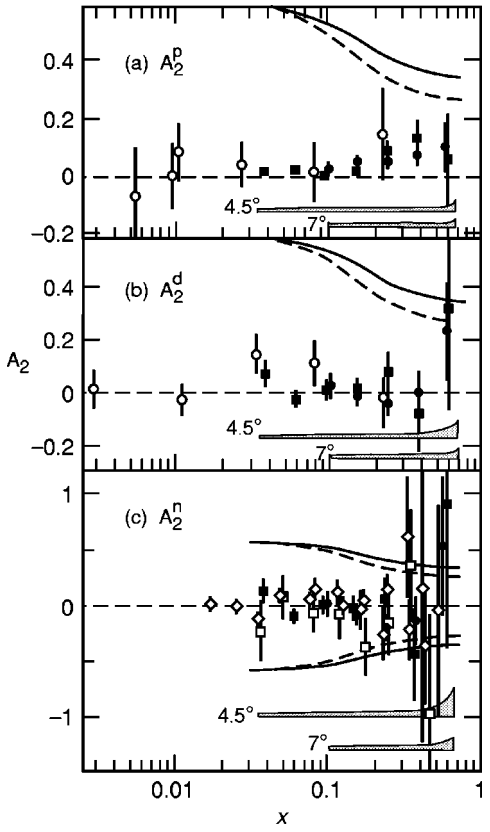

FIG. 19. The results for $A_2(x,Q^2)$ as a function of x for this experiment (solid squares for 4.5°, solid circles for 7°). Also shown are SMC (open circles) [14], E142 (open square) [10], and E154 (diamond) [15]. The solid and dashed curves correspond to the positivity constraint at 4.5° and 7° kinematics, respectively. Overlapping data have been shifted slightly in x to make errors clearly visible. The bands indicate systematic errors for the two E143 data sets.

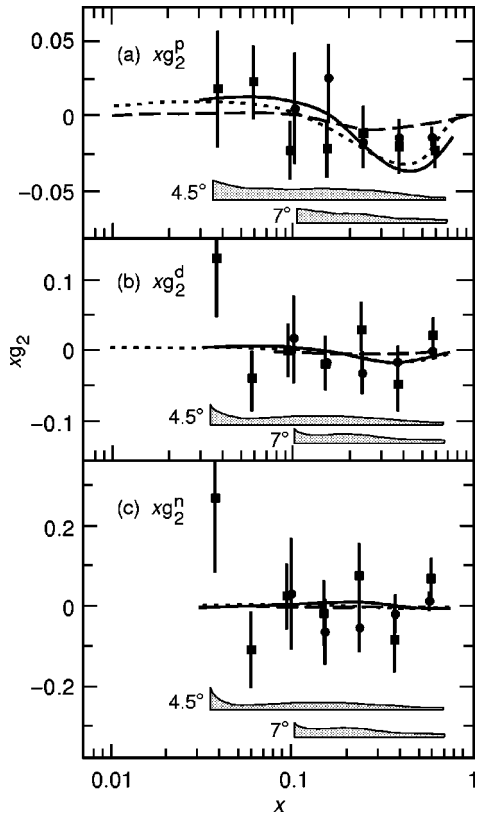

FIG. 20. The results for $xg_2(x,Q^2)$ as a function of x for this experiment (squares for 4.5°, circles for 7°). Systematic errors are indicated by bands. Overlapping data have been shifted slightly in x to make errors clearly visible. The solid curve shows the twist-2 g_2^{WW} calculation for the kinematics of the 4.5° spectrometer. The same curve for 7° is nearly indistinguishable. The bag model calculations at $Q^2=5.0\ (\mathrm{GeV}/c)^2$ by Stratmann [56] (short dash) and Song and McCarthy [57] (long dash) are indicated. The curves on the neutron plot are difficult to distinguish from zero.

TABLE XXXIII. Results for the moments $\Gamma_1^{(2)}$ and $\Gamma_2^{(2)}$ evaluated at $Q^2=5\,(\mathrm{GeV}/c)^2$, and the extracted twist-3 matrix elements d_2 for proton (p), deuteron (d), and neutron (n). The errors include statistical (which dominate) and systematic contributions.

	$a_2/2=\Gamma_1^{(2)}\times 10^3$	$\Gamma_2^{(2)}\times 10^3$	$d_2\times 10^3$
p	12.4 ± 1.0	-6.3 ± 1.8	5.8 ± 5.0
d	4.6 ± 0.8	-1.4 ± 3.0	5.1 ± 9.2
n	-2.4 ± 1.6	3.3 ± 6.5	5.0 ± 21.0

tions of the quarks. It is important to remember that these polarizations have meaning within the quark-parton model where $a_0=\Delta\Sigma$. In pQCD the interpretation becomes scheme-dependent and depends on whether $\Delta G(x)$ contributes to Γ_1. The results are shown in Table XXIX and Fig. 18. Results for both the ''invariant'' and Q^2-dependent pQCD singlet coefficients are shown in the table while the figure shows ''invariant'' results. The quantities a_0, Δu, and Δd are relatively insensitive to the values of F and D, but Δs is very dependent on them. The last two columns of Table XXIX show the errors on Δs with two different estimates on the errors on $3F-D$. As seen in Fig. 18 the results from the deuteron and proton targets are consistent with each other (there is only a small correlation between the errors). The differences between the ''invariant'' and Q^2-dependent results are smaller than the present experimental errors. The negative polarization of the strange quark sea of about -0.08 is very significant only if the smaller estimates of F and D are used. Our averaged proton and deuteron results for $a_0^{inv}=0.33\pm 0.06$, while the world average yields $a_0\sim 0.31\pm 0.04$. The results for a_0 are significantly smaller than the naive parton model prediction of $\Delta\Sigma=1$, the relativistic parton model prediction of 0.75, the Ellis-Jaffe sum rule prediction of 0.58, and a quenched lattice calculation of 0.60 ± 0.05 [132]. With such a low value of a_0, angular momentum conservation [see Eq. (9)] requires that the nucleon spin be dominated by a combination of gluon polarization and orbital angular momentum, or a large charm polarization not included in the formalism above [Eqs. (14)–(20)]. There have been several approaches to understanding the low value of a_0. These are described in Sec. II.

E. A_2 and g_2

Tables XXX–XXXII show A_2 and g_2 for each target and spectrometer (and the derived neutron) with beam energy of 29.1 GeV. Figures 19 and 20 show A_2 and xg_2 for each target and spectrometer. The systematic errors are indicated by the bands. Also shown in Fig. 19 are the results from SMC [9,14] for the deuteron and proton and from E142 [10] and E154 [15] for the neutron. All results are shown at their measured Q^2. There is good agreement between the various experiments. As seen in Fig. 19, the values of A_2^d are consistent with zero, while the values of A_2^p deviate significantly from zero for $x\geqslant 0.1$. For this experiment the average value for all x of A_2 is 0.031 ± 0.007 for the proton, 0.003 ± 0.013 for the deuteron, and -0.03 ± 0.03 for the neutron. The measured A_2 obeys the $\sqrt{R}$ bound within errors, and at almost all kinematics the absolute value of the measured values are significantly lower than the bound. The dashed curve is a calculation of g_2^{WW} from Eq. (24) using g_1 evaluated from a fit to world data discussed in Sec. V A of this paper. The g_2^{WW} curves for the 7° and the 4.5° kinematics are indistinguishable on the figure. The other theoretical curves are bag model predictions [56,57] which include twist-2 and twist-3 contributions for $Q^2=5\,(\mathrm{GeV}/c)^2$. At high x the E143 results for g_2^p indicate a negative trend consistent with the expectations for g_2^{WW} with a χ^2 of 43 for 48 degrees of freedom. However, the results are also consistent with $g_2^p=0$ with a χ^2 of 52. The deuteron and neutron results are less conclusive because of the larger errors and are also consistent with both g_2^{WW} and $g_2=0$. The moments of g_2 will be discussed below along with the moments of g_1.

F. Higher moments of g_1 and g_2

Using our results for both g_1 and g_2, we have computed the third moment of the OPE sum rules [Eq. (25)], and solved for the twist-3 matrix element d_2 and the twist-2 matrix element a_2. For the measured region $0.03<x<0.8$, we evaluated g_1, corrected the twist-2 part of g_2 to fixed $Q^2=5\,(\mathrm{GeV}/c)^2$ assuming g_1/F_1 is independent of Q^2, and have averaged the two spectrometer results. Possible Q^2 dependence of $\overline{g_2}$ was neglected. We neglect the contribution from the region $0\leqslant x<0.03$ because of the x^2 suppression

TABLE XXXIV. Theoretical predictions for the twist-3 matrix elements d_2^p and f_2^p for proton and d_2^d and f_2^d for deuteron. Also shown is μ, the higher twist correction to Γ_1 described in the text.

	Bag models			QCD sum rules			
	Ref. [57]	Ref. [56]	Ref. [53]	Ref. [144]	Ref. [145]	Ref. [52]	Ref. [146]
Q^2 $(\mathrm{GeV}/c)^2$	5	5	1	1	1	1	-
$d_2^p\times 10^3$	17.6	6.0	21	10	-6 ± 3	-3 ± 3	-
$f_2^p\times 10^3$	-	-	35	28	-37 ± 6	-50 ± 34	-69 ± 5
$\mu_2^p\times 10^3$	-	-	27	15	-15 ± 7	-20 ± 13	-27 ± 2
$d_2^d\times 10^3$	6.6	2.9	11	5	-17 ± 5	-13 ± 5	-
$f_2^d\times 10^3$	-	-	17	14	-25 ± 4	-34 ± 20	-38 ± 5
$\mu_2^d\times 10^3$	-	-	13	7	-10 ± 3	-13 ± 8	-15 ± 2

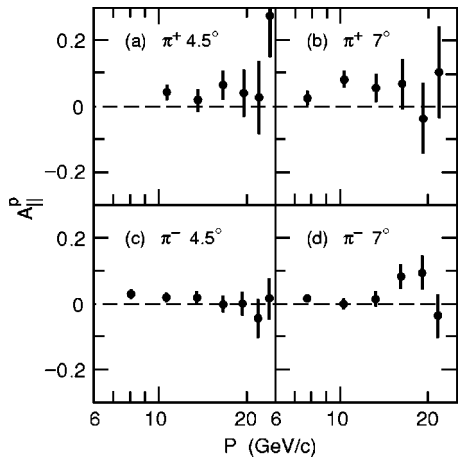

FIG. 21. $A_\parallel$ versus momentum measured from polarized protons for π^- and π^+, at $E=29$ GeV in both spectrometers.

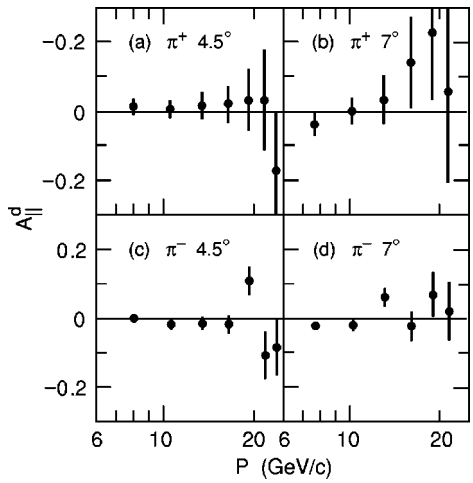

FIG. 22. $A_\parallel$ versus momentum measured from polarized deuterons for π^- and π^+, at $E=29$ GeV in both spectrometers.

factor. For $0.8<x\leqslant 1$, we assume that both g_1 and g_2 behave as $(1-x)^3$ since at high x, $g_2\approx -g_1$ from Eq. (4) and $F_1 \rightarrow 0$, and we fit the data for $x>0.56$. The uncertainty in the extrapolated contribution is taken to be the same as the contribution itself. The results are shown in Table XXXIII. Our extracted values for d_2 are consistent with zero, but the errors are large. For comparison, in Table XXXIV we quote theoretical predictions [52,55–58] for d_2^p and d_2^d. For d_2^d the proton and neutron results were averaged and a deuteron D-state correction was applied. We note that the results for d_2^p and d_2^d differ in sign from the theoretical QCD sum rule calculations [52,55,58]. The bag model predictions [56,57], however, are of the same sign as the data. Ali, Braun and Hiller [133] showed that g_2 obeys an evolution equation in the limit that $N_c\rightarrow\infty$. However, this program of calculation has not been carried out yet.

To test the Burkhardt-Cottingham sum rule, Eq. (27), we have evaluated the integrals $\int_{0.03}^1 g_2^p(x)dx=-0.014\pm 0.028$ and $\int_{0.03}^1 g_2^d(x)dx=-0.034\pm 0.082$ using the same high-x extrapolation as discussed above. These results are consistent with zero. To evaluate the integral for $x\leqslant 0.03$ is theoretically challenging. A double logarithmic approximation has been used [134] to calculate both g_1 and g_2 in the low-x region yielding $g_2\propto x^{-0.75}$ at a fixed Q^2 of a few $(\mathrm{GeV}/c)^2$. Then $\int_0^{0.03} g_2(x)dx$ is negligible and the sum rule is confirmed.

TABLE XXXV. Pion asymmetries versus momentum E' for proton and deuteron targets at $E=29.1$ GeV.

E'(GeV)	$A_\parallel^p(\pi^-)$	$A_\parallel^p(\pi^+)$	$A_\parallel^d(\pi^-)$	$A_\parallel^d(\pi^+)$
		$\theta=4.5°$		
8.04	0.028±0.010	0.016±0.019	0.001±0.011	0.013±0.021
10.65	0.019±0.012	0.043±0.022	−0.017±0.013	0.005±0.025
13.57	0.019±0.016	0.019±0.031	−0.015±0.018	0.016±0.036
16.58	0.001±0.023	0.065±0.043	−0.017±0.025	0.020±0.052
19.41	0.002±0.036	0.041±0.069	0.108±0.041	0.031±0.087
21.88	−0.044±0.056	0.028±0.111	−0.108±0.068	0.031±0.146
23.90	0.018±0.063	0.273±0.127	−0.084±0.079	−0.172±0.171
25.44	0.058±0.082	0.057±0.168	0.057±0.111	0.094±0.242
		$\theta=7.0°$		
5.61	0.123±0.069	−0.010±0.135	0.022±0.072	−0.272±0.195
7.72	0.018±0.010	0.027±0.019	−0.021±0.010	−0.038±0.031
10.29	0.001±0.012	0.081±0.023	−0.019±0.013	0.000±0.037
13.19	0.016±0.022	0.057±0.043	0.063±0.024	0.034±0.071
16.19	0.085±0.036	0.071±0.075	−0.021±0.042	0.142±0.129
19.06	0.096±0.052	−0.035±0.107	0.070±0.063	0.231±0.196
21.59	−0.034±0.064	0.106±0.136	0.023±0.085	0.060±0.263

TABLE XXXVI. The measured virtual photon-nucleon asymmetry $A_1+\eta A_2$ and the spin structure function g_1 for the resonance region. The values of W^2 and Q^2 are given at bin centers. The dilution factor f and applied correction term A_{rc}, which for these data also includes a resolution correction, are from Eqs. (48) and (54). The value of g_1 in the last column is calculated from $A_\parallel$ under the assumption that $A_2=0$.

W^2 GeV^2	Q^2 (GeV/c)^2	f	A_{rc}	$A_1+\eta A_2 \pm$stat$\pm$syst	$g_1 \pm$stat$\pm$syst
			Proton $\theta=4.5°$		
1.31	0.55	0.180	−0.0444	−0.086±0.126±0.225	−0.011±0.017±0.030
1.69	0.54	0.164	−0.0284	−0.453±0.125±0.127	−0.112±0.031±0.032
2.06	0.53	0.155	0.0101	0.461±0.106±0.104	0.139±0.032±0.031
2.44	0.52	0.153	0.0204	0.694±0.091±0.086	0.344±0.045±0.035
2.81	0.50	0.154	−0.0051	0.222±0.078±0.046	0.142±0.050±0.027
3.19	0.49	0.144	−0.0049	0.242±0.079±0.092	0.142±0.046±0.050
3.56	0.48	0.144	−0.0047	0.090±0.072±0.030	0.061±0.049±0.018
3.94	0.47	0.147	−0.0032	0.002±0.064±0.011	0.002±0.054±0.010
4.31	0.46	0.144	−0.0013	0.134±0.059±0.017	0.129±0.057±0.008
4.69	0.45	0.143	−0.0013	0.105±0.056±0.014	0.110±0.058±0.009
			Deuteron $\theta=4.5°$		
1.31	0.55	0.247	−0.0242	−0.173±0.278±0.236	−0.015±0.024±0.021
1.69	0.54	0.235	−0.0221	−0.305±0.231±0.078	−0.061±0.047±0.015
2.06	0.53	0.232	−0.0009	0.290±0.157±0.095	0.107±0.058±0.034
2.44	0.52	0.227	0.0115	0.184±0.152±0.072	0.078±0.064±0.030
2.81	0.50	0.232	0.0030	0.021±0.128±0.055	0.011±0.068±0.029
3.19	0.49	0.230	−0.0033	0.147±0.113±0.021	0.093±0.072±0.011
3.56	0.48	0.230	−0.0040	0.023±0.102±0.011	0.017±0.074±0.008
3.94	0.47	0.230	−0.0037	−0.017±0.096±0.010	−0.014±0.078±0.008
4.31	0.46	0.233	−0.0031	−0.034±0.091±0.009	−0.030±0.080±0.008
4.69	0.45	0.229	−0.0028	0.055±0.086±0.010	0.053±0.084±0.008
			Proton $\theta=7.0°$		
1.56	1.26	0.159	−0.0524	−0.143±0.128±0.113	−0.015±0.013±0.012
1.94	1.23	0.154	−0.0012	0.349±0.110±0.105	0.038±0.012±0.012
2.31	1.20	0.156	0.0251	0.795±0.087±0.088	0.177±0.019±0.020
2.69	1.18	0.158	0.0036	0.593±0.077±0.058	0.163±0.021±0.014
3.06	1.15	0.154	0.0046	0.507±0.069±0.078	0.177±0.024±0.025
3.44	1.12	0.150	0.0029	0.262±0.066±0.035	0.101±0.025±0.010
3.81	1.10	0.148	0.0027	0.299±0.063±0.039	0.136±0.028±0.008
4.19	1.07	0.148	0.0038	0.433±0.059±0.062	0.221±0.030±0.012
4.56	1.04	0.148	0.0035	0.324±0.056±0.054	0.185±0.032±0.017
4.94	1.02	0.147	0.0033	0.237±0.053±0.037	0.150±0.034±0.010
			Deuteron $\theta=7.0°$		
1.56	1.26	0.232	−0.0312	0.043±0.243±0.103	0.003±0.017±0.007
1.94	1.23	0.232	−0.0131	0.163±0.179±0.128	0.018±0.019±0.014
2.31	1.20	0.230	0.0108	0.183±0.154±0.033	0.030±0.025±0.005
2.69	1.18	0.231	0.0110	0.237±0.134±0.072	0.054±0.030±0.016
3.06	1.15	0.234	0.0019	0.389±0.114±0.046	0.112±0.033±0.012
3.44	1.12	0.228	0.0000	0.081±0.105±0.017	0.028±0.037±0.006
3.81	1.10	0.228	−0.0005	0.121±0.099±0.019	0.049±0.040±0.006
4.19	1.07	0.230	−0.0002	0.178±0.094±0.030	0.080±0.042±0.009
4.56	1.04	0.230	−0.0006	0.145±0.091±0.026	0.073±0.046±0.008
4.94	1.02	0.230	−0.0006	0.201±0.085±0.036	0.113±0.048±0.012

G. Higher twist effects

We have compared our experimental integrals with theoretical predictions using pQCD for the finite Q^2 corrections to various sum rules, which were originally derived at infinite Q^2. At low Q^2 it is possible that higher twist effects could also influence the evolution of g_1. These terms generate a multiplicative term of the form $\{1+C/[Q^2(1-x)]\}$ [135]. When going to very high order in pQCD there is a confusion between resummation effects generating $1/Q^2$ terms and the higher twist terms. There have been several calculations of the corrections to Γ_1 using QCD sum rules and the bag model (see the reviews [136]). These take the form of an additive correction to the sum rule of the form μ^t/Q^2 where t=p, n, or d for proton, neutron, or deuteron. From QCD sum rules [25,54] the higher twist contribution to Γ_1 is:

$$\Gamma_1^{HT}=\frac{M_N^2}{Q^2}(a_2+4d_2+4f_2)+O\left(\frac{M_N^4}{Q^4}\right)=\frac{\mu}{Q^2}+O\left(\frac{M_N^4}{Q^4}\right) \tag{56}$$

where a_2 (twist-2) and d_2 (twist-3) have been calculated from data above and f_2 is twist-4. The contribution to μ from a_2 and d_2 is 0.004 for the proton and 0.002 for the deuteron, which are quite negligible at our average $Q^2=3\,(\mathrm{GeV}/c)^2$ and small compared to the estimated contributions from f_2. Table XXXIV shows calculated values of μ_2^p and μ_2^d using bag models and QCD sum rules. The sum rule calculations average about -0.02 for the proton and -0.013 for the deuteron and thus would have an effect on the calculation of Γ_1 at our average Q^2 of $3\,(\mathrm{GeV}/c)^2$ comparable to our experimental error. The bag model calculations are similar in magnitude but opposite in sign to the sum rule calculations. A different type of calculation, using a diquark model [138] gives a higher twist contribution of a different form than Eq. (56), which numerically is 1% or less of both Γ_1^{Bj} and Γ_1^p for $Q^2\geqslant 2\,(\mathrm{GeV}/c)^2$. Using data from this experiment, Ji and Melnitchouk [85] have extracted values for the twist-4 matrix element f_2. Combining this with results for a_2 and d_2 they find for the proton $\mu_2^p=0.04\pm0.02$, and for the neutron $\mu_2^n=0.03\pm0.04$.

The QCD sum rule higher-twist correction and a Pade summation of the perturbative terms have been applied to the Bjorken sum rule [Eq. (20)] by Ellis *et al.* [137]. They then use world data, including the preliminary results from this experiment, and find excellent agreement between experiment and theory. Working backwards, they determine the best value of α_s is $0.117^{+0.004}_{-0.007}\pm0.002$ where the first set of errors is experimental and the second theoretical, in excellent agreement with the world average of 0.118 ± 0.003.

H. Pion asymmetry

The asymmetries for π^+ and π^- for our primary energy of 29 GeV corresponding to target polarization parallel and anti-parallel to the beam direction ($A_\parallel^\pi$) are shown in Figs. 21 and 22. These data were measured using our polarized NH_3 and ND_3 targets, and were corrected for beam and target polarizations as well as dilution to obtain the asymmetries from polarized protons and deuterons. The asymmetries are small, but for the proton may be slightly positive for both signs of pions at small momentum. Table XXXV gives the pion asymmetry at the beam energy of 29.1 GeV for proton and deuteron targets. Data for other beam energies and for the target spins oriented perpendicular to the beam direction have much larger statistical errors and are consistent with zero.

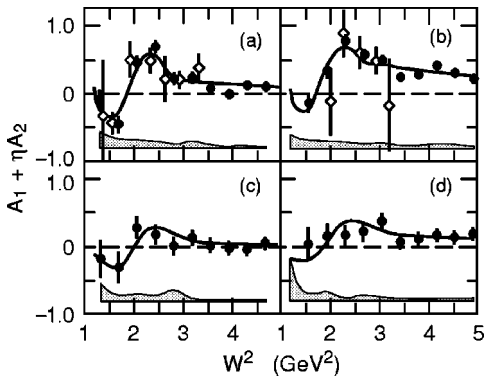

FIG. 23. Extracted values for $A_1+\eta A_2$ (circles) in the resonance region for the proton at (a) 4.5° and (b) 7.0°; and for the deuteron at (c) 4.5° and (d) 7.0°. Also shown are the Monte Carlo predictions (solid line) and the data of Baum *et al.* [139] (diamonds). Error bars correspond to statistical errors only, whereas the bands below the data correspond to the systematic errors.

I. Resonance region

Results for $A_1+\eta A_2$ extracted via the asymmetry method for the resonance region ($W^2<5\ \mathrm{GeV}^2$) are shown in Table XXXVI and in Fig. 23. Also shown in Fig. 23 is the data of Baum *et al.* [139]. The two data sets agree within the errors of both measurements. The asymmetry is negative and close to the expected value $A_1=-\frac{1}{2}$ for the Δ resonance. In the region of the D_{13} and the S_{11} resonances ($W^2\sim2.34\ \mathrm{GeV}^2$) $A_1+\eta A_2$ is large and positive. Although η is large for our kinematics, a small value of A_2 would imply that $A_1+\eta A_2$ is $\approx A_1$.

Table XXXVII lists the systematic errors on $A_1+\eta A_2$ by category. The procedure for estimating these is as follows: (a) radiative corrections (A_{rc}): the maximum deviation in the radiative correction resulting from a 50% change in the input asymmetries; (b) model dependence (model): the worst-case change due to using various cross-section models in the extraction of $A_1+\eta A_2$ from $A_\parallel$; (c) central angle (θ): uncertainty due to the location of the central angle of the spectrometers; (d) energy calibration (E'): uncertainty due to the spectrometer energy calibration; (e) spectrometer resolution (Resol): the maximum difference obtained by varying the width of the hodoscope fingers by 20% and re-running the Monte Carlo routine; (f) polarization (P_bP_t): combined uncertainty in the beam and target polarizations; (g) dilution factor (f): uncertainty based on the variations in the calculated dilution factor with various cross-section models and

TABLE XXXVII. Systematic errors (absolute) on $A_1 + \eta A_2$ by category for the resonance region (see text for details).

W^2	A_{rc}	model	θ	E'	Resol	$P_b P_t$	f	R	g_2
				Proton $\theta = 4.5°$					
1.31	0.0083	0.1842	0.0033	0.1156	0.0328	0.0354	0.0260	0.0188	0.0057
1.69	0.0006	0.1245	0.0051	0.0163	0.0052	0.0019	0.0014	0.0169	0.0046
2.06	0.0837	0.0082	0.0077	0.0541	0.0019	0.0145	0.0106	0.0224	0.0040
2.44	0.0548	0.0614	0.0070	0.0114	0.0098	0.0211	0.0155	0.0520	0.0088
2.81	0.0339	0.0019	0.0014	0.0201	0.0040	0.0106	0.0078	0.0191	0.0042
3.19	0.0544	0.0832	0.0008	0.0118	0.0027	0.0106	0.0078	0.0349	0.0040
3.56	0.0146	0.0256	0.0004	0.0003	0.0008	0.0045	0.0033	0.0150	0.0036
3.94	0.0102	0.0015	0.0000	0.0022	0.0020	0.0009	0.0006	0.0003	0.0032
4.31	0.0011	0.0028	0.0006	0.0012	0.0010	0.0055	0.0040	0.0156	0.0031
4.69	0.0062	0.0017	0.0004	0.0008	0.0001	0.0043	0.0032	0.0115	0.0029
				Deuteron $\theta = 4.5°$					
1.31	0.1965	0.1531	0.0242	0.1203	0.0375	0.0236	0.0132	0.0027	0.0033
1.69	0.0638	0.0613	0.0129	0.0331	0.0048	0.0015	0.0008	0.0259	0.0049
2.06	0.0220	0.0861	0.0180	0.0197	0.0044	0.0161	0.0090	0.0234	0.0058
2.44	0.0107	0.0702	0.0059	0.0073	0.0010	0.0046	0.0026	0.0126	0.0040
2.81	0.0074	0.0542	0.0017	0.0047	0.0013	0.0004	0.0002	0.0016	0.0022
3.19	0.0110	0.0047	0.0067	0.0046	0.0016	0.0099	0.0056	0.0108	0.0034
3.56	0.0037	0.0099	0.0014	0.0003	0.0002	0.0027	0.0015	0.0017	0.0022
3.94	0.0029	0.0094	0.0003	0.0001	0.0002	0.0003	0.0002	0.0016	0.0019
4.31	0.0021	0.0084	0.0011	0.0008	0.0002	0.0009	0.0005	0.0037	0.0016
4.69	0.0024	0.0056	0.0027	0.0007	0.0001	0.0039	0.0022	0.0060	0.0016
				Proton $\theta = 7.0°$					
1.56	0.0186	0.1033	0.0010	0.0126	0.0386	0.0163	0.0090	0.0030	0.0010
1.94	0.0165	0.0186	0.0086	0.1006	0.0010	0.0163	0.0089	0.0137	0.0019
2.31	0.0742	0.0028	0.0150	0.0171	0.0141	0.0258	0.0141	0.0251	0.0081
2.69	0.0103	0.0287	0.0088	0.0196	0.0012	0.0237	0.0130	0.0370	0.0064
3.06	0.0342	0.0630	0.0057	0.0105	0.0043	0.0200	0.0110	0.0385	0.0064
3.44	0.0106	0.0196	0.0029	0.0039	0.0024	0.0100	0.0055	0.0262	0.0033
3.81	0.0075	0.0030	0.0030	0.0021	0.0013	0.0115	0.0063	0.0353	0.0040
4.19	0.0054	0.0056	0.0040	0.0004	0.0004	0.0164	0.0090	0.0591	0.0061
4.56	0.0071	0.0235	0.0028	0.0005	0.0005	0.0127	0.0070	0.0463	0.0046
4.94	0.0009	0.0099	0.0018	0.0004	0.0003	0.0089	0.0049	0.0341	0.0039
				Deuteron $\theta = 7.0°$					
1.56	0.0887	0.0335	0.0008	0.0355	0.0288	0.0216	0.0091	0.0030	0.0018
1.94	0.0144	0.1146	0.0172	0.0523	0.0004	0.0158	0.0066	0.0016	0.0019
2.31	0.0206	0.0020	0.0111	0.0185	0.0051	0.0064	0.0027	0.0113	0.0028
2.69	0.0072	0.0686	0.0095	0.0040	0.0004	0.0098	0.0041	0.0163	0.0043
3.06	0.0085	0.0136	0.0209	0.0052	0.0110	0.0229	0.0096	0.0269	0.0083
3.44	0.0045	0.0129	0.0051	0.0033	0.0032	0.0049	0.0020	0.0056	0.0031
3.81	0.0045	0.0101	0.0068	0.0003	0.0030	0.0073	0.0030	0.0115	0.0031
4.19	0.0046	0.0095	0.0101	0.0062	0.0004	0.0113	0.0047	0.0232	0.0045
4.56	0.0015	0.0075	0.0079	0.0032	0.0004	0.0091	0.0038	0.0208	0.0037
4.94	0.0063	0.0059	0.0109	0.0082	0.0011	0.0130	0.0054	0.0289	0.0054

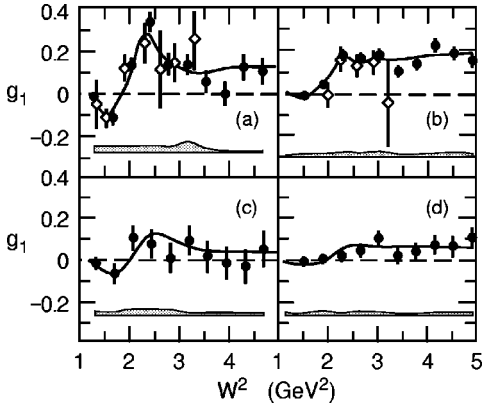

FIG. 24. Measurements of $g_1(x,Q^2)$ in the resonance region as a function of W^2 for the proton at (a) 4.5° and (b) 7°; and for the deuteron at (c) 4.5° and (d) 7°. The present data (circles) are plotted together with the data of Baum *et al.* [139] (diamonds) and our Monte Carlo simulation (solid line). The errors are indicated as in Fig. 23.

the stated uncertainty in the target composition; (h) $R(x,Q^2)$ (R): uncertainty arising from lack of knowledge of $R=\sigma_L/\sigma_T$; (i) no transverse data (g_2): uncertainty in the extraction of g_1 from $A_1+\eta A_2$ due to the lack of knowledge about A_2. This was estimated using the maximum deviations in g_1 assuming $A_2=0$ and $g_2=0$. Even if A_2 were as large as 0.3, the extracted values of g_1 would shift by less than 0.014, which is small compared to the statistical errors on each point. By far the largest error comes from radiative and resolution corrections.

In addition to $A_1+\eta A_2$, Table XXXVI also shows the results for g_1 for the resonance region. Figure 24 shows g_1 for proton and deuteron (per nucleon) measured with the two spectrometers as a function of W^2. The data of Baum *et al.* [139] are taken at similar kinematics and converted to g_1 for comparison by assuming $A_2=0$. Within errors, the two measurements agree well. Both data sets show a negative contribution in the region of the $\Delta(1232)$ resonance at $W^2 \approx 1.5\ \mathrm{GeV}^2$, and a strongly positive contribution just above $W^2=2\ \mathrm{GeV}^2$ where the S_{11} and D_{13} resonances are important. This peak is less pronounced for the deuteron. The solid lines show the Monte Carlo simulation.

Figure 25 shows the integrals $\Gamma_1(Q^2)$ for proton and neutron, evaluated at the average Q^2 for the resonance region $(M^2<W^2<4\ \mathrm{GeV}^2)$. We summed our resonance results directly (where Q^2 does not vary much) and then added a contribution from smaller x (larger W^2) at the same fixed Q^2 by interpolating the 9.7 and 16 GeV data to the appropriate Q^2. The neutron integrals were derived assuming a 5% D-state probability for the deuteron. The statistical errors assigned to the integral over the deep-inelastic region $(\Gamma_1^{\mathrm{DIS}})$ correspond to the weighted average of the statistical errors on the corresponding 9.7 and 16.2 GeV data points used in the interpolation. Systematic errors on the total integral Γ_1^{tot} were calculated using the systematic uncertainties for the measured g_1 in the resonance region added linearly to the systematic errors for the deep-inelastic region, which are highly correlated with each other. For the $x<0.03$ extrapolation we simply took the overall parametrization of the data and integrated it from $x=0$ to $x=0.03$. Extrapolation errors for the region below the last measured datum at $x=0.03$ were taken to be as large as the values themselves. Table XXXVIII lists for each target the numerical values for the integrals in the resonance region alone $(\Gamma_1^{\mathrm{res}})$, in the deep-inelastic region $(\Gamma_1^{\mathrm{DIS}})$, for the low-$x$ extrapolation $(\Gamma_1^{\mathrm{ext}})$, and for the combined total $(\Gamma_1^{\mathrm{tot}})$.

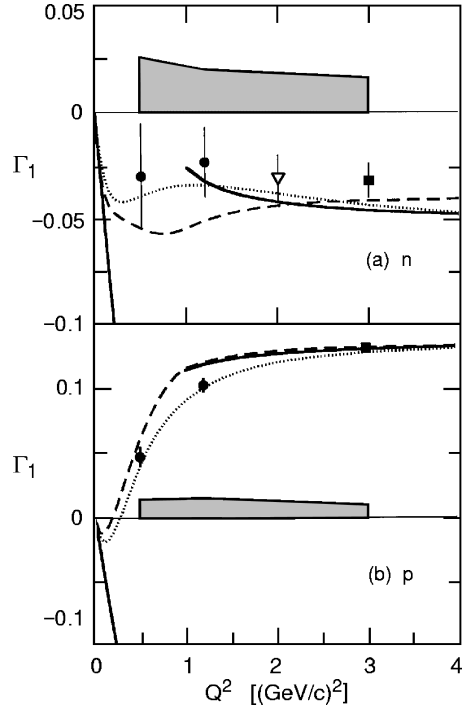

FIG. 25. Integrals of $g_1(x,Q^2)$ at several fixed values of Q^2 for (a) the neutron and (b) the proton. The present data (circles) are plotted together with data from E143 deep-inelastic results from this experiment (squares) and E142 [10] (inverted triangle). The curves correspond to the evolution [33] of the deep-inelastic results due to changing α_s (solid), the predictions of Burkert and Ioffe [142] (short dash), the model of Soffer [143] (long dash), and the GDH approach to $Q^2=0$ (solid). The error bars are statistical, and the shaded bands correspond to the systematic errors.

Although several models for the Q^2 evolution of $\Gamma_1(Q^2)$ exist [53,140–143], we show here only two representative ones, together with the evolution [33] of the world's deep-inelastic data due to the changing coupling constant α_S. Although the GDH sum rule is strictly valid only at $Q^2=0$ where $\Gamma_1(Q^2)$ vanishes, it can be used to predict the slope of $\Gamma_1(Q^2)$ for small Q^2. The solid line at low Q^2 shows $\Gamma_1=-\kappa^2Q^2/8M^2$ in which κ is the anomalous magnetic moment of either the proton or neutron. Burkert and Ioffe [142] consider the contributions from the resonances using the code AO, and the nonresonant contributions using a simple higher-twist-type form fitted to the deep-inelastic data. Their model is constrained to fit both the GDH and the deep-inelastic limits, and it describes the data quite well. Soffer and Teryaev [143] assume that the integral over g_1+g_2 varies smoothly from high Q^2 where $g_2\approx 0$ down to $Q^2=0$. Using their simple prediction for this integral and subtracting

TABLE XXXVIII. Integrals $\Gamma_1(Q^2)$ of the structure functions g_1 for the proton (p), deuteron and neutron (n) at low Q^2. Listed are the measured sums $\Gamma_1^{\rm res}$ for the resonance region ($W^2<4$ GeV^2) and $\Gamma_1^{\rm DIS}$ for the deep-inelastic region ($W^2>4$ GeV^2 using data from 9.7 and 16 GeV beam energies), the low-x extrapolation $\Gamma_1^{\rm ext}$ for $x<0.03$, and the combined total $\Gamma_1^{\rm tot}$.

Q^2 (GeV/c)^2		$\Gamma_1^{\rm res}\pm$stat$\pm$syst	$\Gamma_1^{\rm DIS}\pm$stat$\pm$syst	$\Gamma_1^{\rm ext}$	$\Gamma_1^{\rm tot}\pm$stat$\pm$syst
0.5	Proton	$0.022\pm0.007\pm0.008$	$0.017\pm0.002\pm0.003$	0.009	$0.047\pm0.007\pm0.015$
0.5	Deuteron	$0.004\pm0.010\pm0.008$	$0.004\pm0.003\pm0.002$	0.000	$0.008\pm0.011\pm0.009$
0.5	Neutron	$-0.013\pm0.023\pm0.018$			$-0.030\pm0.024\pm0.025$
0.5	p-n				$0.077\pm0.027\pm0.036$
1.2	Proton	$0.039\pm0.003\pm0.003$	$0.051\pm0.003\pm0.003$	0.014	$0.104\pm0.005\pm0.016$
1.2	Deuteron	$0.018\pm0.005\pm0.003$	$0.019\pm0.006\pm0.002$	0.001	$0.037\pm0.007\pm0.006$
1.2	Neutron	$-0.001\pm0.010\pm0.008$			$-0.023\pm0.016\pm0.020$
1.2	p-n				$0.127\pm0.018\pm0.034$

the contribution from g_2 using the Burkhardt-Cottingham sum rule [74] gives the dashed curves in Fig. 25, which also agree quite well with our data.

The present spin structure function data in the region of the nucleon resonances allow us to determine the integrals $\Gamma_1(Q^2)$ for the first time at Q^2 below 2 (GeV/c)^2. In contrast to the nearly flat behavior in the deep-inelastic region above $Q^2=2$ (GeV/c)^2, Γ_1 varies rapidly below $Q^2=2$ (GeV/c)^2. Models that interpolate between the deep-inelastic and GDH limits describe the data quite well in this non-perturbative regime.

VI. CONCLUSION

In summary, we have presented final results from SLAC Experiment E143 on the spin structure functions g_1 and g_2 for proton and deuteron targets covering a wide range of kinematics from the deep-inelastic to the resonance region. For deep-inelastic data the ratio g_1/F_1 is consistent with being independent of Q^2 for $Q^2\geqslant 1$ (GeV/c)^2, but also consistent with pQCD NLO fits which show a weak Q^2 dependence. We have evaluated the first moments of g_1, using a Regge form for the unmeasured low x region. The Ellis-Jaffe sum rules are a function of the SU(3) parameters F and D and the validity of the sum rules depend critically on the errors assigned to these parameters. We find $a_0^{inv}=0.33\pm0.06$, and in the parton model interpretation we find the average results: $\Delta u=0.84\pm0.02$, $\Delta d=-0.42\pm0.02$, and $\Delta s=-0.09\pm0.02$ or ±0.05 depending on $\delta F/D$. Combined world data are consistent with the Bjorken sum rule at the one standard deviation level of 7%. Results for the twist-3 matrix element extracted from the higher moments of g_1 and g_2 are consistent with calculations within the large errors. The resonance region data show the theoretically expected asymmetries at the $\Delta(1232)$ peak and larger than expected asymmetries (at least at low Q^2) in the region of the S_{11} and D_{13} resonances. The first moment of $g_1^p(Q^2)$ decreases with decreasing Q^2 at low Q^2 toward the GDH sum rule limit as predicted by several models. The asymmetry of pions is close to zero.

With the current round of experiments we now have good knowledge of the distribution of quark spins for $x\geqslant 0.003$. A complete understanding of the spin structure of the nucleon awaits experiments to measure directly the gluon spin distribution and to probe the quark spin distribution at lower x.

ACKNOWLEDGMENTS

This work was supported in part by Department of Energy contract DE-AC03-76SF00515. We wish to thank the SLAC staff for making this experiment a success. This work was supported by Department of Energy contracts DE-AC05-84ER40150 (TJNAF), W-2705-Eng-48 (LLNL), DE-FG05-94ER40859 (ODU), DE-AC03-76SF00515 (SLAC), DE-FG03-88ER40439 (Stanford), DE-FG05-88ER40390 and DEFG05-86ER40261 (Virginia), and DE-AC02-76ER00881 (Wisconsin): by National Science Foundation Grants 9114958 (American), 9307710 (Massachusetts), 9217979 (Michigan), 9104975 (ODU), and 9118137 (U. Penn.); by the Schweizersche Nationalfonds (Basel); by the Commonwealth of Virginia (Virginia); by the Centre National de la Recherche Scientifique and the Commissariat a l'Energie Atomique (French groups); by the Japanese Ministry of Education, Science, and Culture (Tohoku); and by the Jeffress Memorial Trust (William & Mary).

[1] V. N. Gribov and L. N. Lipatov, Yad. Fiz. **15**, 781 (1972) [Sov. J. Nucl. Phys. **15**, 438 (1972)]; Y. L. Dokshitzer, Sov. Phys. JETP **46**, 461 (1977); G. Altarelli and G. Parisi, Nucl. Phys. **B126**, 298 (1977).

[2] E80 Collaboration, M. J. Alguard *et al.*, Phys. Rev. Lett. **37**, 1261 (1976); **41**, 70 (1978).

[3] E130 Collaboration, G. Baum *et al.*, Phys. Rev. Lett. **51**, 1135 (1983).

[4] E143 Collaboration, K. Abe *et al.*, Phys. Rev. Lett. **74**, 346 (1995).
[5] E143 Collaboration, K. Abe *et al.*, Phys. Lett. B **364**, 61 (1995).
[6] EMC Collaboration, J. Ashman *et al.*, Nucl. Phys. **B328**, 1 (1989).
[7] SMC Collaboration, D. Adams *et al.*, Phys. Lett. B **329**, 399 (1994); D. Adams *et al.*, Phys. Rev. D **56**, 5330 (1997).
[8] E143 Collaboration, K. Abe *et al.*, Phys. Rev. Lett. **75**, 25 (1995).
[9] SMC Collaboration, B. Adeva *et al.*, Phys. Lett. B **302**, 533 (1993); D. Adams *et al.*, *ibid.* **357**, 248 (1995); D. Adams *et al.*, *ibid.* **396**, 338 (1997).
[10] E142 Collaboration, P. L. Anthony *et al.*, Phys. Rev. Lett. **71**, 959 (1993); Phys. Rev. D **54**, 6620 (1996).
[11] E154 Collaboration, K. Abe *et al.*, Phys. Rev. Lett. **79**, 26 (1997); Phys. Lett. B **404**, 377 (1997); **405**, 180 (1997).
[12] Hermes Collaboration, K. Ackerstaff *et al.*, Phys. Lett. B **404**, 383 (1997).
[13] E143 Collaboration, K. Abe *et al.*, Phys. Rev. Lett. **76**, 587 (1996).
[14] SMC Collaboration, D. Adams *et al.*, Phys. Lett. B **336**, 125 (1994).
[15] E154 Collaboration, K. Abe *et al.*, Phys. Lett. B **404**, 377 (1997).
[16] E143 Collaboration, K. Abe *et al.*, Phys. Rev. Lett. **78**, 815 (1997).
[17] J. D. Bjorken, Phys. Rev. **148**, 1467 (1966); Phys. Rev. D **1**, 1376 (1970).
[18] P. Stoler, Phys. Rep. **226**, 103 (1993).
[19] C. E. Carlson and N. C. Mukhopadhyay, hep-ph/9801205; Report No. RPI-97-N122.
[20] R. L. Jaffe and A. V. Manohar, Nucl. Phys. **B337**, 509 (1990).
[21] M. Beyer and S. K. Singh, Z. Phys. C **31**, 421 (1986).
[22] S. J. Brodsky and F. Schlumpf, Phys. Lett. B **329**, 111 (1994).
[23] M. Anselmino, A. Efremov, and E. Leader, Phys. Rep. **261**, 1 (1995).
[24] R. L. Jaffe and X. Ji, Phys. Rev. D **43**, 724 (1991).
[25] E. V. Shuryak and A. I. Vainshtein, Nucl. Phys. **B199**, 451 (1982); **B201**, 141 (1982).
[26] Particle Data Group, R. M. Barnett *et al.*, Phys. Rev. D **54**, 1 (1996).
[27] F. E. Close and R. G. Roberts, Phys. Lett. B **316**, 165 (1993).
[28] P. G. Ratcliffe, Phys. Lett. B **242**, 271 (1990).
[29] P. G. Ratcliffe, Phys. Lett. B **365**, 383 (1996).
[30] J. F. Donoghue, B. R. Holstein, and S. W. Klimt, Phys. Rev. D **35**, 934 (1987).
[31] B. Ehrnsperger and A. Schäfer, Phys. Lett. B **348**, 619 (1995).
[32] X. Song, J. S. McCarthy, and H. J. Weber, Phys. Rev. D **55**, 2624 (1997).
[33] S. A. Larin and J. A. M. Vermaseren, Phys. Lett. B **259**, 345 (1991), and references therein; S. A. Larin, *ibid.* **334**, 192 (1994).
[34] A. L. Kataev and V. Starshenko, Mod. Phys. Lett. A **10**, 235 (1995).
[35] R. D. Ball, S. Forte, and G. Ridolfi, Nucl. Phys. **B444**, 287 (1995); **B449**, 680(E) (1995); Phys. Lett. B **378**, 255 (1996).
[36] S. L. Adler, Phys. Rev. **177**, 2426 (1969); J. S. Bell and R. Jackiw, Nuovo Cimento **47**, 61 (1969); A. V. Efremov and O. V. Teryaev, Dubna Report No. JIN-E2-88-287(1988); G. Altarelli and G. Ross, Phys. Lett. B **212**, 391 (1988); R. D. Carlitz, J. D. Collins, and A. H. Mueller, *ibid.* **214**, 219 (1988).
[37] G. Altarelli, R. D. Ball, S. Forte, and G. Ridolfi, Nucl. Phys. **B496**, 337 (1997).
[38] L. Mankiewicz, G. Piller, and A. Saalfeld, Phys. Lett. B **395**, 318 (1997).
[39] P. Chiappetta, P. Colangelo, J. P. Guillet, and G. Nardulli, Z. Phys. C **59**, 629 (1993).
[40] I. Halperin and A. Zhitnitsky, hep-ph/9706251.
[41] S. J. Brodsky and B. Q. Ma, Phys. Lett. B **381**, 317 (1996).
[42] S. J. Brodsky, J. Ellis, and M. Karliner, Phys. Lett. B **206**, 309 (1988).
[43] H. Hogaasen and F. Myhrer, Z. Phys. C **68**, 625 (1995); Phys. Lett. B **214**, 123 (1988).
[44] S. Narison, G. M. Shore, and G. Veneziano, Nucl. Phys. **B433**, 209 (1995).
[45] C. Bourrely *et al.*, Z. Phys. C **62**, 431 (1994).
[46] R. Altmeyer *et al.*, Phys. Rev. D **49**, R3087 (1994).
[47] M. Fukugita, Y. Kuramashi, M. Okawa, and A. Ukawa, Phys. Rev. Lett. **75**, 2092 (1995).
[48] S. J. Dong, J. F. Lagae, and K. F. Liu, Phys. Rev. Lett. **75**, 2096 (1995).
[49] M. Göckeler *et al.*, Phys. Rev. D **53**, 2317 (1996).
[50] J. Ellis and M. Karliner, Phys. Lett. B **341**, 397 (1995).
[51] J. Ellis and R. Jaffe, Phys. Rev. D **9**, 1444 (1974); **10**, 1669(E) (1974).
[52] I. I. Balitsky, V. M. Braun, and A. V. Kolesnichenko, Phys. Lett. B **242**, 245 (1990); **318**, 648(E) (1993).
[53] X. Ji and P. Unrau, Phys. Lett. B **333**, 228 (1994).
[54] B. Ehrnsperger, L. Mankiewicz, and A. Schäfer, Phys. Lett. B **323**, 439 (1994).
[55] E. Stein, P. Gornicki, L. Mankiewicz, and A. Schäfer, Phys. Lett. B **353**, 107 (1995).
[56] M. Stratmann, Z. Phys. C **60**, 763 (1993); (private communication), for values at $Q^2=5\,(\mathrm{GeV}/c)^2$.
[57] X. Song, Phys. Rev. D **54**, 1955 (1996).
[58] E. Stein *et al.*, Phys. Lett. B **343**, 369 (1995).
[59] M. Glück, E. Reya, M. Stratmann, and W. Vogelsang, Phys. Rev. D **53**, 4775 (1996).
[60] E. B. Zijlstra and W. L. van Neerven, Nucl. Phys. **B417**, 61 (1994); R. Mertig and W. L. van Neervan, Z. Phys. C **70**, 637 (1996).
[61] R. P. Feynman, *Photon-Hadron Interactions* (Benjamin, New York, 1972).
[62] E. Leader and M. Anselmino, Z. Phys. C **41**, 239 (1988).
[63] B. L. Ioffe, V. A. Khoze, and L. N. Lipatov, *Hard Processes* (North-Holland, Amsterdam, 1984).
[64] G. L. Kane, J. Pumplin, and W. Repko, Phys. Rev. Lett. **41**, 1689 (1978).
[65] R. L. Jaffe, Lecture given at Ettore Majorana International School of Nucleon Structure, Erice, Italy, 1995, hep-ph/9602236.
[66] R. L. Jaffe and X. Ji, Phys. Rev. Lett. **67**, 552 (1991).
[67] A. P. Bukhvostov, G. V. Frolov, L. N. Lipatov, and E. A.

Kuraev, Nucl. Phys. **B258**, 601 (1985).
[68] A. V. Efremov and O. V. Teryaev, Phys. Lett. **150B**, 383 (1985).
[69] P. G. Ratcliffe, Nucl. Phys. **B264**, 493 (1986).
[70] L. Mankiewicz and Z. Rysak, Phys. Rev. D **43**, 733 (1991).
[71] J. L. Cortes, B. Pire, and J. P. Ralston, Z. Phys. C **55**, 409 (1992).
[72] R. L. Jaffe, Comments Nucl. Part. Phys. **19**, 239 (1990).
[73] S. Wandzura and F. Wilczek, Phys. Lett. **72B**, 195 (1977).
[74] H. Burkhardt and W. N. Cottingham, Ann. Phys. (N.Y.) **56**, 453 (1970).
[75] S. Wandzura, Nucl. Phys. **B122**, 412 (1977).
[76] S. Matsuda and T. Uematsu, Nucl. Phys. **B168**, 181 (1980).
[77] H. Kawamura and T. Uematsu, Phys. Lett. B **343**, 346 (1995).
[78] A. Piccione and G. Ridolfi, Nucl. Phys. **B513**, 301 (1998).
[79] T. D. Averett, Ph.D. thesis, University of Virginia, 1995.
[80] H. Breuker *et al.*, Z. Phys. C **13**, 113 (1982); **17**, 121 (1983); E. Evangelides *et al.*, Nucl. Phys. **B71**, 381 (1974); W. Brasse *et al.*, *ibid.* **B110**, 413 (1976); **B139**, 37 (1978); V. Gerhardt, Report No. DESY-F21-79/02, 1979 (unpublished); R. Haidan, Report No. DESY-F21-79/03, 1979 (unpublished).
[81] V. Burkert and L. Elouadrhiri, Phys. Rev. Lett. **75**, 3614 (1995).
[82] C. Keppel, Ph.D. thesis, American University, 1994.
[83] L. W. Whitlow *et al.*, Phys. Lett. B **250**, 193 (1990). Note that in Eq. (6) $b1$ should be 0.06347, not 0.635.
[84] S. Gerasimov, Sov. J. Nucl. Phys. **2**, 430 (1966); S. D. Drell and A. C. Hearn, Phys. Rev. Lett. **16**, 908 (1966).
[85] X. Ji and W. Melnitchouk, Phys. Rev. D **56**, R1 (1997).
[86] T. Maruyama, E. L. Garwin, R. Prepost, and G. H. Zapalac, Phys. Rev. B **46**, 4261 (1992).
[87] R. Prepost and T. Maruyama, Annu. Rev. Nucl. Part. Sci. **45**, 41 (1995).
[88] R. Alley *et al.*, Nucl. Instrum. Methods Phys. Res. A **365**, 1 (1995).
[89] B. Wagner *et al.*, Nucl. Instrum. Methods Phys. Res. A **294**, 541 (1990).
[90] L. L. DeRaad, Jr. and Y. J. Ng, Phys. Rev. D **11**, 1586 (1975).
[91] H. R. Band *et al.*, Nucl. Instrum. Methods Phys. Res. A **400**, 24 (1997).
[92] M. Swartz *et al.*, Nucl. Instrum. Methods Phys. Res. A **363**, 526 (1995).
[93] L. G. Levchuk, Nucl. Instrum. Methods Phys. Res. A **345**, 496 (1994).
[94] D. G. Crabb and D. B. Day, Nucl. Instrum. Methods Phys. Res. A **356**, 9 (1995).
[95] A. Abragam and M. Goldman, Rep. Prog. Phys. **41**, 395 (1978).
[96] M. Borghini, CERN Yellow Report No. CERN 68-32 (1968).
[97] G. Court *et al.*, Nucl. Instrum. Methods Phys. Res. A **324**, 433 (1993).
[98] S. K. Dhawan *et al.*, IEEE Trans. Nucl. Sci. **43**, 2128 (1996).
[99] D. G. Crabb, in *Proceedings of the 9th International Symposium on High Energy Spin Physics*, Bonn, Germany, 1990, edited by W. Meyer, E. Steffens, and W. Thiel (Springer-Verlag, Berlin, 1991), Vol. 2, p. 289.
[100] B. Boden *et al.*, Z. Phys. C **49**, 175 (1991).
[101] B. Adeva *et al.*, Nucl. Instrum. Methods Phys. Res. A **372**, 339 (1996).
[102] T. J. Liu, Ph.D. thesis, University of Virginia, 1996.
[103] G. Petratos, R. L. Eisele, R. Gearhart, E. Hughes, and C. Young, Report No. SLAC-PUB-5678 (1991).
[104] V. Breton *et al.*, Nucl. Instrum. Methods Phys. Res. A **362**, 478 (1995).
[105] J. M. Bauer, Ph.D. thesis, University of Massachusetts, 1996.
[106] G. Gomez *et al.*, Phys. Rev. D **49**, 4348 (1994).
[107] M. Arneodo *et al.*, Phys. Lett. B **364**, 107 (1995).
[108] P. Amaudruz *et al.*, Nucl. Phys. **B371**, 3 (1992).
[109] T. V. Kukhto and N. M. Shumeiko, Nucl. Phys. **B219**, 412 (1983); I. V. Akusevich and N. M. Shumeiko, J. Phys. G **20**, 513 (1994).
[110] C. D. Buchanan and M. R. Yearian, Phys. Rev. Lett. **15**, 303 (1965); J. E. Elias *et al.*, Phys. Rev. **177**, 2075 (1969); S. Galster *et al.*, Nucl. Phys. **B32**, 221 (1971); R. G. Arnold *et al.*, Phys. Rev. Lett. **35**, 776 (1975); S. Auffret *et al.*, *ibid.* **54**, 649 (1985); R. Cramer *et al.*, Z. Phys. C **29**, 513 (1985); P. Bosted *et al.*, Phys. Rev. C **42**, 38 (1990).
[111] S. Galster *et al.*, Nucl. Phys. **B32**, 221 (1971); F. Iachello, A. D. Jackson, and A. Lande, Phys. Lett. **43B**, 191 (1973); S. Blatnik and N. Zovko, Acta Phys. Austriaca **39**, 62 (1974); G. Höhler *et al.*, Nucl. Phys. **B114**, 505 (1976), fit 5.3; J. G. Korner and M. Kuroda, Phys. Rev. D **16**, 2165 (1977); M. Gari and W. Krümpelmann, Z. Phys. A **322**, 689 (1985); unpublished fit to NE11 data: A. Lung *et al.*, Phys. Rev. Lett. **70**, 718 (1993).
[112] A. Bodek *et al.*, Phys. Rev. D **20**, 1471 (1979).
[113] L. M. Stuart *et al.*, Phys. Rev. D **58**, 032003 (1998).
[114] Y. S. Tsai, Report No. SLAC–PUB–848 (1971); Y. S. Tsai, Rev. Mod. Phys. **46**, 815 (1974).
[115] H. Olsen and L. C. Maximon, Phys. Rev. **114**, 887 (1959).
[116] P. Raines, Ph.D. thesis, University of Pennsylviania, 1996.
[117] V. Burkert and Z.-J. Li, Phys. Rev. D **47**, 46 (1993).
[118] U. K. Yang *et al.*, J. Phys. G **22**, 775 (1996).
[119] M. Arneodo *et al.*, Nucl. Phys. **B483**, 3 (1997).
[120] L. H. Tao *et al.*, Z. Phys. C **70**, 387 (1996).
[121] M. Lacombe *et al.*, Phys. Rev. C **21**, 861 (1980); R. Machleidt, K. Holinde, and C. Elster, Phys. Rep. **149**, 1 (1987); M. J. Zuilhof and J. A. Tjon, Phys. Rev. C **22**, 2369 (1980); L. Kotthoff, R. Machleidt, and D. Schütte, Nucl. Phys. **A264**, 484 (1976); B. Desplanques, Phys. Lett. B **203**, 200 (1988).
[122] M. V. Tokarev, Phys. Lett. B **318**, 559 (1993).
[123] W. Melnitchouk, G. Piller, and A. W. Thomas, Phys. Lett. B **346**, 165 (1995).
[124] N. L. Ter-Isaakyan, Phys. Lett. B **381**, 331 (1996).
[125] K. Abe *et al.*, Phys. Lett. B **405**, 180 (1997).
[126] T. Gehrmann and W. J. Stirling, Phys. Rev. D **53**, 6100 (1996).
[127] R. L. Heimann, Nucl. Phys. **B64**, 429 (1973).
[128] J. Kaur, Nucl. Phys. **B128**, 219 (1977).
[129] S. D. Bass and P. V. Landshoff, Phys. Lett. B **336**, 537 (1994).
[130] F. E. Close and R. G. Roberts, Phys. Lett. B **336**, 257 (1994).
[131] S. J. Brodsky, M. Burkardt, and I. Schmidt, Nucl. Phys. **B441**, 197 (1995).

[132] M. Göckeler *et al.*, Nucl. Phys. B (Proc. Suppl.) **53**, 81 (1997).
[133] A. Ali, V. M. Braun, and G. Hiller, Phys. Lett. B **266**, 117 (1991).
[134] B. I. Ermolaev and S. I. Troyan, Presented at 5th International Workshop on Deep Inelastic Scattering and QCD (DIS 97), hep-ph/9706324.
[135] R. Blankenbecler and S. J. Brodsky, Phys. Rev. D **10**, 2973 (1974).
[136] I. Hinchliffe and A. Kwiatkowski, Annu. Rev. Nucl. Part. Sci. **46**, 609 (1996).
[137] J. Ellis, E. Gardi, M. Karliner, and M. A. Samuel, Phys. Rev. D **54**, 6986 (1996).
[138] M. Anselmino, F. Caruso, and E. Levin, Phys. Lett. B **358**, 109 (1995).
[139] G. Baum *et al.*, Phys. Rev. Lett. **45**, 2000 (1980).
[140] V. Bernard, N. Kaiser, and U.-G. Meissner, Phys. Rev. D **48**, 3062 (1993).
[141] Z. P. Li and Zh. Li, Phys. Rev. D **50**, 3119 (1994).
[142] V. D. Burkert and B. L. Ioffe, Phys. Lett. B **296**, 223 (1992); JETP **78**, 619 (1994).
[143] J. Soffer and O. V. Teryaev, Phys. Rev. D **51**, 25 (1995); **56**, 7458 (1997).
[144] X. Ji, Report No. MIT-CTP-2468 (1995), hep-ph/9509288.
[145] B. Ehrnsperger and A. Schäfer, Phys. Rev. D **52**, 2709 (1995).
[146] G. Ross and R. G. Roberts, Phys. Lett. B **322**, 425 (1994).